Hoyle state rotational excitation studied via β-triple-α angular correlations

Ruchi Garg

PhD

University of York

Physics

October 2017

Abstract

The second 2^+ state of the ^{12}C nucleus is of great importance to nuclear astrophysics reaction rate calculations and also to nuclear cluster structure studies. The triple-α process, which is responsible for ^{12}C production, primarily proceeds through a resonance in the ^{12}C nucleus, famously known as the Hoyle state. The cluster nature of the Hoyle state allows the formation of a rotational band built upon it. The first member of the band is thought to be in the 9 – 11 MeV excitation energy region, with $J^\pi=2^+$. Further knowledge of this state would help not only to understand the debated structure of the ^{12}C nucleus in the Hoyle state, but also to better constrain the high-temperature ($> 10^9$ K) reaction rate of the triple-α process. The precise evaluation of the triple-α reaction rate is required to be able to understand the final stages of stellar nucleosynthesis and the elemental abundances in the universe.

In the past decade, several experiments have been performed in search for the 2_2^+ state of the ^{12}C nucleus. But the results from different measurements have been so different from each other that it has not been possible to reach a consensus on the resonance parameters. Due to the significance of the resonance, a reconciliation of the data from different available probes is highly desirable.

In this work, the first clear observation of the 2^+ rotational excitation of the Hoyle state via a ^{12}N β-decay experiment has been made. The state has been found at the energy 10.53 (17) MeV with width 1.35 (25) MeV. The experiment, $^{12}\mathrm{N}(\beta)^{12}\mathrm{C}(\alpha_1)^8\mathrm{Be}(\alpha_2)\alpha_3$, was performed at the IGISOL facility at JYFL, Jyväskylä, Finland. The identification of the 2^+ strength relative to that of the 0^+ in the 9 – 12 MeV energy region has been done through the novel technique of coincident detection of β-3α particles from the cascade, followed by the β-α_1 angular correlation studies.

Contents

List of Figures

List of Tables

Acknowledgements

First of all, I would like to thank my supervisor Christian, who has provided me with constant support and guidance throughout my PhD work. Over the years of my PhD, he has taught me so much physics and so much about research methods. This work would not have been possible without his guidance.

I would also like to thank all my collaborators and the IGISOL team who put in a lot of valuable work to this project during the experiment.

Many people from the Nuclear Physics research group at the University of York have helped in different ways and I am thankful to each of them for all the help I have received. But I would especially like to thank Alessandro and Charles for their time on my project when I was working on the angular correlation theory, and of course Simon, without whom we could not have run the experiment nearly as well as we did. I must also thank Alison for all her help and guidance on numerous occasions.

I am grateful to have shared my PhD time with Jos, James, and Nic. Not only were they great as colleagues to discuss physics or computational codes with, but they are also very good friends who kept me entertained throughout. They also provided me with sweets and chocolates in the occasional times of despair.

My friends Jess, Keri, and Adelle have been like a family to me here in the UK. I am thankful to them for many things. Every time I needed some practical information regarding the ways of this country, I would turn to one of them. They are my support system essentially. Also, if it was not for these three, I probably would've lost sense of the real world that existed outside of my PhD and my computer in the last few months. I am most grateful to Jess for reading and rereading my

thesis about 1000 times and also for the endless supply of motivation she has in store for whenever I run short of it.

Lastly and most importantly, I would like to express my deep gratitude towards my parents and my brother Tushar. Their constant support has given me the strength to keep going, and their confidence in me has helped me to maintain belief in myself.

Declaration

I hereby declare that except where a specific reference is made to the work of others, the contents of this thesis are original and have not been submitted in whole or in part for consideration for any other degree or qualification in this, or any other university. This dissertation is my own work and contains nothing which is the outcome of work done by others, except as specified in the text and Acknowledgements. All sources are acknowledged as references.

Ruchi Garg

October 2017

Chapter 1

Introduction and Motivation

The Hoyle state is an energy level in the ^{12}C nucleus at an excitation energy of 7.654 MeV. This state plays an essential role in the production of the ^{12}C nucleus in stellar nucleosynthesis. Hence why it has been of great interest to nuclear astrophysicists ever since its discovery. The historical account of how this state was predicted and discovered makes an interesting scientific tale. It has been covered in section 1.1 which gives a brief description of its role in stellar nucleosynthesis.

The interest in the Hoyle state is not limited to just the field of nuclear astrophysics. It is also an interesting case to study from a nuclear structure point of view. All the observations and calculations show that the ^{12}C nucleus exists as a cluster of three alpha-particles in this state. Section 1.2, gives a brief overview of the phenomenon of clustering in nuclei and also introduces the rotational excitation of the Hoyle state which is the central object to the work presented in this thesis.

1.1 Stellar nucleosynthesis

It was early in the 20th century that physicists started working on understanding the creation of elements in our universe. A popular theory of that period said that all the elements were created at the time of the Big Bang. It was thought that at the time of the Big Bang, when the universe was a hot, dense pool of nucleons, the elements were created in steps of one mass unit by neutron capture

and subsequent beta decay. But this theory had a major drawback. There are no stable isotopes corresponding to the mass numbers 5 and 8 (Figure 1.1). So, the theory could not explain the creation of elements heavier than the mass number 4.

Fig. 1.1 Nuclear chart showing light nuclei with number of neutrons on the x-axis, number of protons on the y-axis and with the lifetime of nuclei colour coded. It can be seen here that all the isotopes with mass 5 have lifetime less than 10^{-15} sec [1].

Another theory, stellar nucleosynthesis, most prominently described in the famous B^2FH publication [2], suggested that the elements heavier than hydrogen and helium are produced by nuclear fusion reactions at different stages of stellar evolution. Fred Hoyle, an English astronomer, was a strong proponent of this idea over the Big-Bang nuclesynthesis theory [3]. According to the stellar nucleosynthesis theory, in the first stage, in the core of a star where the temperature and the density are high enough ($>$ 8 MK), hydrogen nuclei fuse together through the coulomb barrier and turn into helium. This process of conversion of hydrogen into helium goes on for 90% of the star's life [4]. Eventually, when the hydrogen in the core is exhausted, the star's core starts to collapse under the action of gravity while the H-burning continues in a shell. This results in raising the temperature and the density of the core further. If the star is massive enough ($>$0.4 $M_{\odot}$), the temperature and density get high enough ($>$ 0.2 GK and 10^3 g cm^{-3}) to ignite He-burning in the core. During the He-burning phase, three He nuclei fuse together to form a ^{12}C nucleus. This process bridges the

mass gap of 5 and 8, and the production of the heavier nuclei can be explained with nuclear reactions at subsequent stages of burning in stars.

The subsequent stages of hydrostatic burning that follow after the H and He-burning are C, O, Ne, Mg, and Si-burning. They are all named after the element that is most abundant in the core at the stage and is burning by fusion with other lighter nuclei in the core. The onset of each stage requires higher temperatures than the previous one because the Coulomb barrier becomes larger for the heavier element. Therefore, different mass stars reach different levels of hydrostatic burning. Figure 1.2 shows the table taken from the textbook 'Nuclear Physics of Stars' by Christian Iliadis [4]. It lists the different stages of burning and the temperature and density at which they are ignited along with the initial mass of the star required to achieve those conditions. The last stage of burning ends up forming a core that is made up of iron and nickel mostly. The hydrostatic burning stops after this stage as further fusion of charged particles is not energetically favourable.

The iron core continues to collapse under the action of gravity, but at this stage nuclear fusion is not an option to generate the energy to counteract gravity. This causes the core-collapse to continue to the point that the density crosses the nuclear matter density of 10^{14} g/cm^3. The nuclear force being repulsive at short distances creates a rebound, sending a shock wave through the star leading to explosive burning in the outer shells.

1.1.1 The triple-α process and the Hoyle state

The triple-α process, as the name suggests, is the fusion of three α particles to form ^{12}C nuclei during the He-burning phase in stars. Although a direct three-body fusion would be possible at the density and temperature conditions in the core during the He burning, it would have too low a cross-section to explain the observed abundance of ^{12}C [5]. It was therefore suggested by Opik in 1951 [6] and Salpeter in 1952 [7], that the triple-α process must take place in two steps; the resonant formation of ^{8}Be

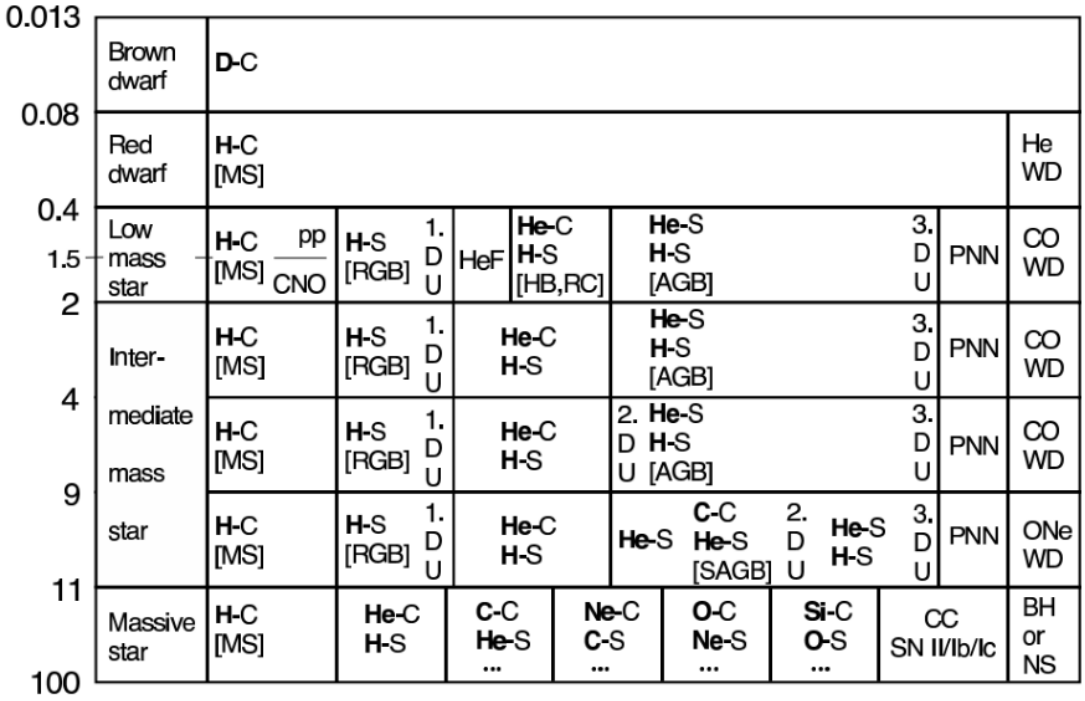

Fig. 1.2 Major evolutionary stages for single stars in different mass ranges [4]. Each row represents the evolution of stars in time (from left to right) in a certain mass-range (given on the left-hand side). The nuclear fuel in a burning phase is shown in bold, with '-C' referring to core burning and '-S' referring to shell-burning. The square bracket labels refer to the burning phase on the H-R diagram (refer to the textbook [4] for details of the H-R diagram). MS - main sequence, SGB - subgiant branch, RGB - red giant branch, and HB - horizontal branch. DU refers to the different dredge-up events. The '...' for massive stars indicate that there are additional overlying burning shells. The labels in the last column are: WD - white dwarf, CC - core collapse, SN - supernova, NS - neutron star, and BH - black hole.

by fusion of two α-particles followed by radiative capture of a third α-particle on the intermediate ^{8}Be.

I. $^{4}\mathrm{He} + {}^{4}\mathrm{He} \rightarrow {}^{8}\mathrm{Be}$

II. $^{8}\mathrm{Be} + {}^{4}\mathrm{He} \rightarrow {}^{12}\mathrm{C}* \rightarrow {}^{12}\mathrm{C} + \gamma$

Although the ^{8}Be has a very short half life of 7×10^{-17} s, Salpeter proposed that given the conditions (density and temperature) in the core of the star, there would always be some concentration of ^{8}Be available for the second step reaction [7].

In nuclear reactions, the phenomenon of a resonance plays a critical role. Those reactions in which the sum of the energies of nuclei in the input channel matches the energy state of the product, are called resonant reactions and have much higher cross-section (reaction probability) compared to non-resonant reactions.

The first step reaction in the triple-α process is known to be resonant with the ^{8}Be nucleus being unbound to two ^{4}He nuclei by 92 keV. But in the second step, the sum of mass energies of ^{4}He and ^{8}Be is 7.367 MeV more than the mass energy of ^{12}C in its ground state.

If the calculations on the reaction rate of Helium burning are performed by considering this second step reaction to be non-resonant, it does not reproduce the observed abundance of carbon. Following this argument, Hoyle did the reverse calculations with the conditions of the interior of stars and predicted that a resonance in the second step reaction should exist at the level 0.31 MeV corresponding to energy state 7.68 MeV in the ^{12}C nucleus [8]. Motivated by this prediction, experiments were performed to search for such a state and it was found that a state does indeed exist at the excitation energy of 7.654 MeV. This second 0^+ spin-parity state of the ^{12}C nucleus was named after its discoverer and was called the Hoyle state.

Since ^{12}C is the base of organic life, the energy placement of the Hoyle state in the ^{12}C level scheme has often been called a lucky coincidence of nature. This state lies right in the Gamow-window corresponding to the temperature of the He-burning phase ($\sim 2 \times 10^8$ K) for the α-capture on ^{8}Be. If the Hoyle state existed at an energy of a few hundred keV higher or lower, the rate of formation of ^{12}C would have been lower by 7 orders of magnitude [9].

1.2 2^+ rotational excitation of the Hoyle state

Theorists too were intrigued by the Hoyle state. The shell model, which was the leading model to study single particle excitations, does not predict a state at the Hoyle state's energy. This was a clear indication that the state has some different structure and requires a different modelling. Independent of the research on the Hoyle state, in 1938, Hafstad and Teller [10] had suggested that in the light α-conjugate nuclei, even the ground state contains some degree of α-clustering. The motivation behind this suggestion was the observed linear trend in the binding energy of these α-conjugate nuclei with respect to the number of α-α bonds. Then in 1968, Ikeda et

al. proposed the emergence of molecule-like structure in the self-conjugate 4n nuclei near the α-decay threshold [11]. Figure 1.3 shows the famous Ikeda diagram. In this diagram, the threshold energies have been shown for α-conjugate nuclei up to ^{24}Mg.

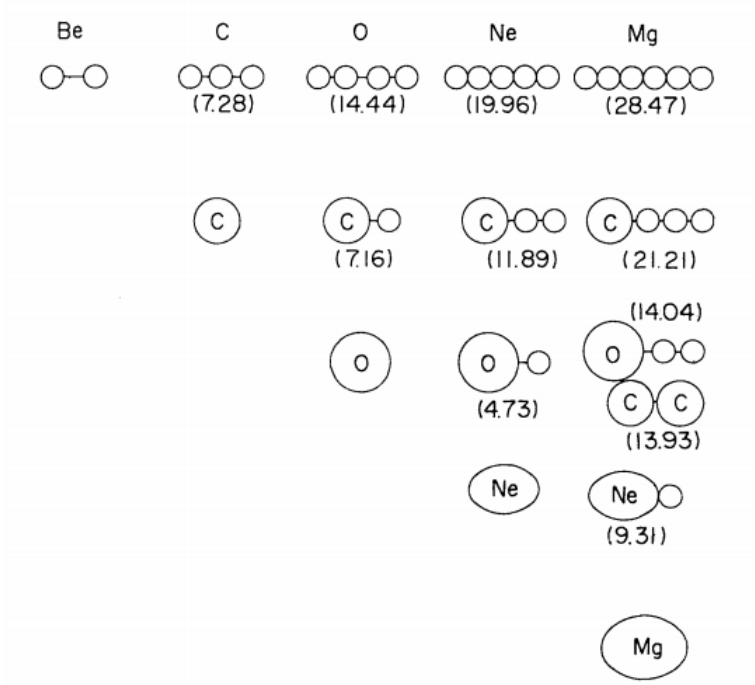

Fig. 1.3 The Ikeda diagram. It shows the different decay thresholds for self-conjugate $4n$ nuclei upto ^{24}Mg [11].

Once it was established that the ^{12}C nucleus has a cluster structure in the Hoyle state, it was treated as a deformed/non-spherical quantum object in further studies which resulted in the prediction of a rotational band built upon the Hoyle state. In the work by H. Morinaga [12], the Hoyle state is assumed to be a linear chain like rotor and the energy of the first rotational excitation of the Hoyle state, the second 2^+ state of the ^{12}C nucleus, is predicted at 9.7 MeV.

Ever since its prediction by Morinaga, there have been numerous attempts to search for this rotational excitation of the Hoyle state. There are two main things that motivated the attention this state received from the nuclear physics community; its role in the triple-α process at higher temperatures ($>10^9$ K), and the potential it holds for revealing the debated structure of the Hoyle state.

1.2.1 Role in the triple-α process

The triple-α process during hydrostatic He-burning mainly proceeds through the Hoyle state. But during explosive burning, higher lying broad states with low energy tails also participate in the triple-α process [13]. Figure 1.4 shows the comparison of the reaction rate for the triple-α process calculated for a high temperature environment with and without the inclusion of the second 2^+ state of the ^{12}C nucleus. The figure has been taken and adapted from the PhD thesis of Zimmerman [14]. The rates shown in the figure have been taken from two different databases. The one shown in the red line is from NACRE (Nuclear Astrophysics Compilation Reaction Rates) [15]. This compilation includes the theoretically predicted second 2^+ state at 9.12 MeV. The other one, shown with a blue line, has been taken from the JINA (Joint Institute for Nuclear Astrophysics) REACLIB database [16]. This compilation took the values from the work by Fynbo *et* al. [17]. It can be seen from the figure 1.4 that the presence of the 2^+ rotational excitation of the Hoyle state can affect the reaction rate by more than an order of magnitude at temperatures higher than 5 GK.

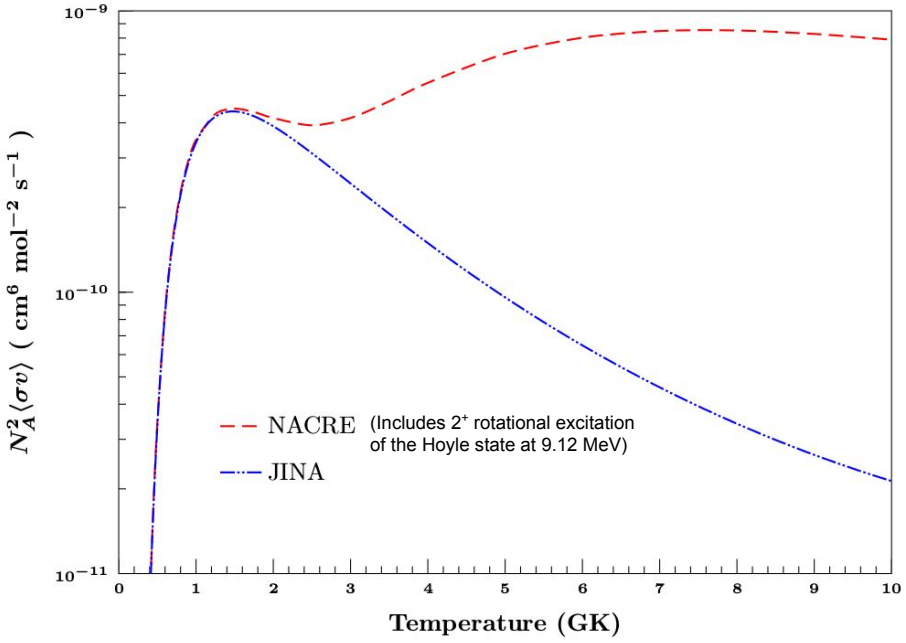

Fig. 1.4 The calculated reaction rate of the triple-α process at high temperatures (>10^9 K) with and without including the 2_2^+ state of the ^{12}C nucleus [15, 16]. Figure adapted from the PhD thesis by Zimmerman [14]

The high temperature triple-α reaction rate can have significant impact on heavy element production in explosive scenarios [18, 19]. It is therefore required to reconcile between different datasets on the energy of the 2_2^+ state.

1.2.2 Role in determining the Hoyle state's structure

It has been nearly 60 years since the Hoyle state was discovered. Even though a significant effort has been put into trying to establish the arrangement of the α-particles in this state, it still remains ambiguous. Different theoretical frameworks, predict the structure of the Hoyle state differently. For example, the linear-chain like arrangement [20], the Bose-Einstein condensate [21], and the obtuse angle or the bent arm arrangement [22] (see figure 1.5).

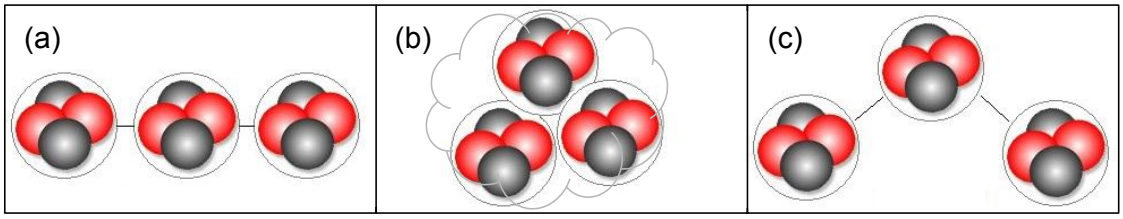

Fig. 1.5 Illustration of the different arrangements of the triple-α cluster in the Hoyle state. (a) Linear-chain arrangement. (b) Bose-Einstein Condensate. (c) Bent-arm structure arrangement.

With these different structural arrangements, the Hoyle state as a rotor would have a different moment of inertia. The energy of the rotational excitation has an inverse proportionality with the moment of inertia of the rotor object.

$$E_{rot} = \frac{\hbar^2}{2I} J(J+1)$$

This means, if the energy of the rotational excitation of the Hoyle state is measured experimentally, the above formula can be used to extract the moment of inertia of the Hoyle state and hence it can give the information on the radius of the state.

1.3 The experiment: β-delayed α-emission

There are different ways that can be and have been used in the past to study the energy levels in the ^{12}C nucleus. To list a few different methods, there are: the inelastic scattering of protons or α-particles on a ^{12}C target [23–26], the gamma-excitation of the ^{12}C nucleus [27], the charge exchange reactions such as ^{11}B(^{3}He,d)^{12}C [28, 29], and the β-delayed particle emission method [17, 30].

The main difficulty in the experimental observation of the 2^+ rotational excitation of the Hoyle state is the presence of other strong states in the same energy region as where it is predicted by theoretical models [22, 31, 32], i.e., 9 – 11 MeV excitation energy. The 9.64 MeV 3^- state and the 10.88 MeV 1^- state lie right in the energy region of interest (see figure 1.6 for the ^{12}C level scheme diagram). There is also the $\sim$3 MeV broad 0^+ strength at 10.3 MeV. The presence of these states make it difficult to observe the 2^+ strength in the region directly.

In the work presented in this thesis, the β-decay of ^{12}N was used to populate the states of interest in the ^{12}C nucleus. The decay equation is as follows:

$$^{12}\mathrm{N} \rightarrow ^{12}\mathrm{C} + \beta^+ + \nu_e + 17.338\ \mathrm{MeV}$$

The ^{12}N nucleus in its ground state has the spin-parity of 1^+. The selection rules for β-decay are such that they allow only 0^+, 1^+ and 2^+ states to be populated in the daughter nuclei from the 1^+ state in the parent nuclei. Therefore, the β-decay method provided a better selectivity in populating the states compared to the other methods such as inelastic scattering. In the work presented, the 9.64 MeV 3^- state and the 10.88 MeV 1^- state were not populated at all and hence the spectrum was relatively cleaner to analyse.

In the experiment, β-triple-α coincidences were detected from the cascade $^{12}\mathrm{N}(\beta^+)^{12}\mathrm{C}(\alpha_1)^{8}\mathrm{Be}(\alpha_2)\alpha_3$. Using the measured energies and momenta of three α-particles from the ^{12}C breakup, kinematics calculations were performed to extract the properties of the state from which they broke. Using the momenta of α_2 and α_3,

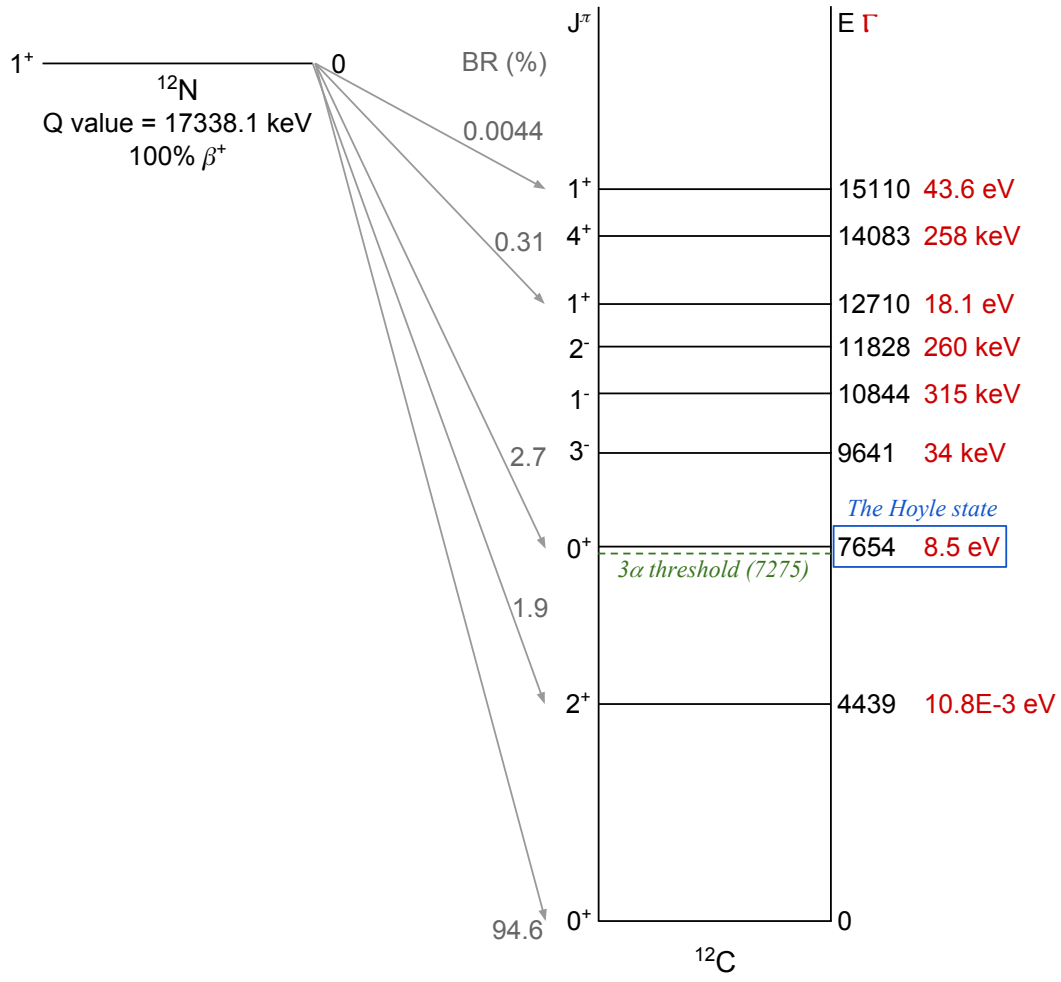

Fig. 1.6 The level scheme diagram of the ^{12}C nucleus. On the left hand side the branching ratios of the β-decay of ^{12}N into different states of ^{12}C has been shown. The values are taken from reference [33].

the energy of the intermediate ^{8}Be nucleus was calculated to determine the breakup channel. The different possible breakup channels and their kinematics have been discussed in detail in chapter 5. The breakup channel information was enough to cut out the 1^+ state component from the data. But to separate out the 0^+ component from the 2^+ component, the β-α_1 angular correlations were analysed. The β-α angular correlation is isotropic for the ^{12}C 0^+ state, whereas for the 2^+ state, the angular correlation has an anisotropy that depends on the β-decay matrix elements.

1.4 Outline of the thesis

The following chapters consist of all the details of the presented work. Chapter 2 contains a brief review of the literature on the subject of this work; the first rotational excitation of the Hoyle state. It lists the experiments that have been performed in the past to look for the state along with their results. Comparisons have also been made between the values obtained in different experiments.

In chapter 3 the theory relevant to the present work has been given in sufficient detail that is required for the complete and coherent understanding of the presented work and results. These details include the theoretical modelling of clustering in nuclei, basics of the β-α angular correlation theory, and the overview of the R-matrix theory.

Chapters 4 and 5 consist of the details of the experimental work (such as, the beam production, the detector setup, and the electronics) and the data analysis procedure respectively. In chapter 6, the results from the data analysis have been presented. Also the R-matrix work done with the data has been shown in this chapter. Finally, the thesis concludes with chapter 7, which contains the remarks on the unusually large anisotropy that has been observed in the β-α angular correlations in this work. This chapter also provides the motivation and suggestions for future work on the subject.

Chapter 2

Previous work and results

There have been several attempts in the past at searching for the first rotational excitation of the Hoyle state in the ^{12}C nucleus using various probes. The present chapter gives a summary of some of those works and their results. In section 2.1, the results from the previous β-delayed particle emission experiments have been presented. Section 2.2 contains the results from the inelastic scattering experiments such as (p,p') and (α, α'). Lastly, in section 2.3 the most recent results from the γ-excitation $(\gamma, 3\alpha)$ experiment have been discussed.

2.1 β-delayed particle emission experiments

The β-decay of ^{12}N and ^{12}B have been used several times before to study the structure of the ^{12}C nucleus. In this section, the results from the experiments performed at JYFL, CERN, and KVI over the period of 2001 – 2007 have been discussed.

In the work by Fynbo *et* al. [17], the data from two experiments were analysed and presented. The first experiment was performed with the ^{12}N beam at the IGISOL facility in JYFL in 2001. The second experiment, with a ^{12}B beam, was performed at the ISOLDE facility at CERN in 2002. Both the experiments used triple-α coincidence detection. The results from the R-matrix analysis on these datasets have been shown in figure 2.1, as they were presented in [34]. In the upper plot, they compared their data with the previous literature value of the 10 MeV 0^+ resonance

assigned in the work [35]. In the lower plot, they showed the R-matrix fit (as the solid black line) to their data. Their R-matrix fit included the Hoyle state, the broad 10 MeV 0^+ resonance, and the 2^+ strength. It can be seen that they did not observe any significant 2^+ strength at energies below 12 MeV, hence they concluded the existence of the 9 MeV 2^+ resonance to be doubtful.

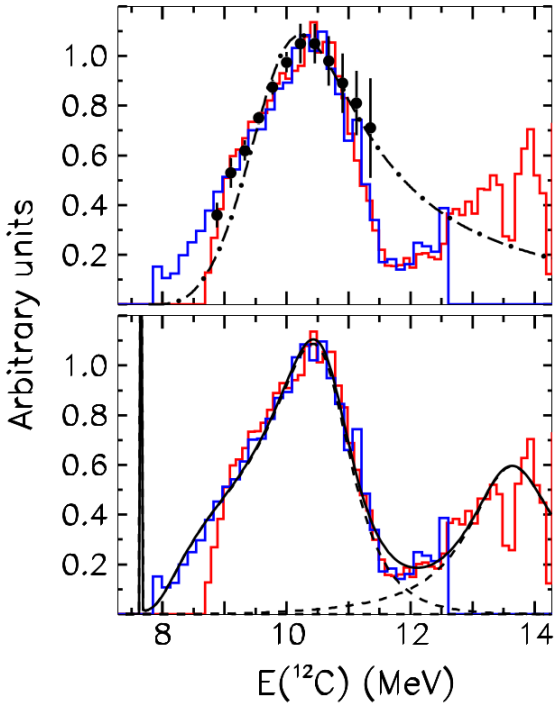

Fig. 2.1 The results from the IGISOL (2001) and the ISOLDE (2002) experiment with β-decay of ^{12}N (red) and ^{12}B (blue) respectively. The lower plot shows the R-matrix fit (solid black line) to the data [17, 34].

In another set of work by Hyldegaard *et* al. [30], the combined analysis on the data sets from two individual β-decay experiments was performed to measure the 0^+ and 2^+ composition of the broad resonance structure at 10 MeV excitation energy. The two experiments were performed at IGISOL (2004) and KVI (2006) with ^{12}N and ^{12}B beams used in both experiments. They performed the R-matrix fitting to the data using different number combinations of 0^+ states and 2^+ states. Their best fit result was obtained with three 0^+ states and two 2^+ states. This fit result to the ^{12}N decay data has been shown in figure 2.2. In conclusion, they recommended the 2_2^+ state's energy and width to be 11.1 $\pm$ 0.3 MeV and 1.4 $\pm$ 0.4 MeV respectively.

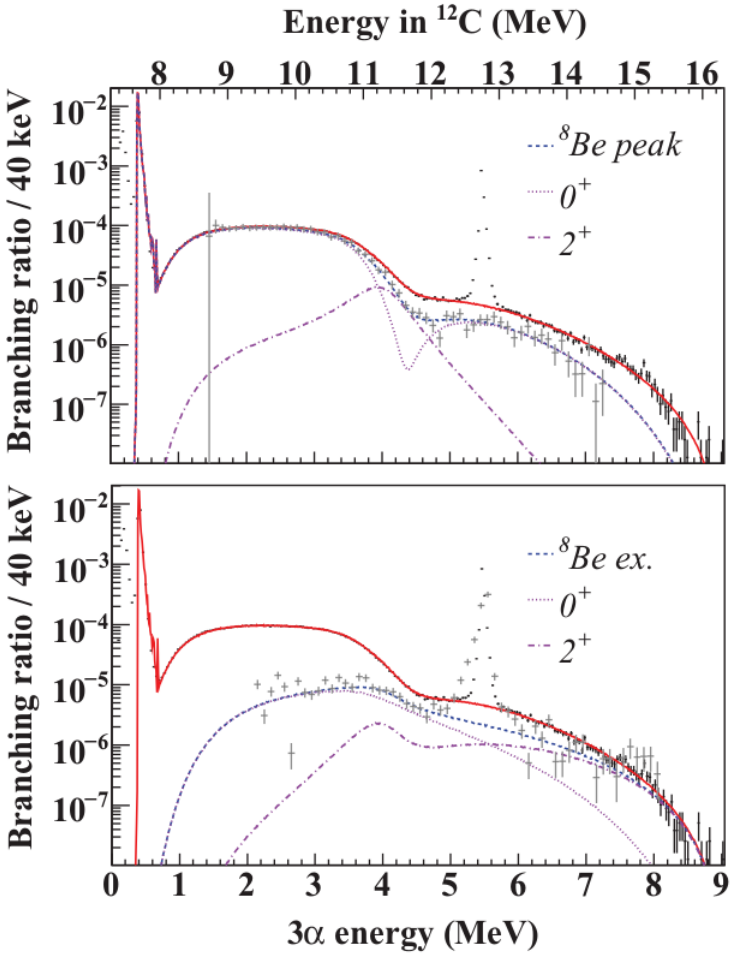

Fig. 2.2 The R-matrix fit with three 0^+ and two 2^+ states to the ^{12}N β-decay data from experiments performed at IGISOL and KVI. Both plots contain the complete 3α data from the KVI experiment. The upper plot shows the IGISOL data gated on the breakup channel via the ^{8}Be ground state. The lower plot shows the IGISOL data gated on breakups via the ^{8}Be excited state. The solid red line shows the total fit summed over all the channels [30].

2.2 (p,p') and (α, α') scattering experiments

Inelastic scattering is another method that has been used multiple times in an attempt to look for the 2_2^+ state of the ^{12}C nucleus. This simple method consists of a beam of the projectile particle (p or α in the cases presented here), the ^{12}C target, and the spectrometer to study the energy spectrum of scattered beam particles at different angles.

Itoh *et* al. performed the ^{12}C(α, α') measurements at RCNP, Osaka with 386 MeV α-particles at forward angles ($\theta = 0° - 10°$) [23]. They performed Multipole Decomposition Analysis (MDA) to study the relative contribution of different spin states in

the energy of interest. They reported the observation of the 2_2^+ state under the 0^+ bump at ∼10 MeV excitation energy. They performed the experiment again in 2011 to gain the statistics and reported the energy and width of the 2_2^+ state at 9.84 ± 0.06 MeV and 1.01 ± 0.15 MeV respectively [25].

In 2009, the ^{12}C(p, p') measurement was performed by Freer *et* al. [24] with a 66 MeV proton beam at iThemba LABS, South Africa. In this work, by R-matrix analysis, the 2_2^+ state was reported to have been observed at an energy of 9.6 ± 0.1 MeV with a width of 600 ± 100 keV.

Three years later, in 2012, Freer *et* al. [36] published a combined analysis on both the experimental data sets; the ^{12}C(α, α') RCNP experiment [23, 25] and the $^{12}C(p, p')$ iThemba LABS experiment [24]. The energy and the width of the 2_2^+ state was reported to be consistent between the two datasets and were found to be 9.75 ± 0.15 MeV and 750 ± 150 keV respectively. The R-matrix fit results on ^{12}C(α, α') data has been shown in figure 2.3 and the fit result on ^{12}C(p, p') data has been shown in figure 2.4. The grey shaded area in both these figures show the shape of the 2_2^+ state as extracted from R-matrix fit and calculations.

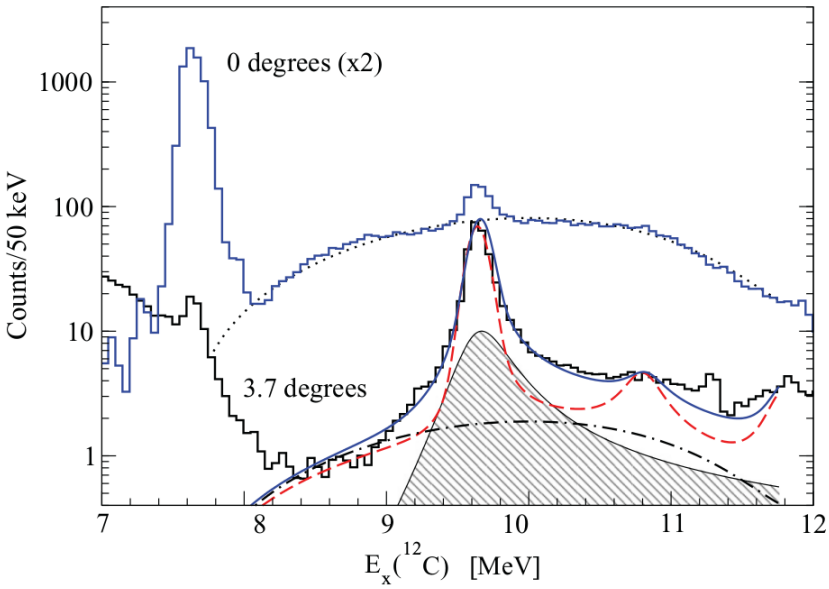

Fig. 2.3 R-matrix analysis performed by Freer *et* al. in [36] on ^{12}C(α, α') data from the RCNP experiment [23, 25]. The red dashed line shows the calculation with all the known states in the ^{12}C nucleus. The solid blue line corresponds to the calculations with the 2^+ state included.

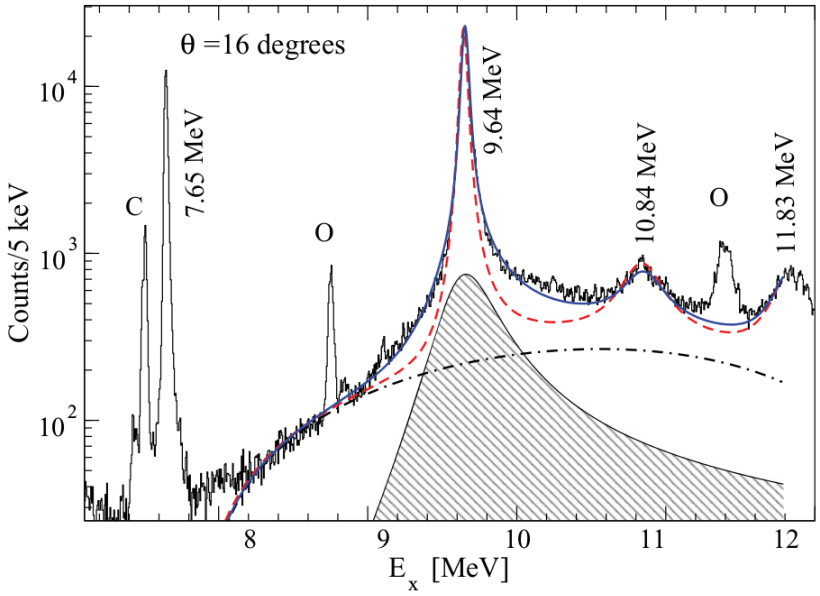

Fig. 2.4 *R*-matrix analysis performed by Freer *et* al. in [36] on $^{12}C(p, p')$ data from the iThemba experiment [24]. The red dashed line shows the calculation with all the known states in the ^{12}C nucleus. The solid blue line corresponds to the calculations with the 2^+ state included.

2.3 γ-excitation experiment

In a recent publication by Zimmerman *et* al. [27], they presented the results from the $^{12}C(\gamma, 3\alpha)$ experiment that was performed at the HIγS facility of TUNL at Duke University. The experiment consisted of an Optical Readout Time Projection Chamber (O-TPC) operating with a mixture of gases CO_2 and N_2, and γ-ray beams with energies between 9.1 and 10.7 MeV and intensities of 2×10^8 γ/s.

This method had the advantage that from the 0^+ ground state of ^{12}C, the broad 0^+ component in the 10 MeV region could not be populated via the γ-excitation. Therefore, they only had to distinguish the 2^+ strength from the 1^- at 10.844 MeV. This was done using the complete angular distribution of the $^{12}C(\gamma, \alpha_o)^8Be$ events and identifying the *E2* strength relative to *E1* strength as a function of energy. In this work, they reported a clear observation of the 2^+ resonance at 10.03 ± 0.11 MeV excitation energy with a width of 800 ± 130 keV. The results have been shown in figure 2.5. There has been some reservation about these results within the

collaboration recently, and the revised analysis of the data seems to suggest a lower value for the resonance energy [37].

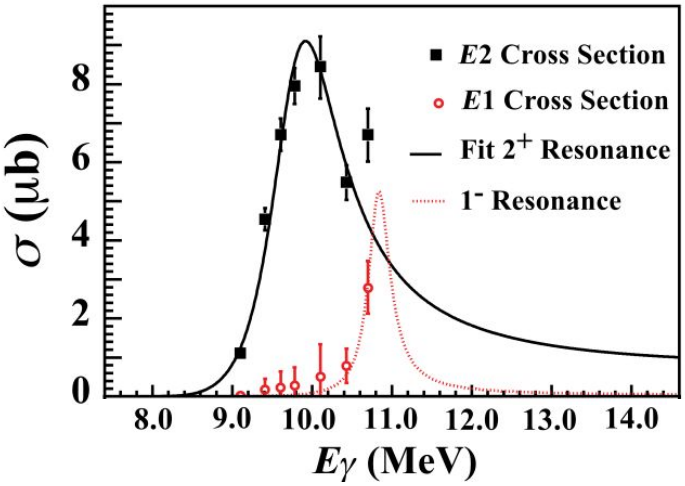

Fig. 2.5 $^{12}C(\gamma, 3\alpha)$ experiment results [27]

2.4 Discrepancy between different works

Each of the three different experimental techniques that have been discussed in this chapter have reached a different conclusion from the others on the resonance parameters for the 2_2^+ state of the ^{12}C nucleus. This discrepancy could be an artefact of the difference in population mechanism, or it could be due to human error during the experiment or the analysis. Whatever the reason, there is clearly a need to either reach an agreement between different experiments, or understand the physics reason behind the discrepancy. In the work presented in this thesis, a measurement was made of the 2_2^+ state using the β-decay method. But in addition to R-matrix fitting, the novel technique of β-3α angular correlation has been used for the first time. The results from different works have been summarised in table 2.1 along with the result of the present work.

Experiment	Energy (MeV)	Width (MeV)
^{12}N, ^{12}B β-decay [30]	11.1 ± 0.3	1.4 ± 0.4
^{12}C(α, α') [23]	9.84 ± 0.06	1.01 ± 0.15
^{12}C(p, p') [24]	9.6 ± 0.1	0.6 ± 0.1
Combined analysis of ^{12}C(p, p') and ^{12}C(α, α') [36]	9.75 ± 0.15	0.75 ± 0.15
^{12}C$(\gamma, 3\alpha)$ [27]	10.03 ± 0.11	0.8 ± 0.13
Present work: β-3α analysis of ^{12}N β-decay	10.53 ± 0.17	1.35 ± 0.25

Table 2.1 Summary of recent literature values of energy and width of the 2_2^+ state of ^{12}C nuclues. The results from the present work have also been shown for comparison.

Chapter 3

Theory

3.1 Theoretical modelling of clustering in nuclei

The Hoyle state has been a matter of interest to nuclear theorists ever since its prediction and discovery. While the shell model calculations work very well to reproduce the 4.44 MeV 2^+ state of the ^{12}C nucleus, it fails to predict anything in the energy region of the Hoyle state [38, 39]. The shell model fails to reproduce the Hoyle state because this state does not fall into the single-particle excitation picture, but has a cluster structure. Different groups of theorists across the world have tried to reproduce the Hoyle state and its rotational excitation using various models. A few different models have been discussed briefly in this section.

3.1.1 Bose-Einstein Condensate Model

α-particles consist of two protons and two neutrons, all coupled to a net spin of zero. This means that asymptotically they can be treated as bosons. Therefore, if a cluster state has a radius large enough to allow the asymptotic nature to play a significant role, the α-particles in such a state can form a degenerate condensate. Such a system can be described by the wave-function,

$$\langle r_1, r_2, .., r_n | \Phi_{N\alpha} \rangle = \mathcal{A}[\phi(\alpha_1), \phi(\alpha_2), .., \phi(\alpha_N)], \tag{3.1}$$

where $\Phi_{N\alpha}$ is the α cluster wave-function describing an alpha particle Bose condensed state. $\mathcal{A}$ is the antisymmetrization operator to take the Pauli Exclusion principle into account. $\phi(\alpha_n)$ is the internal wave-function of the n_{th} α-particle, given by a Gaussian wave-packet.

This wave-function is famously known as the THSR wave-function, named after Tohsaki, Horiuchi, Schuck, and Röpke [21]. Their work was adapted from a more simplistic Alpha Cluster Model (ACM), developed by Brink [40].

The total wave-function in equation 3.1 has a dependency on two free parameters; the size of the free α-particle and the size of the total Gaussian distribution. This dependency makes the importance of the antisymmetrization operator $\mathcal{A}$ become negligible in the limits where the size of the total Gaussian distribution is large. This leaves the total wave-function as a multiplication of Gaussians. Such a wave-function describes the system as a gas of free α-particles [41]. On the other hand, if the size of the total distribution is small (of the scale of the ^{12}C ground state radius), the antisymmetrization operator $\mathcal{A}$ comes into play, and the Bose condensate structure dissipates.

The BEC model predicts the 2^+ excitation of the Hoyle state at 9.4 MeV energy with the width of 600 keV [31, 42].

3.1.2 Molecular Dynamics: *AMD* and *FMD*

The AMD (*Antisymmetrized Molecular Dynamics*) [43] and the FMD (*Fermionic Molecular Dynamics*) [32] are the two different models that use the same approach but with a small difference. In this approach, the wave-function of the nucleus is given by the Slater determinant of the Gaussian wave packets of individual nucleons in the nucleus. The single-particle wave function of a nucleon consists of the spatial, intrinsic spin, and isospin wave functions. The difference between FMD and AMD is that in the FMD calculations, the width of the Gaussian wave-packets is left as a free parameter, while in the AMD calculation a single value for width parameter is chosen as the optimal value of each nucleus. The Hamiltonian of the system is

constructed using an effective nucleon-nucleon interaction potential. Finally, the properties of the nucleus (such as radii, densities, transition strengths) are calculated by minimising the expectation value of the Hamiltonian for the spin-parity projected wave-function.

This method is different to the ACM [40] or the BEC [21] (section 3.1.1), as it does not presume the clustering in the nucleus from the outset. The nucleon-nucleon interaction in the calculations result in the formation of the cluster structure. These models have been able to reproduce not only the cluster states such as the Hoyle state [32, 43], but in [43] they have also successfully reproduced the shell-model-like state (the first 2^+ excitation of ^{12}C nucleus). The 2_2^+ state is predicted at 2.33 MeV above the Hoyle state energy in their calculation [32].

3.1.3 *Ab initio* calculations

The *ab-initio* approach is the most fundamental of the all that have been discussed here in this section. The calculations in this approach are based on the first principle of nucleon-nucleon interaction and no assumptions regarding the structure or the wave function of the nucleus are made *a priori*. The difficulty is such calculations is the many-body nature of the nuclear forces. The nuclear interaction is thought to be mediated via meson exchange between two nucleons, and the presence of a third nucleon can alter the properties of the one of the two original nucleon during the meson exchange with them and hence affecting the properties of their interaction with each other.

An ideal model to study the nuclear properties should take into account these degrees of freedom in calculation, which suggests that the solution lies in the QCD theory regime. Epelbaum *et* al. in reference [22] have used the Chiral Effective Field Theory (ChEFT) on a grid of discretized space and time to address the many nucleon problem (up to A=12). A review of the theory and the framework has been given in reference [44]. In the chiral EFT framework the interaction of protons and neutrons is treated as systematic expansion in powers of nucleon momenta and

pion mass. For the typical particle momentum Q, the most effective term in the interaction Hamiltonian is the $O(Q^0)$, called the leading order (LO) term. In the work presented in [22], the terms with power of up to three, Next-to-Leading order (NLO) $O(Q^2)$, and Next-to-Next-to-Leading Order (NNLO) $O(Q^3)$, have been included in the calculations. The discretization of the space and time is a mathematical tool to numerically solve the Hamiltonian.

They have reported the emergence of the Hoyle state as well as its 2^+ rotational excitation in their calculations at the energy of 9.65 MeV [22].

3.2 Beta Decay

In a β-decay process, a neutron is converted into a proton (or vice versa), emitting an electron (or positron) along with an anti-neutrino (or neutrino). In this process, the mass number of the nucleus remains the same, but the atomic number changes by $\pm$ 1 (for $\beta^{\mp}$-decay). There are three types of radioactive processes that fall under the β-decay category: the β^--decay of the neutron-rich nuclei, the β^+-decay of the proton-rich nuclei, and the e^--capture of the proton-rich nuclei. These processes can be expressed as the following equations:

$$ {}^{A}\mathrm{X}_{Z} \rightarrow {}^{A}\mathrm{Y}_{Z+1} + \beta^- + \bar{\nu}_e $$

$$ {}^{A}\mathrm{X}_{Z} \rightarrow {}^{A}\mathrm{Y}_{Z-1} + \beta^+ + \nu_e $$

$$ {}^{A}\mathrm{X}_{Z} + e^- \rightarrow {}^{A}\mathrm{Y}_{Z-1} + \nu_e $$

Where, ν_e and $\bar{\nu}_e$ are electron neutrino and anti-neutrino respectively.

Since the β-decay is a three-body process, the energy spectrum of the β-particle is continuous. The spectrum shape can be derived from the Fermi theory of β-decay.

For a transition between an initial quantum state, ψ_i, and a final quantum state ψ_f, the decay constant can be given by the Fermi's Golden Rule as,

$$\lambda = \frac{2\pi}{\hbar}\left| \int \ \psi_f^* V \psi_i \ dv \right|^2 \rho(E_f) \tag{3.2}$$

Where, V is the interaction that triggers the transition. It is treated as a perturbation to the potential in the theory. $\rho(E_f)$ is the density of states in the exit channel. While the initial wave function ψ_i is the total wave function of the parent nucleus, the final wave function ψ_f consists of three parts; the daughter nucleus wave function, the travelling wave of the electron, and the travelling wave of the corresponding neutrino.

To derive the spectral shape from equation 3.2, the problem is solved in two parts. In the first part the state density $\rho(E_f)$ is calculated using statistical mechanics by calculating the number of ways the Q-value energy can be divided between electron and neutrino. In the second part, the matrix element, $\mid \int \ \psi_f^* V \psi_i \ dv \mid^2$ is calculated. Combining the two, the decay probability as a function of β-particle's momentum is calculated as,

$$\lambda(p_e) \ dp_e = \frac{2}{\pi^3 \hbar^7 c^3} \mid M_{fi} \mid^2 \ g^2 \ (Q - T_e)^2 \ p_e^2 \ dp_e \tag{3.3}$$

where p_e is the momentum and T_e is the kinetic energy of the β-particle. g is the strength parameter. $\mid M_{fi} \mid^2$ is the nuclear matrix-element and is calculated from the overlap between the wave functions of the initial and final state. This function is called the ***phase space*** of the decay.

In the function shown in equation 3.3, the Coulomb effect due to the charge of the β-particle has not been included. To incorporate this effect, the Coulomb-distorted wave functions for electron and neutrino must be used while calculating the matrix-element. This was done by Fermi, resulting in the inclusion of a spectrum distorting

factor called the Fermi function, $\mathrm{F}(Z_D, p_3)$, where Z_D is the atomic number of the daughter nucleus. The final form of the β-spectrum then takes the form,

$$\lambda(p_e)\ dp_e = (\text{constants})\ \mathrm{F}(Z_D, p_e)\ (Q - T_e)^2\ p_e^2\ dp_e \tag{3.4}$$

Integrating equation 3.4 gives the decay constant as,

$$\lambda(p_e) = \frac{g^2 \mid M \mid^2 m_e^5 c^4}{2\pi^3 \hbar^7}\ f(Z_D, Q) \tag{3.5}$$

where $f(Z_D, Q)$ is the Fermi integral. Finally, rearranging the above equation for half-life, $t_{1/2}$, the comparative half-life, ***ft-value*** is obtained.

$$ft_{1/2} = \ln 2\ \frac{2\pi^3 \hbar^7}{g^2 \mid M \mid^2 m_e^5 c^4} \tag{3.6}$$

The range of half-lives for different β-decay ranges from 10^3 to 10^{20} s. Therefore, often the logarithm of *ft* value is used to show the half-life of a decay [45].

3.2.1 Decay Selection Rules

The conservation of angular momentum and parity set some selection rules in the β-decay, dividing them into classes; *allowed* and *forbidden*. The selection rules for *allowed* decays are:

$$\Delta I \equiv |I_i - I_f| = 0\ or\ 1$$

$$\pi_i \pi_f = +1$$

where I_f and I_i are the total spin, and π_f and π_i are the parities of the of parent and daughter nuclei. ΔI is the vector difference of the I_f and I_i values. The leptons in the decay together can take away the total spin value of 0 or 1 depending on whether the β-particle and the ν have antiparallel or parallel spins. The former case is classified as the *Fermi selection rule* and the latter is called the *Gamow-Teller selection rule*.

It should be noted that the base for these selection rules is that for ΔI to be greater than 1, or for $\pi_i\pi_f$ to be -1, the leptons that are generated in a small volume of the nucleus during the decay would have to carry a unit of orbital angular momentum. So, while it is rare to observe such decays, they are not entirely forbidden. The degree to which a decay is forbidden (first, second, ..) is defined by the L value of the decay.

3.2.2 β-α angular correlation

In the present work, two different approaches have been used to evaluate the theoretical expression for the β-α angular correlation for the cascade,

$$^{12}\mathrm{N}(1^+) \xrightarrow{\beta^+} {}^{12}\mathrm{C}(2^+) \rightarrow {}^{8}\mathrm{Be} + \alpha_1$$

The first approach is the more fundamental of the two. The starting point in this approach is the simple expression for the angular distribution of α-decay from polarized nuclei.

$$W(\theta) = \sum_{m_i} p(m_i)\, G(m_i, m_f)\, W(\theta)_{m_i \rightarrow m_f}, \tag{3.7}$$

where, $W(\theta)_{m_i \rightarrow m_f}$ is the directional distribution function for initial magnetic substate m_i to the final magnetic substate m_f transition in α-decay of ^{12}C. It is directly proportional to the modulus square of the spherical harmonics, $|Y_L^m(\theta, \phi)|^2$, where L is the orbital angular momentum of the α-decay and m is the magnetic substate of the decaying nucleus. $G(m_i, m_f)$ is the relative transition probability and is 1 for all values of m_i for the $^{12}\mathrm{C}(2^+) \rightarrow {}^{8}\mathrm{Be}(0^+)$ case. $p(m_i)$ is the probability of spin projection m_i in ^{12}C along the z-axis (defined by the momentum vector direction of β-particle). It is the $p(m_i)$ values that are dependent on the polarization effect of the β-decay.

The expression for $p(m_i)$ has been derived using the β-decay density matrix elements in the book *Alpha-, Beta-, and Gamma-ray Spectroscopy* by Siegbahn [46]:

$$P(m) = \sum_{k=0}^{2I} \sum_{J,J'} (-1)^{I+m} (2k+1)^{1/2} (2I+1)^{-1/2} \times \begin{pmatrix} I & I & k \\ m & -m & 0 \end{pmatrix} b_k(J,J') F_k(JJ'I_iI), \tag{3.8}$$

where I is the spin of the final state after the decay and J is the total spin taken away by the leptons while $J \leq J'$. $b_k(J,J')$ are the β-parameters that consist of the matrix-elements. The full expression for $b_k(J,J')$ and $F_k(JJ'I_iI)$ coefficients are given in reference [46] in chapter XIXA, equation 146 and equation 96 respectively. Usually, in the allowed transition approximation, the values for $k \geqslant 2$ are neglected under the assumption that the higher-order corrections and the relativistic correction on the coordinate type matrix elements and the momentum type matrix elements in the $b_k(J,J')$ are negligibly small.

In the first attempt to calculate the $p(m_i)$ values for $^{12}\mathrm{N}(1^+)$ β-decay to $^{12}\mathrm{C}(2^+)$ from equation 3.8, the $k \geqslant 2$ values were neglected and the results were a linearly polarized system with values, $p(-2) = 0.2 + 0.2$; $p(-1) = 0.2 + 0.1$; $p(0) = 0.2$; $p(+1) = 0.2 - 0.1$; $p(+2) = 0.2 - 0.2$.

Inserting these values of $p(m_i)$ into equation 3.7, the net angular distribution function comes out isotropic. This result of isotropic distribution for a linearly polarized system can can be predicted even by just looking as equation 3.7 because the component for any m_i value is proportional to the modulus square of the $Y_L^m(\theta,\phi)$, which is identical for $\pm$m values.

Therefore it is clear that if the β-decay has contributions only from the vector and axial vector couplings then the β-α angular correlation has to be isotropic. In the experimental data, however, there was a clear observation of anisotropy in the angular correlation plots (section 5.7 and 6.1). This prompted an attempt at calculations with the inclusion of higher order corrections and relativistic corrections. Such calculations ($b_k(J,J')$ parameters for $k \geqslant 2$) are, however, not straightforward

as they require the values of higher order matrix elements, which in turn require the complete understanding of the initial and final states' wave functions. Some additional insight was therefore needed to calculate the angular correlation function.

A general expression for the angular correlation expression was derived by Morita and Morita [47] that can be to calculate the $W(\theta)$ distribution for the specific case of ^{12}N(1^+) β-decay to ^{12}C(2^+). This expression in reference [47] is given by,

$$W(\theta) = \sum_{n=0}^{2j_1,even} \Big\{ \Big[\sum_{L \leqslant L'} (-1)^{j_1-j+n} b^n_{LL'} W(j_1 j_1 l L'; nj)(2j_1+1)^{1/2} \Big] \times \Big[\sum_{L_1, L'_1} (j_2 \| L_1 \| j_1)(j_2 \| L'_1 \| j_1) F_n(L_1 L'_1 j_2 j_1) \Big] \Big\} P_n(cos\theta), \tag{3.9}$$

with

$$F_n(L_1 L'_1 j_2 j_1) = (-1)^{j_2-j_1-1}[(2j_2+1)(2L_1+1)(2L'_1+1)]^{1/2} \times (L_1 L'_1 00|n0) W(j_2 j_1 L_1 L'_1; n j_1), \tag{3.10}$$

where the notations are same as used by Morita in [47]. L is the difference between the total spins of parent and daughter nuclei. Therefore, for the β-decay it is the rank of the β-decay matrix element and for the α-decay it is the orbital angular momentum of the α-particle. j's are the spins of the nuclei in the decay cascade in the order. Specifically, for ^{12}N(1^+) $\xrightarrow{\beta^+}$ ^{12}C(2^+) $\xrightarrow{\alpha}$ ^{8}Be(0^+), the j, j_1, and j_2 are 1, 2, and 0 respectively. L and L_1 are 1 and 2. $(j_2 \| L_1 \| j_1)$ and $(j_2 \| L'_1 \| j_1)$ are the reduced matrix elements for the α-decay. $W(j_1 j_1 L L'; nj)$ and $W(j_2 j_1 L_1 L'_1; n j_1)$ are the *Wigner*-6j symbols. $(L_1 L'_1 00|n0)$ is the 3j symbol. Finally, $b^n_{LL'}$ are the β-parameters and their values in terms of matrix-elements have been given in the reference [47].

By substituting the values for all of these variable in equation 3.9, the final simplified expression for the angular correlation function was obtained as,

$$W(\theta) = 0.023\ b^0_{11} \left[1 - \frac{b^2_{11}}{b^0_{11}}\ 0.3162\ P_2(cos\theta) \right] \tag{3.11}$$

From this expression, it can be seen that the anisotropy in the β-α angular correlations across the excitation energy region of interest in the ^{12}C nucleus is proportional to the second order Legendre polynomial $P_2(cos\theta)$. This proportionality is what was ultimately used in this work to fit the experimental angular distributions.

It should be noted from equation 3.11 that the proportionality constant for the anisotropy is proportional to the ratio of the β-parameters, b^2_{11} and b^0_{11}. The second-forbidden type nuclear matrix elements in b^2_{11} are of the order of magnitude $(p_eR)^2 \approx 10^{-2}$ as per the most fundamental theory of β-decay [46]. Therefore the the anisotropy in the β-α or even β-γ angular correlations is normally expected to be very small (of the order of 0.001 per MeV of β-particle's energy). However, in the cases where the allowed transition is inhibited by the structural differences between the parent and daughter states b^0_{11} could be small and the interference terms in b^2_{11} would become large, making the ratio b^0_{11}/b^2_{11} significant. Table 1 in [48] gives a complete account of the expected order of magnitude of the matrix elements in the β-parameters for different ranks of nuclear matrix elements.

A similar calculation for the β-α angular correlation for the 12.71 MeV 1^+ state in the ^{12}C nucleus shows that this distribution function is expected to be isotropic.

3.3 *R*-matrix Theory

The experimental data should be fitted using a theoretical model to extract a complete description of the resonances in the observed spectrum of α_1-particles in the cascade ^{12}N$(\beta^+)^{12}$C$(\alpha_1)^8$Be. If it was the case of a reaction that proceeds via a single isolated resonance, and a single exit channel, the Breit-Wigner formula [49] could very well describe the observed cross-section. Since that is not the case however, the R-matrix theory was used to extract the energy and the width of the resonances that contributed to the spectrum. The R-matrix formalism is the mathematical description of the theory of resonance reactions that was developed by Wigner and his collaborators in the 1940s. This section presents a brief introduction of the theory along with an outline of the mathematics involved.

The main complication in a nuclear reaction theory that treats the formation of a compound nucleus, lies in the configuration space which allows multiple alternative reactions that can lead to the formation of the same compound nucleus or the multiple alternative ways via which the same compound nucleus can decay. In the R-matrix theory, the configuration space is divided into two regions: the external region where the particle pair interact only via the long-range force (the Coulomb force), and the internal region where the wave function of the system is governed by the many-body nuclear forces. The external region provides the information on scattering physics parameters such as collision matrix, phase shifts, or penetration factor. The internal region provides the nuclear physics parameters such as the level energy, level width, or reduced widths. With the knowledge of mass, energy, spins (internal and orbital), and charge of the particles in a reaction, the external wave function can be solved analytically. This wave function is then matched with the internal wave function on the channel boundary to solve for the collision matrix.

The detailed mathematical formulation of the R-matrix theory has been reviewed in several articles [50–52]. Therefore, only a small summary has been given here, mostly in the same form as in reference [53].

3.3.1 External Wave Function

For channel $c = \alpha sl$, where α is the particle pair, s is the channel spin, and l is the relative orbital angular momentum of the particles, the radial component of the external wave-function is given by the equation,

$$\phi_c = \left(\frac{1}{v_c}\right)^{1/2}(y_c I_c + x_c O_c), \tag{3.12}$$

where v_c is the relative channel velocity, y_c and x_c are the amplitudes of incoming and outgoing waves with wave functions I_c and O_c respectively.

Equation 3.12 can be rewritten in terms of incoming wave amplitudes as,

$$\phi_c = \left(\frac{1}{v_c}\right)^{1/2}\left(y_c I_c + \sum_{c'} U_{cc'} y_{c'} O_c\right), \tag{3.13}$$

where U is the collision matrix given by equation,

$$x_c = -\sum_{c'} U_{cc'} y_{c'} \tag{3.14}$$

The experimentally measured cross section, σ is a measure of this matrix U as

$$\sigma \propto |1 - U|^2 \tag{3.15}$$

3.3.2 Internal Wave Function

The internal wave function is derived by starting from the radial wave equation for the nuclear potential and adding the boundary condition to it. This results in a Hermitian eigenvalue problem with the eigenstates X_λ forming the complete base. With some mathematical manipulation, the radial component of the internal wave function is derived as,

$$\phi_c = \left(\frac{m_c a_c}{\hbar^2}\right)^{1/2} \sum_{c'} R_{cc'} \left(\frac{\hbar^2}{m_{c'} a_{c'}}\right)^{1/2} [\rho_{c'} \phi'_{c'} - B_{c'} \phi_{c'}], \tag{3.16}$$

where, m_c is the reduced mass, a_c is the channel radius, $\rho_c = k_\alpha a_c$, k_α is the wave number, and B_c is the boundary condition. ϕ' is the derivative of ϕ with respect to $k_\alpha r$. $R_{cc'}$ in equation 3.16 is the ***R*-matrix**, defined as,

$$R_{cc'} = \sum_{\lambda} \frac{\gamma_{\lambda c}\ \gamma_{\lambda c'}}{E_\lambda - E'} \tag{3.17}$$

where $\gamma_{\lambda c}$ is the reduced width amplitude of the level λ. The reduced width amplitude is a measure of the contribution of a level to the total channel wave function at the surface. It is given by the expression,

$$\gamma_{\lambda c} = \left(\frac{\hbar^2}{2m_c a_c}\right)^{1/2} \int dS X_\lambda^* \psi_c, \tag{3.18}$$

where, ψ_c is the channel wave function and the quantity $X_\lambda^* \psi_c$ represents the overlap of the level λ's wave function with the total channel wave function at the surface. With this definition of the reduced width amplitude, it can now be stated that the R-matrix contains all the information regarding the nuclear structure that is relevant is the reaction.

3.3.3 Matching the internal and external wave functions

By matching the logarithmic derivative of the internal and external wave functions at the channel surface, the relationship between the collision matrix ($U_{cc'}$) and the R-matrix ($R_{cc'}$) is obtained as,

$$U_{cc'} = \rho_c^{1/2} O_c^{-1} (1 - RL)^{-1} (1 - RL^*) I_{c'} \rho_{c'}^{-1/2}, \tag{3.19}$$

where, the diagonal matrix L_c is given by the following equation in terms of matrices; energy shift-function S_c, boundary constant B_c, and the penetrability P_c.

$$L_c \equiv S_c - B_c + iP_c \tag{3.20}$$

With the formalism described in sections 3.3.1 - 3.3.3, the parameters of the R-matrix theory, the pole energy E_λ and the reduced width amplitude $\gamma_{\lambda c}$ are calculated. Which are related to, but are not the same as the observed parameters from the experimental measurements, resonance energy $\tilde{E}_\lambda$ and the partial width

$\Gamma_{\lambda c}$. The observed width can be expressed in terms of physical width, $\tilde{\gamma}_{\lambda c}$, which is the reduced width for the boundary condition taken as $S_c(\tilde{E}_\lambda)$.

$$\Gamma_{\lambda c} \equiv \frac{2P_c\tilde{\gamma}_{\lambda c}^2}{1+\sum_k \tilde{\gamma}_{\lambda k}^2 (dS_k/dE)_{\tilde{E}_\lambda}} \tag{3.21}$$

When the boundary condition matches the shift function S_c, the pole energy can be taken as the resonance energy.

The calculations were performed using AZURE2, which is a computer code that can model low energy nuclear reactions in the multichannel, multilevel R-matrix framework [53]. It consists of mainly two subroutines. In the first subroutine the code calculates the parameters like boundary conditions, shifts, penetrability using the input channel information. In the second subroutine it uses the MINUIT package [54] to perform the iterative fitting of the cross-section from the R-matrix parameters while minimising the χ^2 value.

Chapter 4

Experimental Setup

The experiment consisted of a ^{12}N ion beam impinging on a carbon stopper foil, which was surrounded by a silicon detector array. The setup was located inside a vacuum chamber at a pressure of $\sim 10^{-6}$ mbar. A silicon detector array was used to detect α and β particles from the cascade $^{12}\mathrm{N}(\beta^+)^{12}\mathrm{C}(\alpha_1)^8\mathrm{Be}(\alpha_2)\alpha_3$, and a germanium detector outside the vacuum chamber was used to detect gamma particles. The details of these components and their associated electronics are discussed in the following sections, with section 4.1 covering the beam production, section 4.2 describing the stopper foil and detector arrangement, and section 4.3 explaining the details of electronics setup and the DAQ.

4.1 Beam production at the IGISOL facility, JYFL

The experiment required a beam of ^{12}N ions, which was produced using the Ion-Guide technique at the IGISOL (Ion-Guide Isotope Separator OnLine) facility at JYFL. Generally, in the Ion-Guide technique, the ions of interest are produced in a nuclear reaction between a primary beam of protons or deuterons from the cyclotron and the (thin) target material nuclei. The target foil is surrounded by a helium buffer gas located inside a gas cell in the target chamber. The target material is chosen to produce the desired beam for the experiment; in this experiment, the target material was ^{12}C. The resulting ions from the nuclear reaction recoil out of the thin target

foil into the helium buffer gas. In the buffer gas the ions undergo thermalisation, creating a range of different charge states. Between 1% and 10% of the ions are produced in a single-charge state [55]. These singly-charged ions are extracted from the buffer gas and are sent to the mass separator. The extraction process involves transporting the ions from the buffer gas cell to the high vacuum isotope separator, which is done using a differential pumped electrode. For the purpose of skimming the ions, using an electric potential and differential pumping, a double radiofrequency SextuPole Ion beam Guide (SPIG) is placed between the target chamber and the extraction chamber. The systematics of the IGISOL setup are shown in figure 4.1.

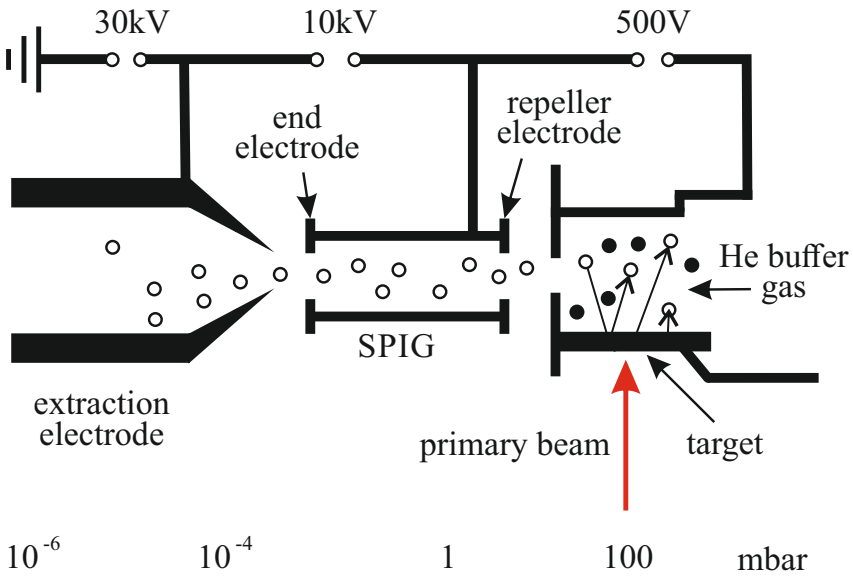

Fig. 4.1 The IGISOL technique mainly consists of the primary beam hitting the target, the buffer gas thermalising the ions in the ion-guide, the SPIG electrode to skim the charged ions from the buffer gas, and finally the extraction electrode. This figure also shows the differential gas pressure and voltage at different stages of extraction.

For the present work, the ^{12}N ions were produced using a proton beam on a ^{12}C target in the reaction,

$$^{12}C + p \rightarrow {}^{12}N + n \tag{4.1}$$

The primary beam of protons with 30 MeV kinetic energy was delivered by the K130 cyclotron. The carbon foil used in the target chamber was 1.7 mg/cm^2 thick on a 4.5 μm Ta backing.

The yield of ^{12}N ions was estimated to be ∼1500 ions/s by monitoring the β-particle count rate. This was also calculated using the data. The details of the calculation are covered in section 5.4.3.

4.2 Stopper foil and detectors

The extracted beam of ^{12}N ions with an energy of 29.9 keV/u entered the vacuum chamber, where it was completely stopped in a ^{12}C foil of ∼22 μg/cm^2 thickness. This thickness is the average of the measured value before and after the experiment. The details of the technique used to measure foil thickness are covered in section 5.3.

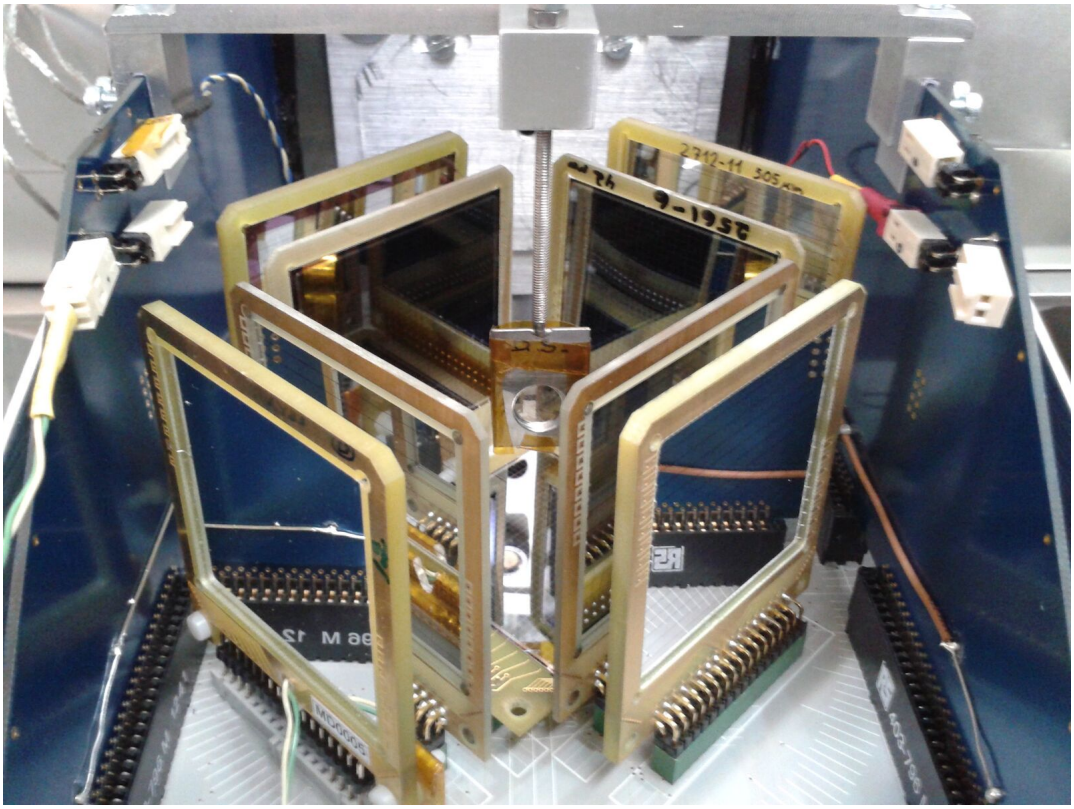

Fig. 4.2 A picture of the detector arrangement taken looking upstream.

The ^{12}N nuclei, completely at rest, underwent β^+ decay, populating different energy states in the ^{12}C nucleus. ^{12}C nuclei with an excitation energy higher than

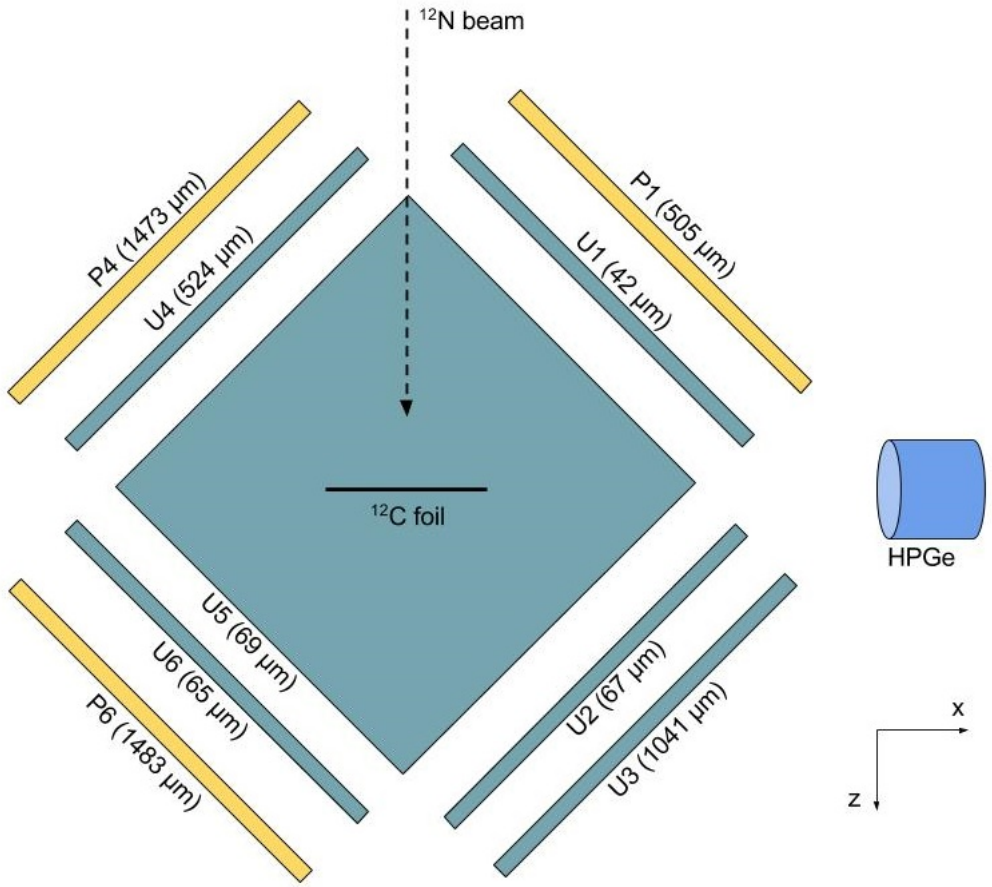

Fig. 4.3 A schematic diagram of the top view of the detector set up. The relative dimensions in this diagram are not to scale.

the triple-α threshold typically breakup into three α-particles. The stopper foil was surrounded by an array of Silicon detectors for observing the energy and direction of the β and α particles produced. Figure 4.2 shows a picture of the detector arrangement looking in upstream. Figure 4.3 shows the schematic diagram of the setup.

The detectors were placed in a double layered cubical arrangement around the foil. The inner layer was built with thinner silicon detectors which completely stopped the α-particles while allowing the β-particles to punch through and hit the outer layer of silicon detectors. This arrangement was designed to ensure the α-particles would be easily distinguished from the β-particles. Table 4.1 lists all the detectors with their respective thicknesses and positions.

Detectors labelled 'U' in Figure 4.3 are W1 type DSSSDs (Double Sided Silicon Strip Detectors). This type of detector provides high energy resolution charged particle detection while also providing reasonably good position resolution. The active area of the W1 silicon wafer is 49.5×49.5 mm in dimension. It is segmented into 16 vertical strips on the front side and 16 horizontal strips on the back side. Each strip is 3 mm wide and the inter-strip region is 0.1 mm wide. For any particle that enters the active region, the signal is read from the front strip contact and the back strip contact, providing the position of the hit within the precision of 3×3 mm, which is the size of a pixel. Appendix A contains the specification of the W1 DSSSD detectors.

Six W1 detectors were used in the experiment, and their positions can be seen in Figure 4.3. Five were placed next to the ^{12}C stopper foil in a cubic arrangement with the top uncovered. These five detectors were used for α-particle detection from the triple-α breakup events. The sixth W1 detector, named U3, was placed parallel to and behind the 67 μm thick U2 detector. The thickness of the U2 detector made it nearly transparent to the β-particles, while still allowing it to completely shield the U3 detector (DSSSD used for β-particle detection) from α-particles.

The spatial arrangement of the detectors in the setup had a typical efficiency of $\sim$2% for the triple-α detection and $\sim$0.15% for the β-triple-α detection. These efficiencies have been calculated using a Monte-Carlo simulation of the setup. The details of the simulation have been described in section 5.5.

The thickness and the (x, y, z) coordinates of the centre of each U detector are given in table 4.1. The coordinate frame was defined with the origin (0, 0, 0) at the center of the stopper foil, the z-axis along the beam direction, the y-axis vertically upwards, and the x-axis orthogonal to the z- and y- axes.

Detectors that have been labelled 'P' in Figure 4.3 are the Silicon Pad detectors. They are non-segmented silicon detectors with single-sided readout. They are also 50×50 mm in size. They were installed in the setup with the intention of having

Name	Thickness (μm)	Position (mm)		
		x	y	z
U1	42	24.50	1.00	-29.50
U2	67	24.00	0.30	16.50
U3	1041	34.00	00.45	27.00
U4	524	-26.00	0.50	-24.00
U5	69	4.15	-35.00	-9.00
U6	65	-30.00	00.00	25.00

Table 4.1 The table shows the list of the DSSSDs along with their thickness in μm and the position coordinates of the detector center in mm. The origin of the system was defined at the center of the beam spot, the z-axis was along the beam direction, and the y-axis was along the vertically upward direction.

a larger geometrical efficiency for β-triple-α coincidence detection. But due to the high level of noise in the detectors, their signals have not been used in the analysis.

An HPGe detector was also used for gamma-ray detection. Its purpose was to measure the characteristic 4.44 MeV gamma-rays from the ^{12}C nucleus and use the intensity for beam normalisation. This detector was also used to validate the low energy calibration of the U3 detector (β-particle detector) by studying the Compton lines using a ^{60}Co source. The technique has been discussed in details in section 5.1.2.

4.3 Data acquisition system

When a charged particle passes through the Silicon detector, it causes the creation of electron-hole pairs. The amount of charge generated is proportional to the energy of the incident particle. The ionisation energy of Si at room temperature is 3.62 eV [56]. The present section explains the electronic circuit and modules that were used to process these signals from detectors and convert them to signals that could be read into the DAQ. The whole circuit and all its components (the modules) work with one or both of the two types of pulses caused by the incident particle; the linear

pulse and the logic pulse. A linear pulse carries the information in its amplitude and shape. However, for a logic pulse it is the instance or timing of its generation that matters [56].

Figure 4.4 shows a block diagram of the electronic circuit that was used for signal processing for the DSSSD (U) detectors in this experiment.

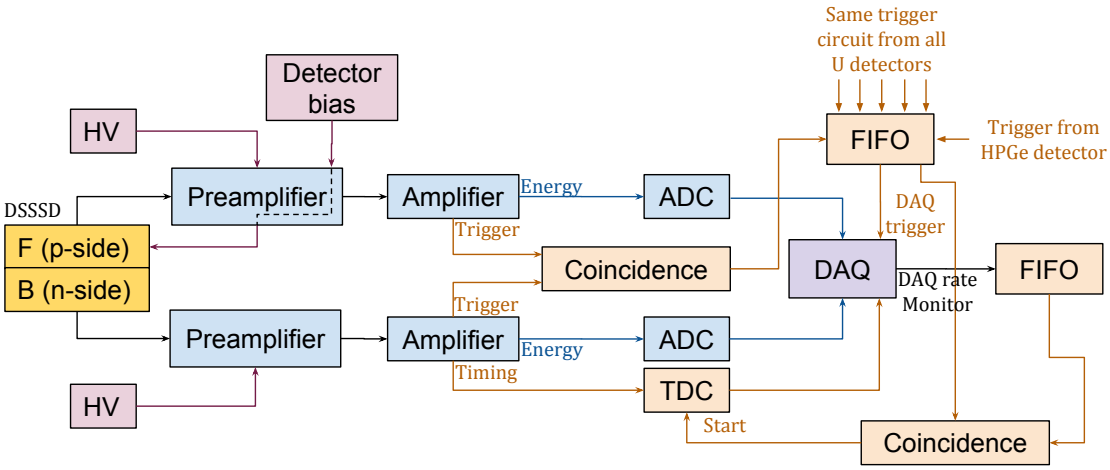

Fig. 4.4 A flow-chart diagram of the electronics set up for the DSSSDs. The components in blue show the linear pulse processing chain. The linear pulses carry information on the energy of the detected event. The orange colour components show the logic pulse chain. The logic pulses hold the information on the timing of the events. The logic pulses were also used for setting the trigger to the DAQ.

4.3.1 Shaping and amplification of the linear signal

The signal-processing electronics began with the preamplifiers, the purpose of which was to prepare the signal generated by charge collection at the detector electrodes for further amplification and pulse shaping. The output pulse from the preamplifier was a linear tail pulse and the amplitude was of the order of 250 mV per MeV of energy of the incident particle. The preamplifiers were also used as the interface to apply the bias voltage to the detectors.

The output from the preamplifiers was fed into linear amplifiers. The linear amplifiers (also called shaping amplifiers) were used for the shaping and amplification of the pulse to the accepted amplitude range of the DAQ. The shaped output

pulse was finally fed into the ADC (Analogue to Digital Convertor) modules, which ultimately input the signal into the DAQ.

4.3.2 Timing signal processing

The linear amplifiers generate a logic pulse corresponding to each signal. These logic pulses were used for determining the timing information for particles incident on the detectors in any event. The TDC (Timing to Digital Convertor) modules were used to measure the timing of each detected incident in an event. The clocks for all TDC modules channels were started simultaneously using the same logic pulse that triggered the DAQ. A clock would stop for any channel when the logic pulse from the amplifier arrived at the corresponding channel at the TDC. The time difference between the start and the stop signal was then recorded as the timing information of the incident. The timing signal processing and the trigger circuit are shown in orange in Figure 4.4. The coincidence between the DAQ trigger and DAQ rate monitor was taken to ensure that the TDC modules' clocks were started only for the accepted events.

There were two different types of modules of linear amplifiers that were used in the experiment; Mesytec MSCF-16 and Mesytec STM-16+. The main difference between these two modules is the way they generate the logic pulse corresponding to a signal. One has a constant fraction discriminator (MSCF modules) while the other has a leading edge discriminator (STM). The timing properties of the modules with the leading edge discriminator are energy dependent. Therefore, the MSCF modules were used for the back side channels as the timing information was recorded only for the back channels of all the detectors except U3. For U3, both front and back side channels were connected to the TDCs.

4.3.3 Trigger circuit

The DAQ starts to look for the signals from the ADC and TDC modules when it records any trigger pulse, and it was desired that all real hits be recorded while

ignoring the non-real signals such as noise in the detectors. To achieve this, the DAQ trigger generation was set to require a coincidence between signals from the front and the back of the detectors. All six of the output logic pulses corresponding to the six DSSSDs from the coincidence unit were fed into a Fan In Fan Out (FIFO) unit. The FIFO unit is essentially an OR circuit, and the output from this was set as the trigger to the DAQ.

4.3.4 Thresholds

Trigger threshold

The linear amplifier modules were used to set the discriminator thresholds to reduce the trigger rate from the low level background and noise signals. The discriminator threshold determined the lower limit on the height of the linear pulse that would generate the logic pulse.

MIDAS ADC thresholds

The trigger rate was controlled using the hardware (amplifier) thresholds, but the low level noise could still be observed in the data through one channel whenever the DAQ was triggered by another channel. This would have caused a high event rate to be recorded, filling up the disks unnecessarily. To avoid this, the readout thresholds were set on each ADC channel individually using the MIDAS software.

The thresholds (both hardware and software) were changed as necessary throughout the experiment.

Chapter 5

Data Analysis

The data in its most raw form consist of a series of hexadecimal numbers that only contained the information on the ADC and TDC channel numbers that were fired in an event and the corresponding digital signals (ADC peak height and timing). The data analysis that was performed to convert those numbers into physical information such as energy and momentum of the particles has been detailed in this chapter.

A typical event during the experiment underwent one of the four possible sequences;

$$^{12}\mathrm{N} \xrightarrow{\beta^+,\nu} {}^{12}\mathrm{C} \tag{5.1}$$

$$^{12}\mathrm{N} \xrightarrow{\beta^+,\nu} {}^{12}\mathrm{C}* \xrightarrow{\alpha_1} {}^{8}\mathrm{Be} \rightarrow \alpha_2 + \alpha_3 \tag{5.2}$$

$$^{12}\mathrm{N} \xrightarrow{\beta^+,\nu} {}^{12}\mathrm{C}* \xrightarrow{\alpha_1} {}^{8}\mathrm{Be}* \rightarrow \alpha_2 + \alpha_3 \tag{5.3}$$

$$^{12}\mathrm{N} \xrightarrow{\beta^+,\nu} {}^{12}\mathrm{C}* \rightarrow \alpha_1 + \alpha_2 + \alpha_3 \tag{5.4}$$

In the first sequence, the ^{12}C nucleus was formed in its ground state or in the first excited 2^+ state at 4.44 MeV energy, which is below the triple-α threshold of 7.275 MeV. So, these decays did not result in the triple-α breakup of the nuclei. In the second, third, and fourth sequences, the ^{12}C nucleus was formed with an excitation energy above the triple-α threshold, and can decay via triple-α breakup. In the second and third sequences, the triple-α breakup was sequential, involving the intermediate ^{8}Be nucleus either in its ground state or first excited state. Whereas,

in the fourth sequence it was a three-body breakup. The main motivation of the experiment was to search for the 2^+ strength in the 9-11 MeV energy region. Two main steps were taken in the data analysis to achieve this. The first step was to construct the excitation energy spectrum of the ^{12}C from the α-particles' energies. The energy spectrum was gated on specific breakup channels: either the equation 5.2 breakup channel or the combined equation 5.3 and 5.4 breakup channels. The second step was to use the β-α angular-correlations to determine the spin-parities of the resonance strengths observed. But to be able to perform these two steps, the data had to be sorted into the physical information form by calibrating the setup first. Figure 5.1 shows a flow chart of the different stages of the data analysis process. The techniques used in each stage have been explained in detail in the following sections, with energy and geometry calibration in section 5.1 and 5.2 respectively, foil thickness measurement in section 5.3, data reduction in section 5.4, Monte-Carlo simulation in section 5.5, kinematic reconstruction in section 5.6, angular correlation analysis in section 5.7, and geometrical uncertainties in section 5.8.

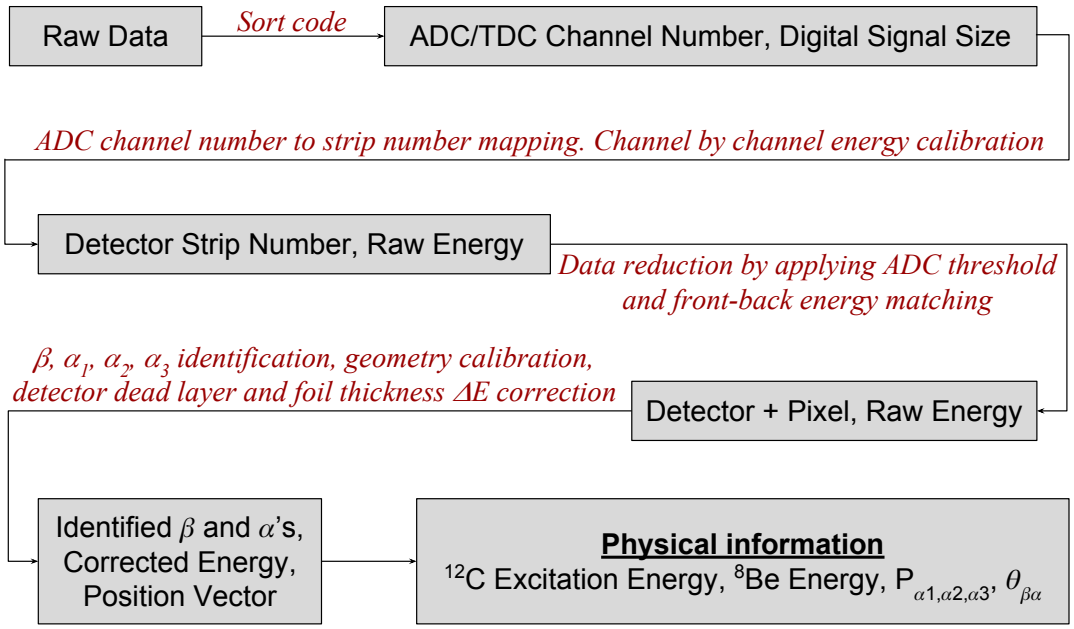

Fig. 5.1 A flow-chart diagram showing the different stages of data analysis.

5.1 Energy calibration of silicon detectors

To convert the digital signal corresponding to an event into the energy of the incident particle, it was required to establish the relationship between the energy and the ADC signal (between 0 - 4096) for each channel. Equation 5.5 shows the linear equation used to convert the ADC output to an energy using the parameters gain and offset. The calculation of these parameters is described in this section.

$$energy = gain \times ADC\ output + offset \tag{5.5}$$

5.1.1 Calibration of α-particle detectors

The energy calibration was done in two steps. The first step was to obtain the equation between the input voltage at any preamplifier channel and the corresponding digital output at the ADC module. This was achieved using the pulser data. As the name suggests, a pulser is an electronic module that can generate periodic pulses at a desired voltage. The pulser was connected to the preamplifier input and various values of pulser voltages were sent through the electronic circuit that a real signal from detector would go through. The pulser voltage was changed in regular increments starting from 0 volts and going up to the maximum preamplifier input value corresponding to the full ADC output range. An example of the pulser spectrum from one ADC channel has been shown in figure 5.2. Using these spectra for each channel, the linear equation between pulse number (in arbitrary units) and the ADC output was obtained as in equation 5.6.

$$Pulse\ height\ (arb) \;=\; parameter1 \times ADC\ output + parameter2 \tag{5.6}$$

In the second step, the equation between pulse height and the energy was evaluated. This was done using a triple-α source that contained the radioactive isotopes; ^{239}Pu, ^{241}Am, and ^{244}Cm, which emit α-particles of known energies (see table 5.1). An example spectrum of the triple-α source is shown in figure 5.3. By

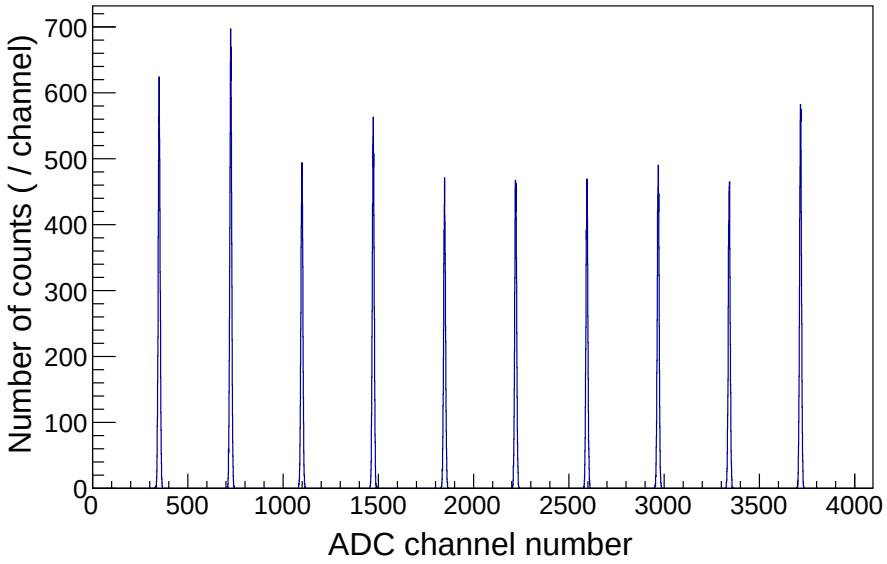

Fig. 5.2 A single ADC channel spectrum of a pulser run. The x-axis values correspond to the ADC output values (ranging 0 - 4096). On the y-axis is the number of pulses per channel.

identifying the three main peaks in the spectra, their corresponding ADC outputs were noted by fitting the peaks. Using those ADC output values in equation 5.6 along with the knowledge of corresponding energies, the relationship between pulse height and energy was obtained as in equation 5.7.

$$\textit{Pulse height (arb)} = \textit{constant} \times \textit{energy} \tag{5.7}$$

Finally, using equations 5.6 and 5.7, the calibration parameters; gain and offset (see equation 5.5) were obtained.

This final relationship between energy and the ADC channel could have been directly obtained by linear fitting the triple-α peak positions. But the energy of α-particles from the source was $\sim$5.5 MeV, whereas the energy of the α particles in the ^{12}C triple-α breakup data extended down to 70 keV. Therefore, the offsets obtained using the pulser runs were better suited for this data analysis.

Detector dead layer correction

The DSSSDs used in the experiment had an approximately 100 nm thick layer of dead material even when fully biased. This meant that α-particles lost some energy

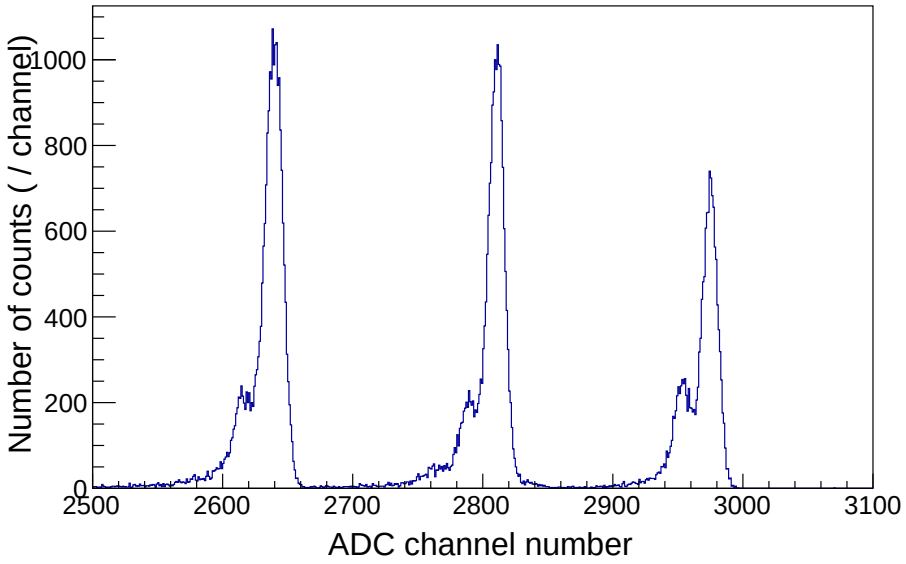

Fig. 5.3 A single ADC channel spectrum of a triple-α source run. As in figure 5.2, the x-axis values correspond to the ADC output values (ranging 0 - 4096). The y-axis is the number of counts per channel.

ΔE_{DL} when passing through the dead layer. The stopping power in any material is dependent on the incident energy of the particle. Therefore, the energy loss, ΔE_{DL}, was different for the α-particles used for the calibration ($\sim$5.5 MeV) and the α-particles from the ^{12}C breakup in the relevant energy range for this work ($\sim$70 keV - 4 MeV). This meant that a correction was required for this detector dead layer effect.

The angle of incidence for particles was different for different strips and for individual pixels on any one strip. The effective dead layer that was seen by a particle was dependent on this angle. Therefore, as the first step, the effective dead layer for each strip was calculated.

In figure 5.4, t is the dead layer thickness, E is the energy of the incident particle, and θ_i is the angle of incidence of the particle on the i_{th} pixel. If $\partial E/\partial x$ is the stopping power at energy E then the energy of the particle after passing the dead layer should be,

$$E_i = E - \frac{t}{\sin\theta_i} \times \frac{\partial E}{\partial x} \tag{5.8}$$

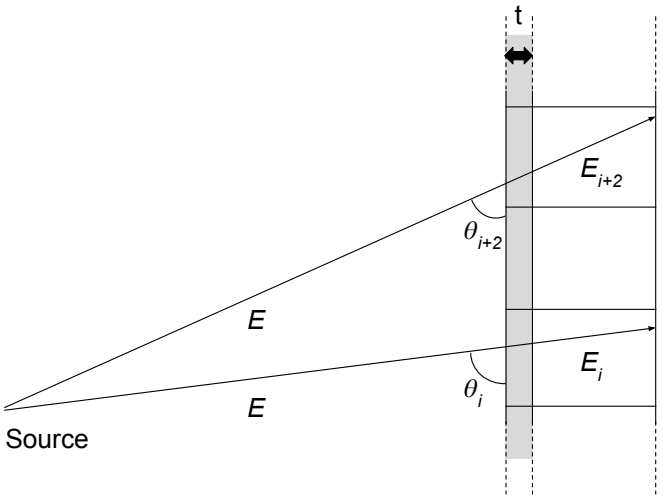

Fig. 5.4 A vertical strip of the detector as seen from the side, showing dead layer of thickness t in grey. An α-particle of energy E, incident on i^{th} pixel enters the active region of the detector with energy E_i.

Simplifying the weighted average of E_i over solid angle Ω_i for all 16 pixels gives,

$$E' = E - t \times \frac{\partial E}{\partial x} \times \sum_{i=1}^{16} \frac{\Omega_i}{\sin\theta_i} \times \frac{1}{\sum_{i=1}^{16} \Omega_i} \tag{5.9}$$

Using equation 5.9, the effective dead layer thickness for each strip was calculated as,

$$DL_{eff} = t \times \sum_{i=1}^{16} \frac{\Omega_i}{\sin\theta_i} \times \frac{1}{\sum_{i=1}^{16} \Omega_i} \tag{5.10}$$

As the next step, the energy of the α-particles from the triple-α source that reached the active volume of the detector were calculated by subtracting the corresponding energy loss in the dead layer. In the calibration process of obtaining gain and offset parameters for equation 5.5, these corrected energies were used.

The calibration parameters obtained gave the energy of the particles that would have reached the active material. In the final step, to get the incident energy of the particles, the estimated energy loss ($\partial E/\partial x \times DL_{eff}$) corresponding to the energy was added to the value.

Foil thickness correction

The energy of a particle from the ^{12}C triple-α breakup that was incident on the detector was not the energy with which the particle was created. The ^{12}N beam was implanted in a stopper foil of thickness 118.2 nm. The implantation depth for a ^{12}N ion with 30 keV/u energy in ^{12}C was calculated to be 61 nm using TRansport of Ions in Matter (TRIM) program calculations. TRIM is a part of the SRIM (Stopping Range and Energy Loss) package that consists of programs that are used for calculating the stopping power and range of ions in matter [57]. This meant that any particle generated in the decay of ^{12}N or in the subsequent breakup of ^{12}C had to travel through the ^{12}C foil for at least 61 nm or 57 nm depending on which side it exited. Therefore, to evaluate the real energy of an α-particle from the breakup, the energy it lost in the stopper foil was added to the energy incident on the detector.

The effective foil thickness was calculated from the angle of emergence of the particle from the foil. The relationship between the particle energy and the stopping power of the α-particles in ^{12}C was calculated using the SRIM software.

5.1.2 Calibration of β-particle detector

The β-particle detector was calibrated using the same procedure, but using an electron source instead of a triple-α source. The radioactive ion in the source was ^{207}Bi, which emits conversion electrons with energies of 481.69, 553.84, 975.65, and 1047.8 keV [58]. The spectrum as recorded on one channel is shown in figure 5.5. There was no need to correct for detector dead layer thickness or the foil thickness while calibrating the β-particle detector because the β-particles (positrons and electrons) do not lose a significant amount of energy in such a small thickness of material. An electron of 1 MeV energy would lose about 0.0049 keV in 61 nm of ^{12}C foil, and about 0.0066 keV in 100 nm of silicon dead layer. These values are based on stopping power calculated from Electron STopping-power And Range (ESTAR) database [59].

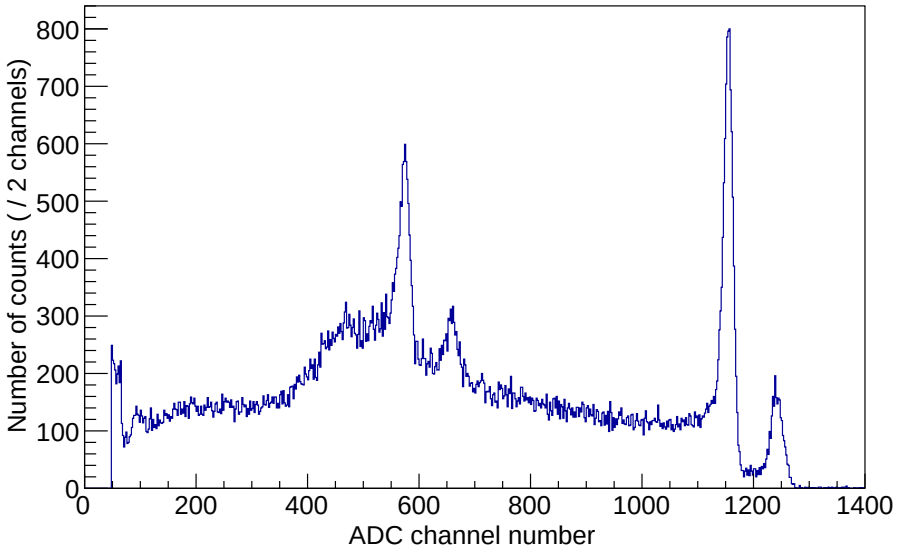

Fig. 5.5 A single ADC channel spectrum of the ^{208}Bi source run. The x-axis values correspond to the ADC output values (ranging 0 - 4096). The y-axis is the number of counts per two channels.

Energy calibration in the low energy region

It was briefly mentioned in chapter 4 that the HPGe detector was used to validate the low energy calibration of the U3 detector. This was done using the ^{60}Co source and studying the Compton scattered γ-particles, scattering off the Si detector and getting absorbed in the HPGe detector. In such events, the particle deposited part of its energy in the Si detector and the rest of the energy in the Ge detector. The ratio of the energies deposited in each detector depends on the scattering angle. Therefore, the source was placed near the bottom right corner of the U3 detector (see figure 4.3) to maximise the range of scattering angles between the U3 and HPGe detectors.

These events can be very clearly seen in a 2D histogram of energy recorded in Si vs energy recorded in Ge. The plot is shown in figure 5.6. The diagonal lines in the plot correspond to the Compton scattering events that were detected. As can be seen in the plot, there are two such lines, each corresponding to two main γ-lines from the ^{60}Co source.

This was done in order to check the validity of the low energy calibration of the U3 detector. This was achieved by checking the intercepts of the aforementioned diagonal lines in figure 5.6 on the x-axis. These lines should have both x- and y-

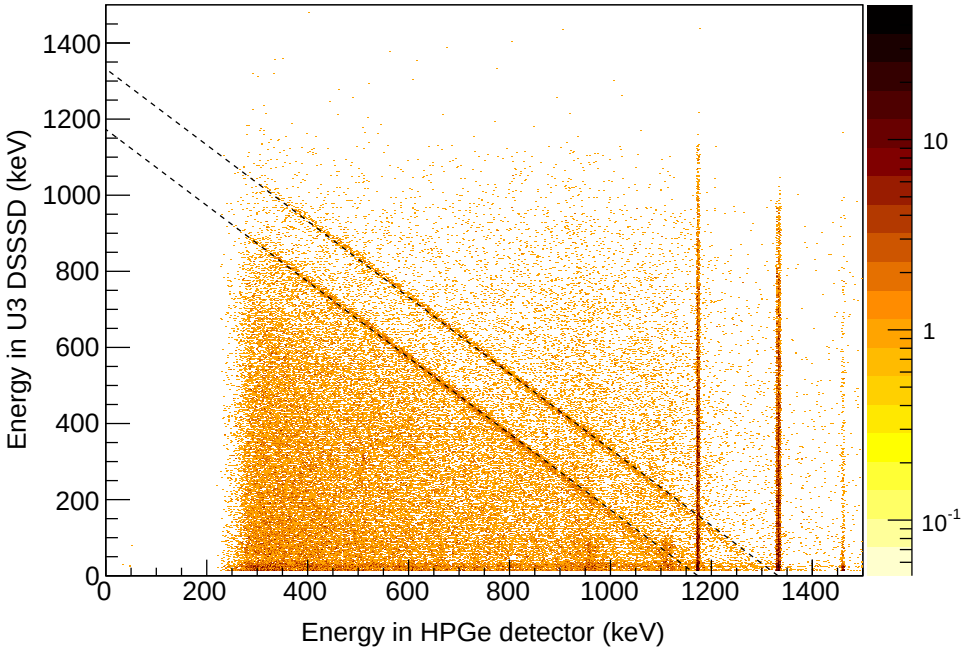

Fig. 5.6 Energy in the U3 DSSSD versus energy in the HPGe detector. The Comton scattered events can be seen as the diagonal lines where a γ-ray deposited part of its energy in the U3 DSSSD and the remaining in the HPGe detector.

intercepts as 1173 and 1332 keV, which are the energies of the two γ-lines from the ^{60}Co source [60]. If the U3 energy calibration was non-linear, the x-axis values corresponding to the low energy values on the y-axis (the Si energy axis) would have been wrong. This would have made the intercepts of diagonal lines on the x-axis vary off the correct values. It can be seen from the plot in figure 5.6 these intercepts were within 10-20 keV of the correct values of 1173 and 1332 keV. This small offset was acceptable as it didn't have any significant impact on analysis as can be seen in following sections.

5.2 Geometrical calibration of the setup

The coordinates of each detector's center were measured using a ruler on the PCB board on which they were mounted. Taking into account the uncertainty in the beam spot on the stopper foil, and the uncertainty in the position of the stopper foil itself, these measurements were accurate to within 2 mm.

The angular correlation measurements (details of which are covered in section 5.7 and 5.8) were sensitive to the geometrical calibration, therefore it was required to get the detector positions in the data analysis as close to the real values as possible. To do that, the two physical aspects of the breakup that were most sensitive to the geometrical calibrations were monitored; the sum of the momenta of all three α-particles, and the energy state of the intermediate ^{8}Be nucleus calculated using the momentum of the second and third α-particles. The former was more sensitive to the detectors' position in their planes, while the latter was more sensitive to detectors' distance from the stopper foil. So, together they provided a good handle on the overall geometrical calibrations of the detector-foil setup. One more thing to mention here is that due to the breakup mechanism of the ^{12}C energy states that were of interest in the present work (0^+ and 2^+ spin-parities), the three α-particles from the breakup mostly hit the detectors opposite to each other. This made it easier to perform tests on the geometrical calibrations, as it meant that only two detectors (either the pair U1 and U6, or the pair U2 and U4) were to be monitored at one time. See figure 4.3 for the detector setup arrangement.

By the law of conservation of momentum, the sum of momentum of α particles from a triple-α breakup should be zero. If the geometrical calibration was done perfectly, histograms of each of the x, y, and z components of the total momentum in the breakup should be centred around zero. Any offset from zero in these histograms would be an indication of an offset in the calibrations. Given the geometry of the setup and the axes definition, the x and z components were coupled, but the y component was independent. Therefore, for the ease of explaining, the y-coordinate has been chosen to show how a change in any of the coordinates would have affected the physical parameters. It can be seen with the help of figure 5.7 how the y-component of the sum of momenta would change if the defined y-coordinates of the detectors were different from the actual setup. Any difference in x- or z-coordinate definition would also affect the y-component of the total momentum, but the effect would be of second order.

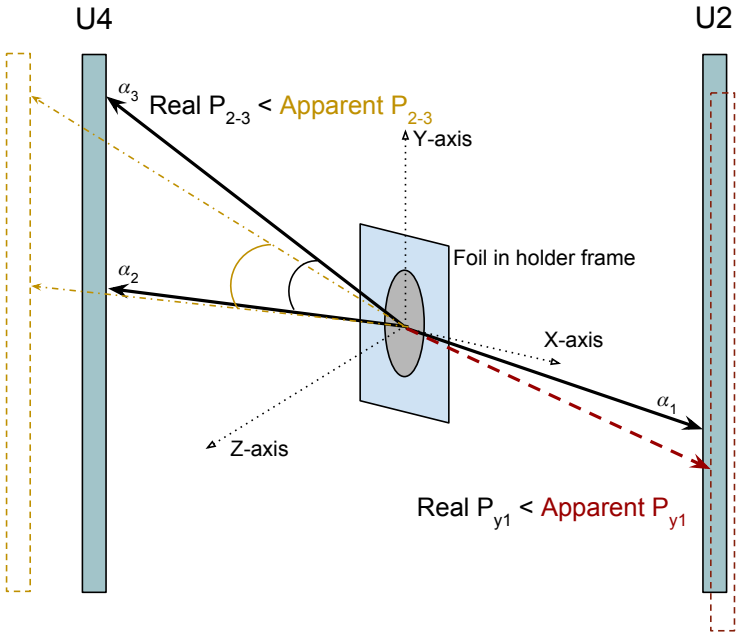

Fig. 5.7 A schematic diagram of the stopper foil and detectors U2 and U4 from the side, looking along the plane of the detectors. The diagram shows how the y-component of the sum of momenta of α-particles from the breakup would change from zero if there was an error in defining the y-coordinate of the detectors. The solid lines show the actual trajectory of particles from the break up, and the dotted lines show the apparent trajectory if the coordinates are defined incorrectly. The diagram also shows how the measured angle between the second and third α-particles would change if the detector position was defined closer or farther than the real position.

The second observable that was monitored for checking the geometrical calibration was the energy state of the intermediate ^{8}Be nucleus. It was calculated using the relative momentum $\vec{P_{23}}$ between the α_2 and α_3 from the breakup. Therefore, it depended on the angle between the momentum vectors $\vec{P_2}$ and $\vec{P_3}$. The details of how it is calculated is covered in section 5.5. This quantity was mainly sensitive to the distance of the detector from the breakup point as is clear in figure 5.7.

The ^{8}Be energy plots were mainly sensitive to the detectors' distance from the stopper foil. In the procedure for obtaining the correct peak energy in these plots, there were two parameters that were varied: the x and z coordinates of the corresponding detector's center. For the P_y component plots also, there were only two parameters that affected the distribution: the y components of each of the detectors in a pair of two facing each other. However, for the x and z component

momentum distribution plots, there were four parameters (x and z coordinates of the two detectors in either pair) that affected the P_x and P_z simultaneously, because the x and z coordinates were coupled in the defined coordinate system. But provided the fact that the detector planes were fixed at a 45^o angle to the axes, the x and z coordinates for the center of a detector were coupled if they were to remain in the detector plane. This reduced the number of parameters from four to two essentially.

Figure 5.8 and 5.9 show the best results that could be achieved simultaneously for momentum distribution plots and the plots of reconstructed energy of the intermediate ^{8}Be nucleus. In figure 5.8 the 1st and 2nd column corresponds to the x and z component of the sum momentum of the α-particles from the breakup. Only x and z components of the sum momentum have been shown because they were coupled and therefore more complicated to center around zero simultaneously. These plots show only those breakup events which took place via the ground state of the ^{8}Be nucleus. As has been mentioned before, due to the breakup mechanism, the α particles from such events were mostly recorded in the detectors facing one another. So, only four detectors are included in these histograms. Which makes all detectors with the exception of U5 as there was no detector opposite to it. The top row shows the histograms with all the events. The middle row shows only those events which were recorded in the detector pair U1 and U6, while the bottom row shows those that were recorded in the pair U2 and U4.

The histograms in figure 5.9 show the energy of the ^{8}Be nucleus, calculated using momenta of α particles that the ^{8}Be nucleus broke into; the α_2 and α_3 in the triple-α breakup. The ground state energy of ^{8}Be is 91.8 keV [61]. The difference between the ground state energy values in these plots from the real value comes from any discrepancy between the defined and real geometrical coordinates of the detectors.

As has been mentioned above, both these observables were monitored together while tweaking the geometrical coordinates of the detector centres. The ideal values for these observables are; zero for momentum distribution, and 91.8 keV for the ^{8}Be ground state energy. These ideal values could not be achieved simultaneously as there

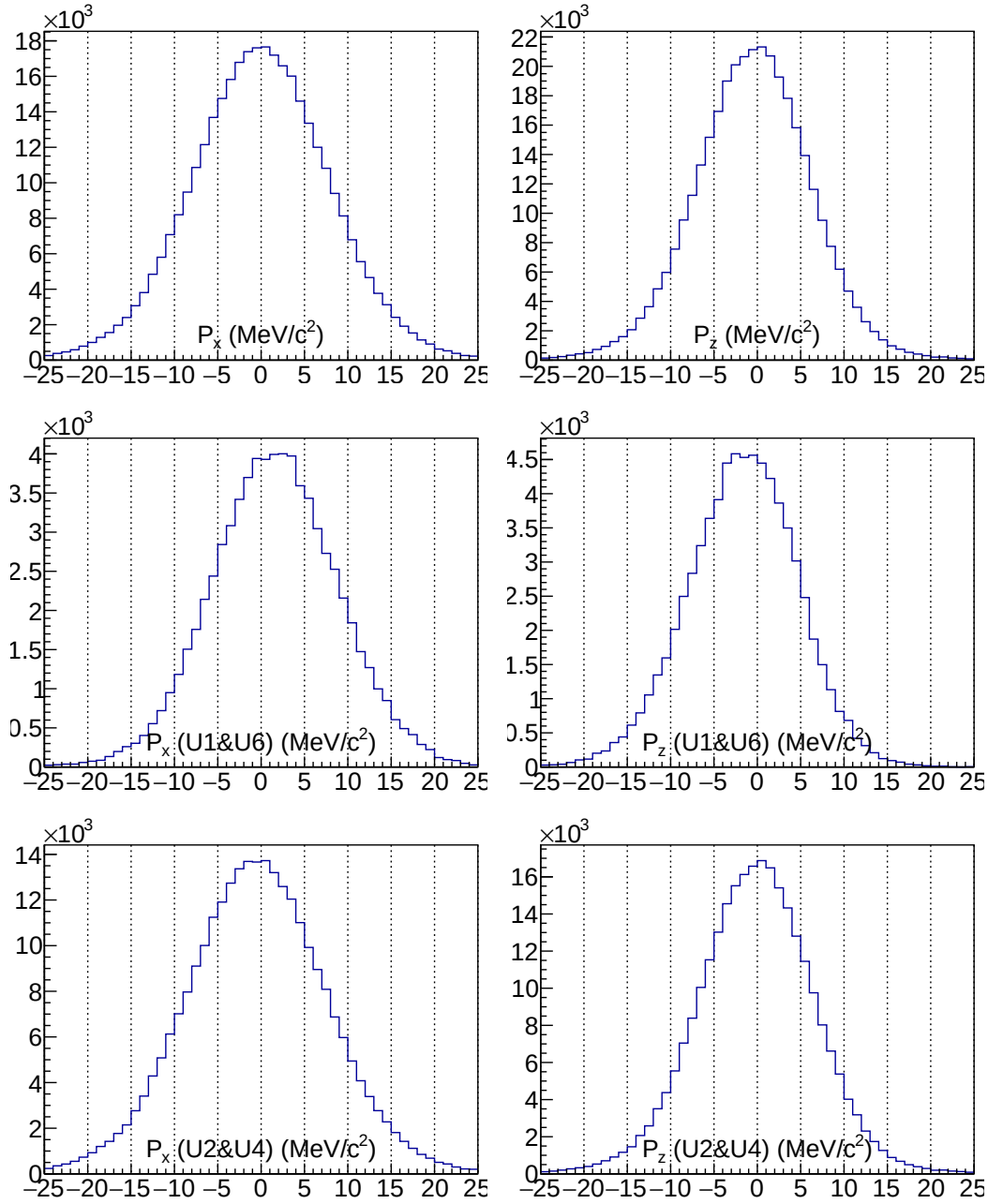

Fig. 5.8 The figure shows the x and z components of the sum of momenta of α-particles from the triple-α breakup of ^{12}C via the ground state of the intermediate ^{8}Be nucleus. The 1st and 2nd column correspond to the x and z component respectively. The top row plots consist of data from all the α-particle detectors. The middle row shows the events recorded in the detector pair U1 and U6. The bottom row shows the events recorded in the detector pair U2 and U4.

seemed to be a trade-off between the two. The explanation behind that observation could be that the values of implantation depth of the ^{12}N ions in the foil and the foil thickness used were not accurate. They depend on the stopping power of the ^{12}N ion in the ^{12}C material, which was obtained using SRIM. Any error in the stopping

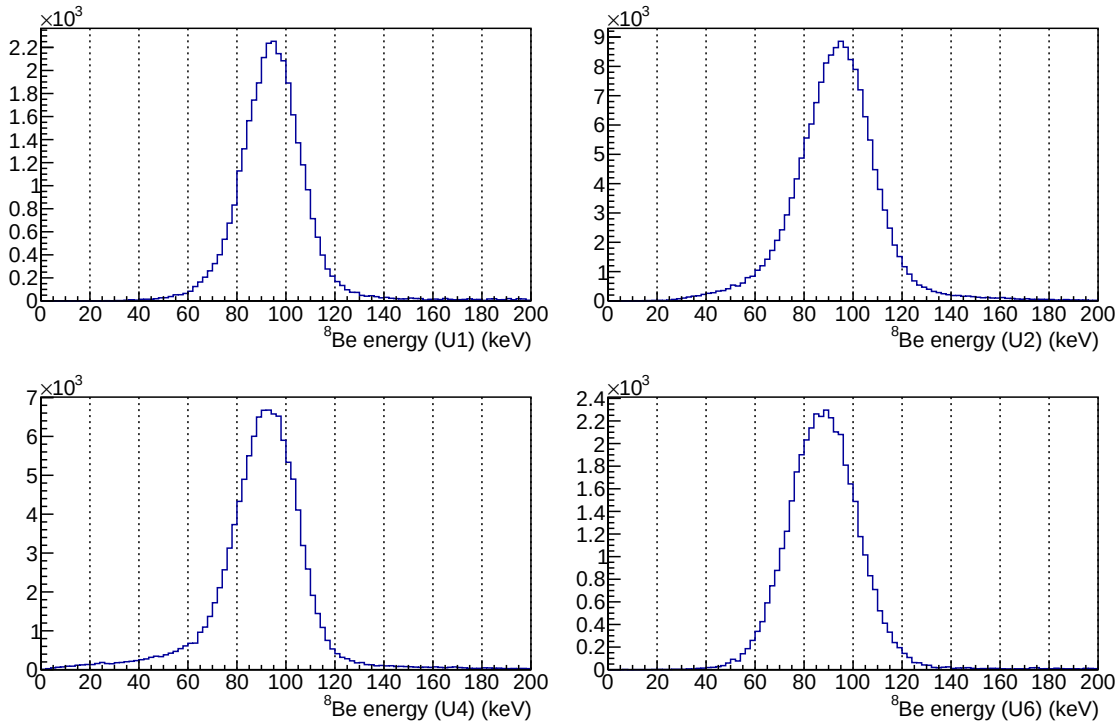

Fig. 5.9 The figure shows the reconstructed energy state of the intermediate ^{8}Be nucleus in the breakup. The energy was calculated using the momenta of α_2- and α_3-particles. Selection of α_2 and α_3 out of the three detected particles was made based on the particles' energies, with the highest energy particle being the first emitted in the breakup. Clockwise from the top-left, the plots show the events where α_2 and α_3 were recorded in U1, U2, U4, and U6 respectively. The peak corresponding to the energy of the ground state of ^{8}Be should be at 91.8 keV. Any deviation from this value comes from the discrepancy between the defined and real geometrical coordinates of the detectors.

power in that database would have lead to a misjudged foil thickness and the ion implantation depth, which would affect the observables in question. Nevertheless, the geometrical coordinates were known within ±2 mm accuracy and the effect of this uncertainty on angular correlations and on further results was calculated. These uncertainty calculations have been detailed in section 5.8.

5.3 Foil thickness calculation

The thickness of the stopper foil was measured before and after the beam time run. To measure the foil thickness, the triple-α source was shone onto the U2 detector through the stopper foil. By calculating the difference between the measured energy

and the known energy of the α-particles, along with the stopping power of the foil material, ^{12}C, for the α-particles of $\sim$5.5 MeV energy, the foil thickness was calculated using the equation, $t_{foil} = \Delta E_{foil}$ / *stopping power*. Detector U2 was selected based on the convenience given the setup as it was. The results of the measurements and calculations before and after the beam-run have been given in table 5.1. The growth in the foil thickness can be attributed to the deposition of beam ions and vacuum impurities.

Isotope	Energy (keV)	Stopping power (keV/nm)	Before beam run		After beam run	
			ΔE_{foil} (keV)	t_{foil} (nm)	ΔE_{foil} (keV)	t_{foil} (nm)
^{239}Pu	5156.6	0.177	18.2	102.6	25.2	142.1
^{241}Am	5485.6	0.170	16.5	96.8	22.8	133.8
^{244}Cm	5804.8	0.164	16.0	97.6	22.3	136.0
				Avg: 99.0		Avg: 137.3

Table 5.1 The table shows the calculation of stopper foil thickness using the triple-α source. The measurements were carried out at the beginning of the experiment (before the beam-run) and then again at the end of the beam run.

5.4 Data reduction

This section contains the details of the how the data was sifted through different cuts and gates to ensure the best removal of false (background and noise) events. Once the total number of true events was identified, using the detection efficiency as obtained from the Monte Carlo simulation in section 5.4, the ^{12}N ion yield was calculated.

5.4.1 Real triple-α hits identification

For identifying a real particle hit from the background or noise, a series of cuts and acceptance criterion were applied to the data.

ADC threshold: As has been mentioned previously in section 4.3.4, while recording the data during the experiment, a readout threshold was set for each ADC channel using the MIDAS data acquisition. In the data analysis, similar or slightly higher values of thresholds were implemented to cut out the low level noise in each strip. The ADC thresholds were varied a few times over the course of experiment. The typical energy equivalent threshold values were between 40 - 250 keV. For the sake of keeping further analysis less complicated, only one set of values (the highest ones) was used for all the runs. Figure 5.10 shows the difference between the acceptance with low and high threshold cutoffs. The spectrum shown is the reconstructed ^{12}C excitation energy. The details of the reconstruction are covered in the next section. The curve in blue is accepted data with low cutoffs and the one shown in red is with the higher cutoffs. The total difference between the statistics in the two cases is of the order of 10%. As can be seen from the figure 5.10, the effect is most prominent in the 10 MeV region. However, in this region there is high enough statistics even with the higher cutoffs, therefore, it was justified to use the higher cutoffs for the whole dataset analysis.

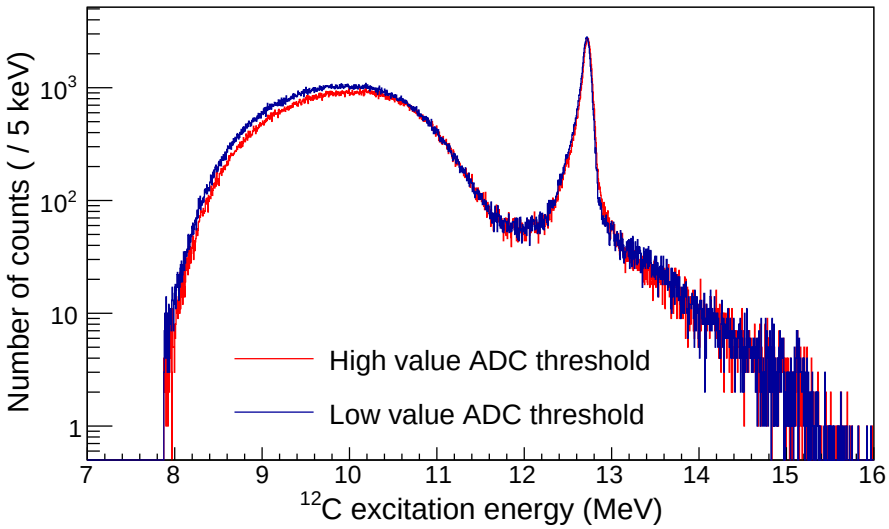

Fig. 5.10 The figure shows the comparison between the acceptances when low (in blue) or high (in red) cutoffs are applied to the data. On the x-axis is the reconstructed ^{12}C excitation energy and on the y-axis is the number of counts per 5 keV.

Front-back energy matching: If a particle hits the detector in the middle of a pixel, *i.e.*, not in the inter-strip region, it must have deposited similar energy in the two channels corresponding to the front strip and the back strip. The typical energy resolution of the detectors was 25-30 keV FWHM. Motivated by the resolution, the acceptance criterion was set to be $\mid E_F - E_B \mid < 60$ keV.

In some instances, there were two particles of very similar energy that hit the same detector in two different pixels. In that case, there were two possible pairs identified by the front-back energy matching criteria. In order to select the true one of the two pairs, the pair with the lower value for ($\mid E_F - E_B \mid_{particle1} + \mid E_F - E_B \mid_{particle2}$) was chosen.

Minimum three identified hits: Only those events which had at least three identified α-particle hits were selected for further analysis.

Total energy and momentum: To further cut down the low level noise from the data, a lower limit of 600 keV was set on the acceptable total energy. Finally, to ensure that the three identified particles were indeed the three α-particles from a ^{12}C breakup, the data was gated on the events which had total momentum, $P_{sum} < 35$ MeV/c^2, and had $P_{sum} < (E_{sum}/90 + 10)$. These cuts have been shown graphically in figure 5.11.

5.4.2 Real β-particle hit identification

The previous subsection explained how the real triple-α hits were identified and how the noise and background was filtered out from the α-particle detectors. A similar procedure was followed for the β-particle detector. The first part was the same, i.e., applying the readout thresholds and the front-back energy matching. But this time, since it was the β-particle detection being dealt with, special care was taken while applying the readout thresholds. The same energy β-particle can deposit a different amount of energy in the detector depending on the angle of incidence. The apparent thickness of the detector to the particle is different for different angles of incidence. Therefore, to avoid an angular dependency on the β-particle acceptance, the readout

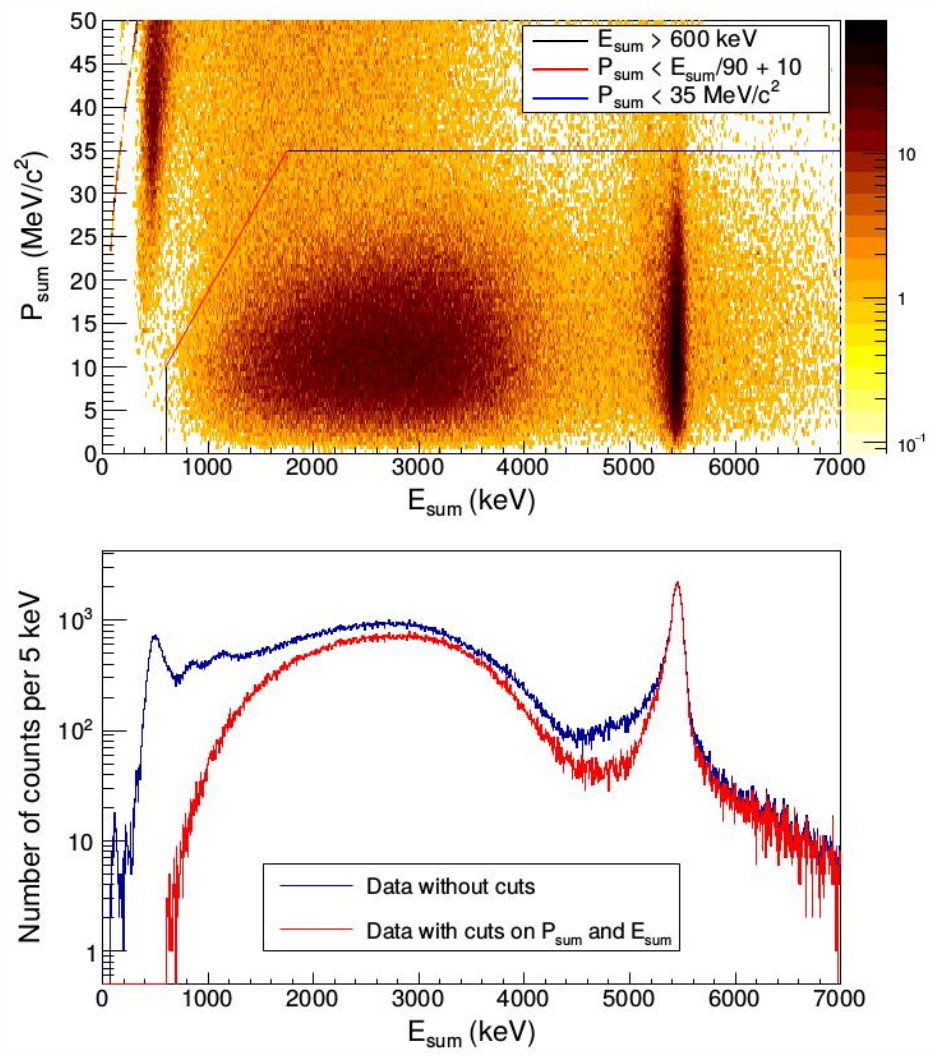

Fig. 5.11 The top figure shows the total energy and total momentum cuts graphically in the 2D histogram of P_{sum} vs E_{sum}. The bottom figure shows the effects of these cuts on the total E_{sum} spectrum.

threshold in the analysis was set by considering the spectrum on the strips which have the smallest angle of incidence, i.e., the strips in the middle of the detector. The β-particle spectra for the bottom, middle, and top parts of the detector have been compared in figure 5.12. In blue is shown the spectrum for the middle part, and it can be clearly seen that the spectrum peak is at a lower energy than compared to the spectra for the bottom (shown in black) or the top (shown in red) part of the detector. The readout threshold was set to be at 200 keV to ensure that all the β-particle events were accepted.

In addition to the readout thresholds and the front-back energy matching, TDC gates were also applied on the β-detectors. By looking at the TDC data, the peak

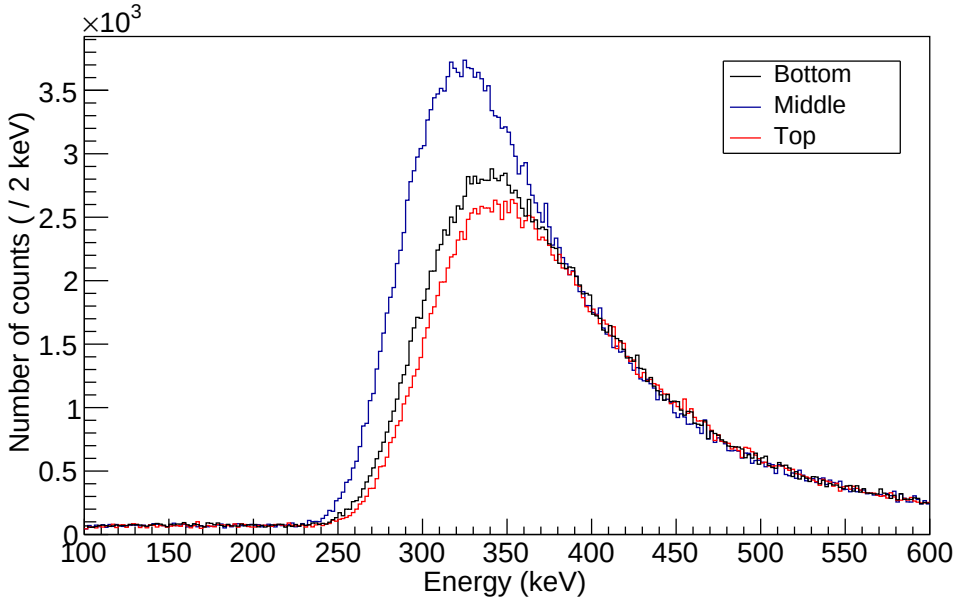

Fig. 5.12 The figure shows the β-particle spectrum as recorded in bottom, middle, and top parts of the detectors in black, blue and red respectively. The x-axis is the energy of the particles in keV and the y-axis is the number of counts per two keV.

position corresponding to the real hits was identified. Any hit on a channel with a TDC value outside of peak range was then discarded as low level noise. Figure 5.13 shows the TDC spectrum for one specific TDC channel.

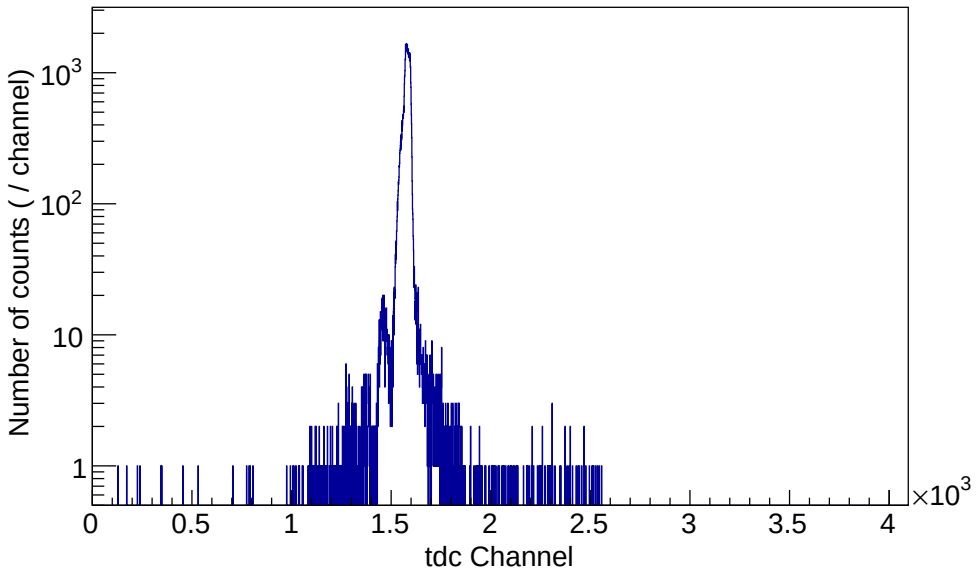

Fig. 5.13 A single TDC channel spectrum of the ^{208}Bi source run. The x-axis corresponds to the TDC output values (ranging 0-4096). The y-axis is the number of counts per channel.

5.4.3 Yield estimate

An account of how many events survived after each gate was applied has been given in table 5.2.

Gate/Criteria	Number of events
Raw	353,123,805
ADC threshold	206,901,658
(Front-back energy matching + real pair identification)	181,248,889
Minimum three identified hits	785,963
$E_{sum} < 600$ keV	756,267
$P_{sum} < 35$ MeV/c^2	463,319
$P_{sum} < (E_{sum}/90 + 10)$	457,439
Coincident β-particle detection	33,393

Table 5.2 The table shows the number of events that survive after every step of data reduction.

To calculate the average yield of ^{12}N ions in the experimental chamber, the total number of counts in the 12.71 MeV state were used. The number of counts in the 12.7 MeV peak between 12.3 and 12.9 MeV were calculated to be 7.6×10^4 over $\sim$151 hours of beam time. The overall efficiency of the setup for the 12.7 MeV 1^+ state was calculated using the Monte Carlo simulation in the work [62] as 0.076. The branching ratio of the ^{12}N β-decay to the ^{12}C 12.7 MeV state is 0.12 % [30]. So, using these numbers, the average yield was estimated to be 1533 ^{12}N ions/s.

5.5 Monte Carlo simulation

In the work presented in this thesis, we are dealing with β-triple-α coincidence detection. The detection efficiency of the setup for this experiment was dependent on a number of things including the triple-α breakup mechanism. Therefore, it could not be simply calculated from the detectors' efficiency combined with the geometrical efficiency as can be done for single particle detection. Moreover, the

detection efficiency in the low energy region was dominated by the ADC readout thresholds and the analysis thresholds. Therefore, a simulation of the experiment was required in order to calculate the detection efficiency. The simulation was also required to obtain the geometrical acceptance of the setup, which was crucial for the β-α angular correlation analysis.

The main base of the simulation was developed by our collaborators at Aarhus University. This base structure included the specifics of the experiment such as the beam spot size, the $\beta\nu$ recoil from the β-decay, the phase-space of the triple-α breakup allowed by the energy and momentum conservation laws, the α-particle detectors' description, energy losses in the foil thickness and the detector dead layer, and the detectors' response to the particles. The detailed procedure of the simulation have been given in [62].

For the work presented here, an addition of the β-particle detector (U3) was made to the base simulation. Optimisation of the geometry of the α-particle detector setup was also added. Specifically, the coordinates of the center of these detectors were changed to the values obtained by geometrical calibrations as has been discussed in section 5.2. The coordinates used in the analysis and the simulation have been given in table 4.1.

To obtain the detection efficiency of the setup as a function of ^{12}C excitation energy, the simulation was run for eight different triple-α breakup Q-values in the 8 - 12 MeV excitation energy region. The simulated data was analysed using the same procedure and scripts that were used to analyse the experimental data. For each Q-value, 10^7 events were simulated. The ratio of number of events that survived the whole data reduction routine to 10^7 was taken as the detection efficiency of the setup for that Q-value. The final efficiency curve has been shown in figure 5.14. As can be seen from the figure, efficiency versus energy function had a smooth curve behaviour. Hence, interpolation was used to get the efficiency for the energies in between any data points in the plot in figure 5.14.

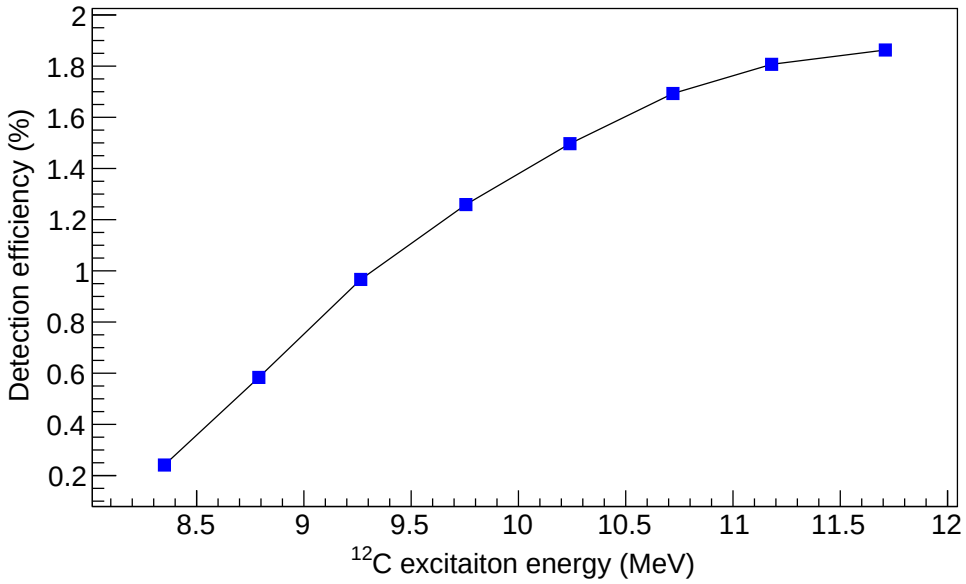

Fig. 5.14 Detection efficiency of the setup as a function of ^{12}C excitation energy. This figure only shows the setup efficiency for the breakup channel via the ^{8}Be ground state.

The geometrical acceptance of the system for β-α angular correlation was extracted by plotting the number of β-triple-α coincidence events against the $\theta_{\beta-\alpha}$, the angle between the β-particle and the α_1-particle. More details on this have been covered in section 5.7.

5.6 Kinematic reconstruction

Using the measured energies and momenta of the α-particles, it was possible to perform the complete kinematic reconstruction of the breakup. What is meant by 'complete kinematic reconstruction' is the extraction of the excitation energy of the ^{12}C nucleus and of the intermediate ^{8}Be nucleus in the breakup, as well as the identification of the breakup channel. This is detailed in the following two subsections.

5.6.1 ^{12}C energy spectrum and the breakup channels

The excitation energy of the ^{12}C nucleus was calculated using conservation of energy. To do that, the ^{12}C triple-α threshold was added to the sum of kinetic energies of the three α-particles from the breakup.

To visually identify the breakup channel, the total energy of the breakup was plotted against the individual α-particle's energy. The resulting plot has been shown in figure 5.15. The main feature which stands out in this 2D histogram is that the way the energy is distributed amongst the three α-particles in a breakup is very different for the energy state at 12.7 MeV and the broad resonance at ∼10 MeV. For the 12.7 MeV state all three α-particles' energies fall into three separate groups along the x-axis, while for the broad strength at 10 MeV the highest energy α particle very distinctly lies on the line of slope 2/3, and the remaining two α-particles' energies lie very close to each other's in the group centred around a line of slope 1/6.

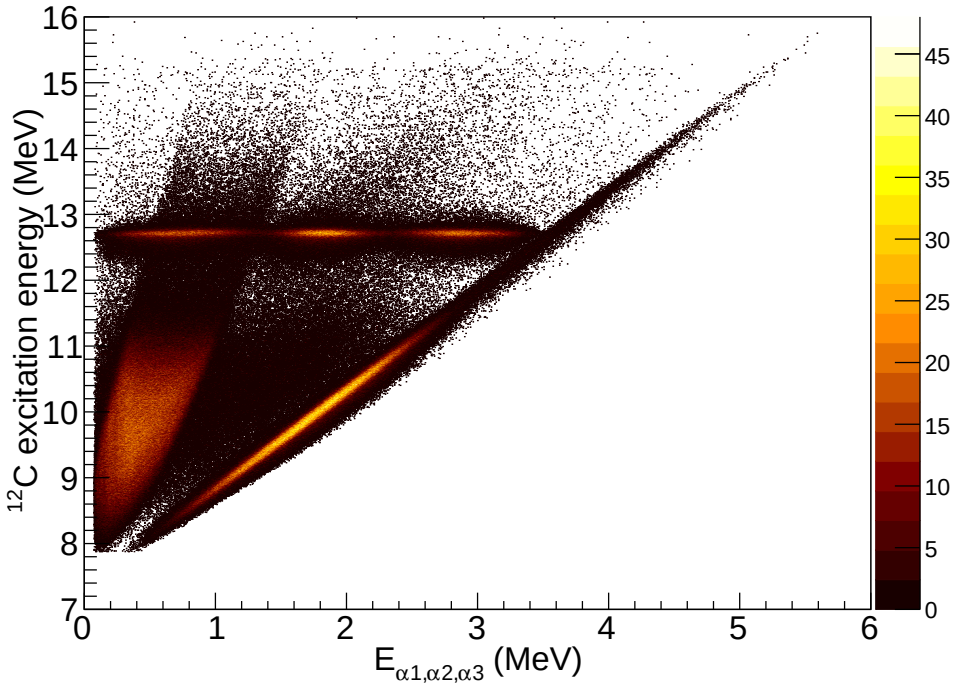

Fig. 5.15 The figure shows the reconstructed excitation energy of the ^{12}C nucleus on the y-axis, plotted against the energy of individual α particles from the breakup. This plot shows the difference between the kinematics of breakup mechanisms from different breakup channels.

The strength in the 10 MeV region consists of resonances of spin-parities 0^+ or 2^+. These spin-parity states breakup mainly via the ground state of the ^{8}Be nucleus. By simple kinematics, it is therefore apparent that the first α-particle from such a breakup takes away two-thirds of the available energy, the ^{12}C excitation energy minus the α-emission threshold. The second and third α-particles shared the remaining one-third of the energy plus the 91.8 keV, the ground state energy of ^{8}Be. The 12.7 MeV state has the spin-parity 1^+. Therefore, due to the conservation of angular momentum and parity, this state could only breakup via the 2^+ excited state in the intermediate ^{8}Be nucleus which lies at 3.03 MeV energy with 1.5 MeV width [61]. Therefore, the energy distribution in this breakup looks very different, with α_1 lying in the middle group, and α_2 and α_3 lying in the groups on the either side (see figure 5.15).

5.6.2 ^{8}Be energy spectrum

For a sequential breakup (eq 5.2 and 5.3), the energy of the intermediate ^{8}Be nucleus could be reconstructed using the relative momenta of its breakup products, α_2 and α_3, by using the equation,

$$E_{^8\mathrm{Be}} = 2\frac{\vec{p_{23}}^{\,2}}{2m_\alpha} \tag{5.11}$$

where, $\vec{p_{23}} = \frac{1}{2}(\vec{p_2} - \vec{p_3})$

Figure 5.16 shows a histogram of the ^{8}Be reconstructed energy for all the triple-α events recorded. The very clear peak that shows at 91.8 keV, corresponds to the ground state of ^{8}Be. For the selective analysis on the breakups that took place via the ground state of ^{8}Be, the data was gated on the events in the ground state peak only (*i.e.*, $\mathrm{E}_{^8Be} < 120$ keV).

The effect of gating the data on different breakup channels using the ^{8}Be energy can be seen very clearly in figure 5.17. This figure shows the same plots as the one in figure 5.15, but with the data gated on one breakup channel or the other. The top one contains the events gated on the ^{8}Be ground state peak from figure 5.16. While the bottom plot contains all the other events. As has been explained before, the

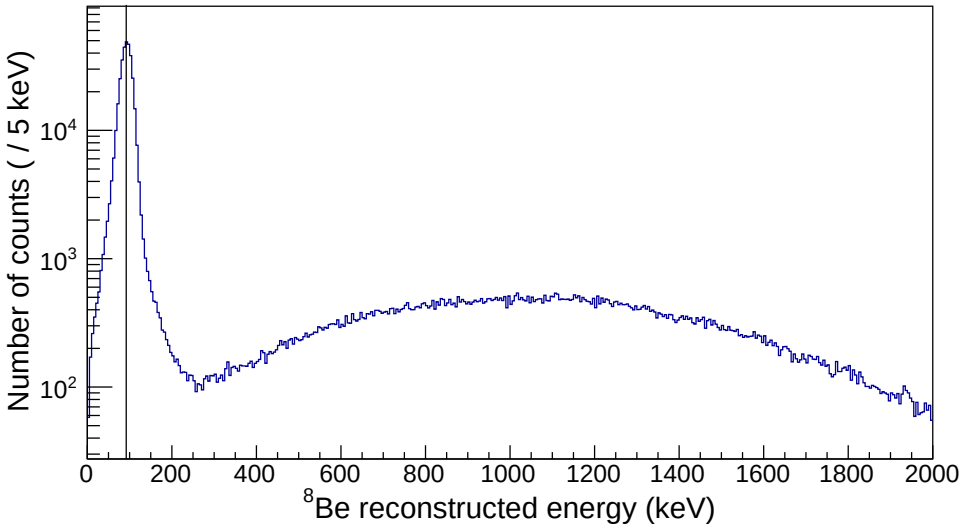

Fig. 5.16 The figure shows the energy of the intermediate ^{8}Be nucleus reconstructed from the relative momentum of α_2 and α_3. The peak at 91.8 keV corresponds to the events where the breakup happened via the ground state of ^{8}Be.

12.7 MeV 1^+ state cannot breakup via the ground state of ^{8}Be due to the angular momentum and parity conservation. Figure 5.17 (top) presents the evidence for this statement.

5.7 Angular correlation plots

Once the data was cleaned of any possible noise or background, the $\beta - \alpha$ angular correlations were analysed as a function of ^{12}C excitation energy. The $\beta - \alpha$ angular correlation should be isotropic for the breakup of the 0^+ state and any anisotropy would suggest the presence of a 2^+ strength. Therefore, the main idea was to scan the energy region of interest in small sections (500 keV wide bins), and evaluate the strength profile of the 2^+ state by analysing how the anisotropy in the $\beta - \alpha$ angular correlations evolve.

The angular correlations were studied for each breakup channel separately. The analysis presented in this section was performed on the data gated on the breakup channel via ground state of ^{8}Be. The β-triple-α data was first divided into regions of ^{12}C excitation energy. For each energy region, a histogram of $\theta_{\beta\alpha}$ (the angle between the direction vectors of β and α_1 particles) was made. One sample of these

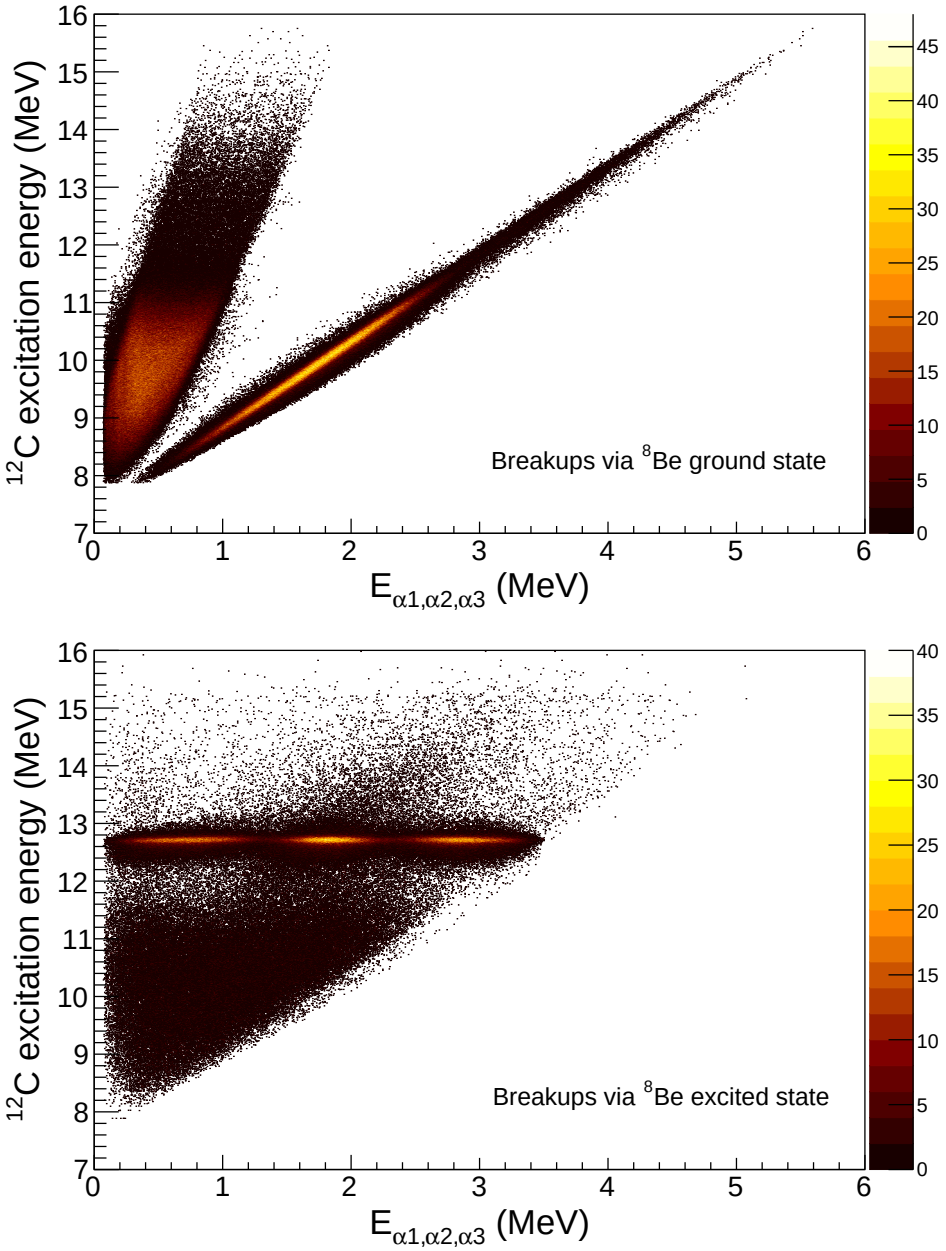

Fig. 5.17 The figure shows the data gated on different breakup channels using the ^{8}Be energy plot. The top plot only contains the events that fall in the ^{8}Be ground state peak in figure 5.16. It can be seen that the 12.7 MeV 1^{+} state of ^{12}C does not show in the top plot as it cannot breakup via the 0^{+} ground state of ^{8}Be. The bottom plot shows the events where the breakup took place via the 2^{+} excited state of ^{8}Be.

histograms for the energy region 10 - 10.5 MeV is shown in figure 5.18 in blue. The most noticeable feature of the histograms shown is the three bumps structure. This structure was mostly due to the geometrical acceptance of the setup, and partly due to the different ADC thresholds on different detectors. The detector array did not

have the full 4π coverage, but instead had gaps between the detectors. Those gaps between the detectors correspond to the dips in the angular correlation histograms. Therefore, the angular correlation histograms of the simulated isotropic breakup events showed the same features as the histograms of the experimental data. The simulated histogram for the same energy region has been shown in red in figure 5.18.

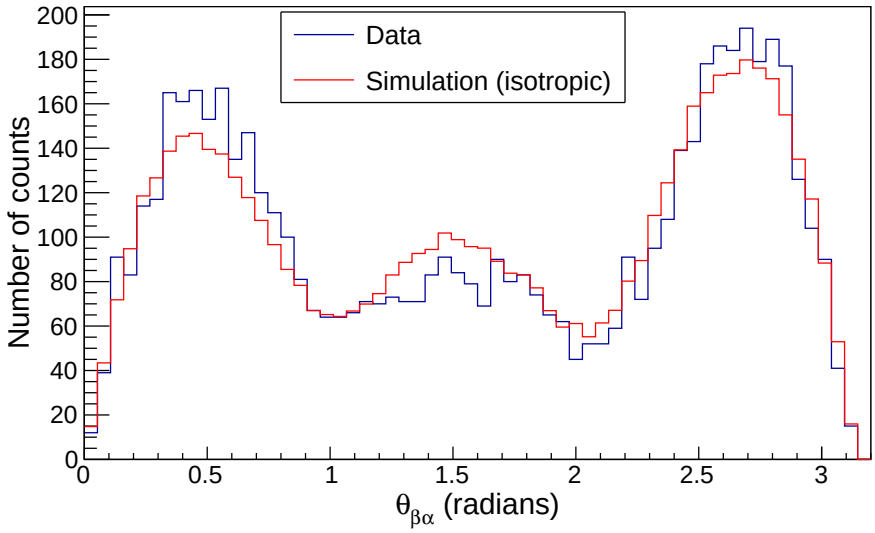

Fig. 5.18 The figure shows the angular correlation histograms; number of counts versus $\theta_{\beta-\alpha}$, for ^{12}C excitation energy 10 - 10.5 MeV. The histogram in blue shows the real data and the red shows the simulated events. These plots are uncorrected for geometrical acceptance and setup efficiency.

A quantitative analysis was performed on these these angular correlations for each energy region to obtain the behaviour of anisotropy as a function of ^{12}C excitation energy. This analysis involved multiple steps which have been described in detail as follows.

1. The data was first divided into six regions between 9.0 and 12.0 MeV excitation energy, and the angular correlation histograms were plotted for each region.

2. The angular correlation plots from the data alone do not give any quantitative information on the anisotropy as their features are mainly dominated by the geometrical acceptance and the efficiency of the setup. Therefore, simulations were performed for all the six energy regions to get a handle on the effect of geometrical acceptance and the efficiency of the setup on the angular correlation

plots. The breakup Q-values in the simulation were set as the data weighted mean of each region (1990, 2480, 2965, 3445, 3905, and 4435 keV).

3. Since the simulated events had an isotropic $\beta - \alpha$ angular distribution, the angular correlation histograms produced using those events had the theoretical behaviour of the 0^+ state's decay. To get the equivalent (theoretical) histograms for the 2^+ state's decay, the isotropic behaviour (or, the 0^+ behaviour) histograms were scaled to the 2^+ state's decay distribution function which has been derived in chapter 3 in section 3.2.2, equation 3.11,

$$W(\theta) = 1 + A_2(\beta)A_2(\alpha)P_2(cos\theta)$$

The value of the coefficient $A_2(\beta)$ varies on a case by case basis and for this case of ^{12}N β-decay, the value of $A_2(\beta)$ was unknown. The value of $A_2(\alpha)$ is calculable, but only with the access to the complete wave function. Furthermore, it was unnecessary for the main objective of this work, which was to obtain the relative anisotropy and not the absolute values. Hence, the $A_2(\alpha)$ coefficient was set to be 0.32 as calculated in chapter 3, and the $A_2(\beta)$ coefficient was left as the free parameter 'A' in the fitting procedure.

4. For each energy region, the data histogram was fitted to a combination of the pure 0^+ and pure 2^+ decay behaviours as obtained from simulations in step 3. The combination function used was,

$$f = b \times 2^+_{simulated} + (1 - b) \times 0^+_{simulated} \tag{5.12}$$

where, b was the fraction of the 2^+ state contribution and *(1-b)* was the 0^+ strength component.

5. Fitting was done by varying the above described A and b parameters and minimising the χ^2 function,

$$\chi^2 = \sum_{i=1}^{bins} \frac{(f_i - y_i)^2}{max(y_i, 1)}$$

where, y_i was the ith bin's value in the data histograms.

The above described fitting procedure has been shown for one energy region 10 - 10.5 MeV in figure 5.19. The top panel is showing the comparison of the angular correlation histograms of data with simulation. The data histogram is shown as a solid blue line, the original simulation (the 0^+ behaviour) is shown as a dotted red line, and the simulation histogram scaled to the angular correlation function of the 2^+ state is shown as a dotted black line. This comparison clearly shows that the real data does not have an isotropic behaviour, indicating the presence of a 2^+ strength in the region. The middle section shows the χ^2 value as a function of the product b*A. From this plot, the value of b*A corresponding to the minima of the curve was extracted as the best fit value of the parameters. The 1σ error on the b*A value was also extracted from these plots by taking the difference between b*$A(\chi^2_{min})$ and b*$A(\chi^2_{min}\pm1)$. The bottom panel finally shows the data plot as the solid blue line superimposed with the combined (0^+ and 2^+) simulated histogram as the dotted green line. The values of b*A that were obtained from the χ^2 minimisation were used in the combination equation, equation 5.12, to obtain this fit.

Another method was used to visualise the anisotropy in the angular correlation plots. The experimental data plots were normalised to the simulated data plots. This normalisation action corrected the plots for the aforementioned effects of geometrical acceptance and the efficiency of the setup. The normalised data should have a flat line behaviour for a pure isotropic angular correlation. Again, the excitation energy region of 10 -10.5 MeV has been used to present a sample of this normalisation. Figure 5.20 shows the normalised data along with the best-fit. The fitting function

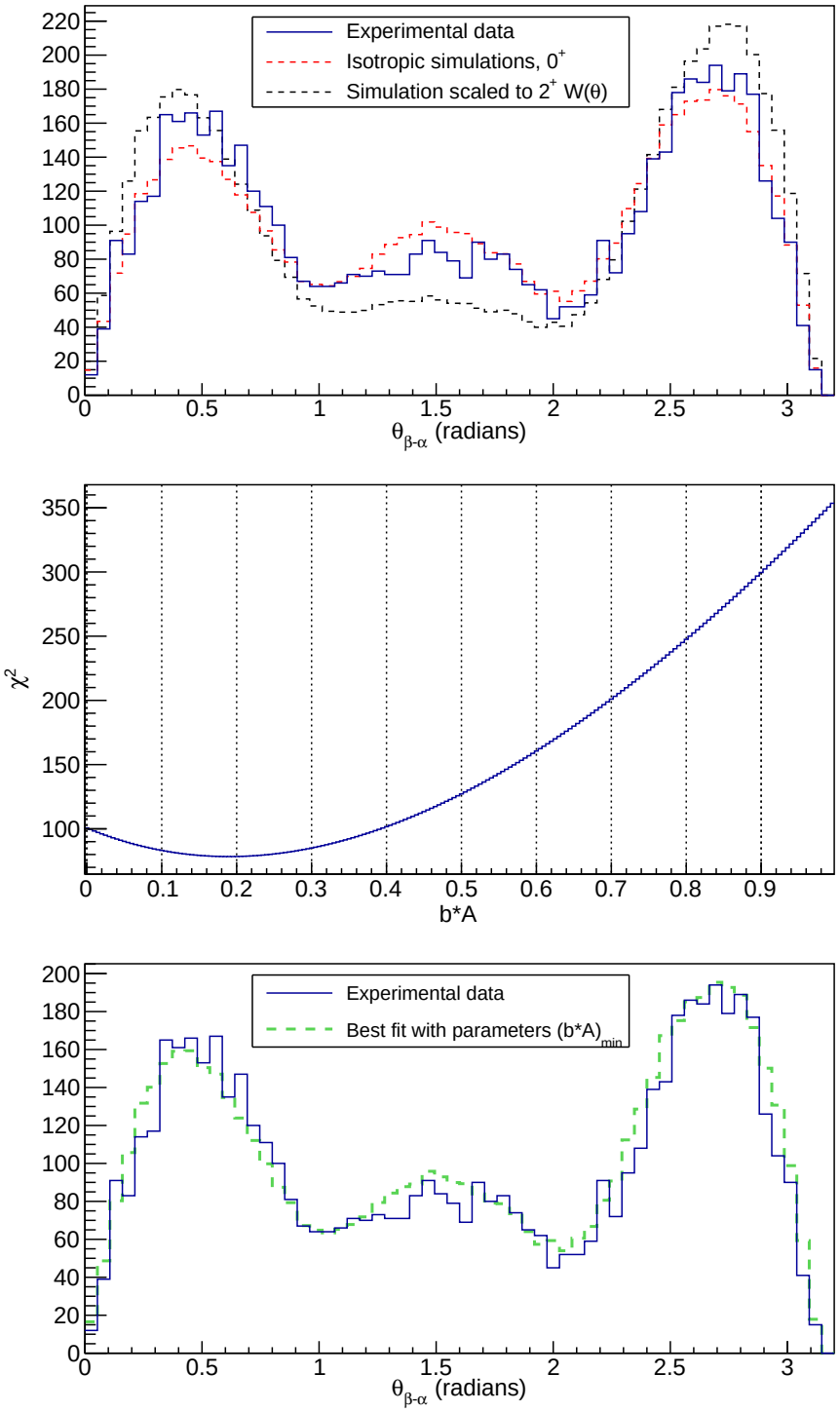

Fig. 5.19 The figure shows the fitting procedure of the angular correlation histograms (for the ^{12}C excitation energy region 10 - 10.5 MeV). The top panel shows experimental data as solid blue line and the simulated histograms for pure 0^+ and 2^+ state's as the dotted red and black lines respectively. The middle panel shows the χ^2 values as a function of the product b*A, where b and A are the parameters used in the fitting function. The bottom panel shows the real data histogram (solid blue line) along with the fit obtained by combining the simulated 0^+ and 2^+ histograms (dotted green line).

used was exactly the same as described above with figure 5.19, and gave the same values of the product b^*A.

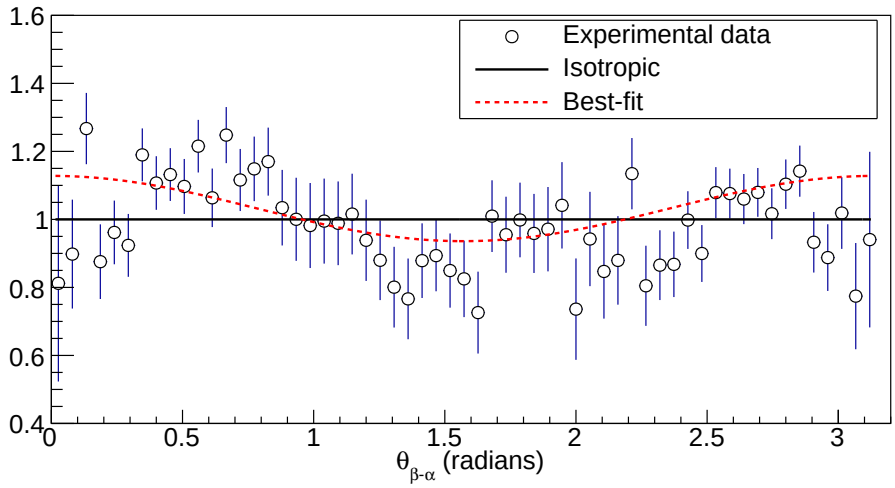

Fig. 5.20 The figure shows the angular correlation plot of the experimental data (for the ^{12}C excitation energy region 10 - 10.5 MeV) normalised to the simulation, hence, corrected for the geometrical acceptance and the efficiency of the setup. The best-fit to the data has also been shown with dotted red line.

The values of b^*A that were obtained by χ^2 minimisation in all the energy regions, together gave the strength profile of the 2^+ state. The details of this strength function are discussed in the next chapter in section 6.1.

5.8 Geometrical uncertainties

In section 5.2, it was mentioned that the angular correlation plots were sensitive to the geometrical calibration. To quantify the effect of any uncertainty in the geometrical coordinates of the detectors on the angular correlation plots, the position coordinates of detector U3 were changed by 2 mm in both radial and angular directions. The decision to only tweak U3's position for this sensitivity study was based on the argument that being the only β-particle detector, it had the biggest effect on the $\beta - \alpha$ angular correlation plots.

Firstly, the direct effect of the difference between the detection setup geometry and the analysis geometry on the angular correlation plots was measured. For this, the simulation was performed using one set of geometric coordinates and the analysis

was done using, first, the same set, and then a different set of geometric coordinates. The comparison between the two cases has been shown in figure 5.21. The blue line histogram shows the angular correlation when the simulation and analysis were done using the same geometry description. In red and black are shown the angular correlation histograms when in the analysis the U3 detector position was taken to be 2 mm farther and 2 mm sideways upstream respectively. As can be seen from figure 5.21, there is no schematic difference between the angular correlation plots for the different cases. So, from this plot it was concluded qualitatively that the error due to geometrical uncertainty was overshadowed by the statistical fluctuation.

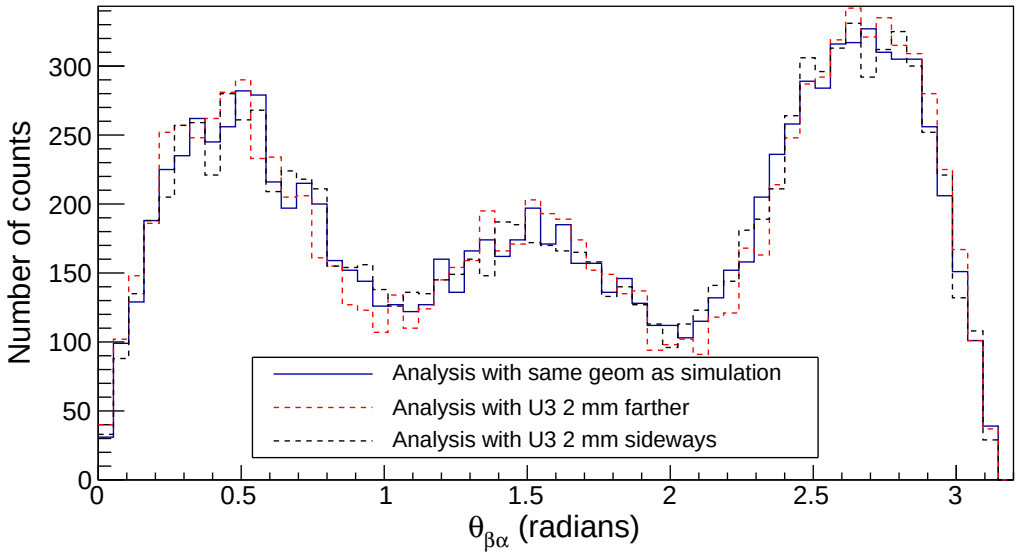

Fig. 5.21 The figure shows the $\beta - \alpha$ angular correlation plots for simulated events (for the ^{12}C excitation energy region 10 - 10.5 MeV). The blue line histogram was made by analysing the events using the same geometry that was used for simulation, while the other two were made by using different coordinates for the U3 detector center in the analysis than in the simulation. The U3 detector was placed 2 mm farther and 2 mm sideways (upstream) in the analysis to create the red line and black line histograms respectively.

To quantify the error on the 2^+ state's strength profile due to geometrical uncertainties, the change in the value of b^*A obtained from fitting the data to simulation by using different geometries was evaluated. The three different χ^2 versus a^*A plots have been shown in figure 5.22. The blue line corresponds to the analysis with geometrical coordinates that were obtained via the combination of measurements using a ruler at the experimental setup and the calibration procedure followed in

section 5.2. The red and black lines correspond to the analysis with the U3 detector position 2 mm farther and 2 mm sideways upstream respectively. As can be seen from these plots, the difference in the b^*A values corresponding to the χ^2 minima of each curve is less than the 1σ error. So, in conclusion, the geometrical uncertainties were smaller than the statistical uncertainties in this work.

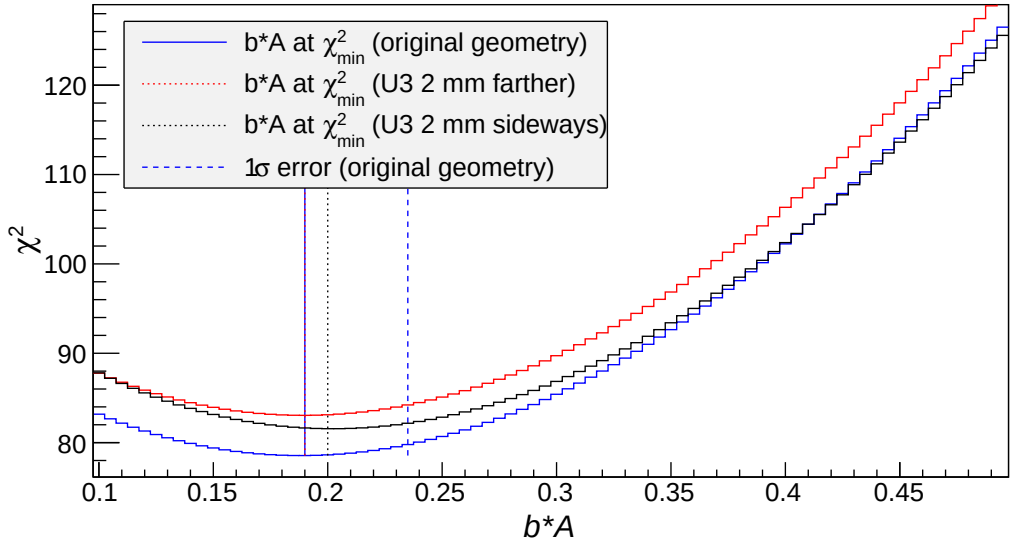

Fig. 5.22 The figure shows three different χ^2 versus a^*A plots (for the ^{12}C excitation energy region 10 - 10.5 MeV). The blue line corresponds to the analysis with detector positions as obtained in section 5.2, and listed in table 4.1. The red line was made with the U3 detector's position moved 2 mm farther, while the black one was made with the U3 detector's position moved 2 mm sideways upstream. The variation in the x-axis value of the χ^2 minima is small enough to be overshadowed by the statistical uncertainties in the results.

Chapter 6

Results and Discussion

6.1 Strength profile of the second 2^+ resonance

To quickly revisit what has already been explained in chapter 3 and chapter 5, here is a summary of how the anisotropy in the β-α angular correlation in the cascade $^{12}\mathrm{N}(\beta^+)^{12}\mathrm{C}(\alpha_1)^8\mathrm{Be}(\alpha_2)\alpha_3$ has been used to extract the 2^+ resonance strength profile in the ^{12}C nucleus. The β-α angular correlation function for a 0^+ state should be isotropic,

$$W(\theta)_{0^+} = 1 \tag{6.1}$$

Whereas, for a 2^+ state, this function has the behaviour,

$$W(\theta)_{2^+} = 1 + A \times P_2(cos\theta) \tag{6.2}$$

where, A is a constant dependent on β-decay and α-decay matrix elements, and $P_2(\cos\theta)$ is the second order Legendre polynomial. Assuming that the fraction of the 2^+ strength in the ith energy bin is b_i, the total angular correlation for that energy region should be,

$$W(\theta)_i = [(1 - b_i) \times W(\theta)_{0^+}] + [b_i \times W(\theta)_{2^+}] = 1 + b_i \times A \times P_2(cos\theta) \tag{6.3}$$

It becomes clear from equation 6.3 that the measured anisotropy in the angular correlation for an energy region should be equal to b_i*A, and therefore is directly proportional the fraction of 2^+ resonance strength (b_i) in the region. Therefore, by measuring the anisotropy in β-α angular correlations for 500 keV wide energy bins in the excitation energy region of interest (8.5 - 12 MeV), the 2^+ resonance strength profile has been extracted.

The procedure for measuring the anisotropy in the β-α angular correlations has been explained in detail in section 5.7. Following that procedure, the χ^2 minimisation routine was performed for all six energy regions in the 9 -12 MeV excitation energy range. The χ^2 versus the product b_i*A for each energy region is shown in figure 6.1. The b_i*A value corresponding to the χ^2_{min} is highlighted by a solid red line in these plots. The dashed red line is highlighting the b_i*A value corresponding to the (χ^2_{min} + 1). The difference between those two values, b_i*A (χ^2_{min}) - b_i*A (χ^2_{min} + 1), gives the 1σ error on the b_i*A (χ^2_{min}) value [63]. The extracted b_i*A values along with the 1σ error have been given in table 6.1.

Figure 6.2 and 6.3 show the comparison of experimental data to the simulations. In figure 6.2, experimental data angular correlations (solid blue line) have been compared with theoretical 0^+ (dotted red line) and 2^+ (dotted black line) angular correlations. The theoretical curve for the angular correlation of the 0^+ state were obtained by simulating isotropic β-decay followed by isotropic emission of the α_1-particle in the triple-α breakup. To obtain the theoretical curve for the 2^+ state, the isotropic curve was scaled to the theoretical angular correlation function, $W(\theta)_{2^+}$.

All six values of b_i*A in table 6.1 together provided the information as to how the fraction of the 2^+ strength varies across the excitation energy region of 9 - 12 MeV. By combining those values with the experimental data (which has been corrected for detection efficiency) in each energy bin, the final 2^+ resonance strength profile was extracted. These steps have been shown in figure 6.4. In the top panel, the blue line shows the detected β-triple-α coincidence data in the 9 - 12 MeV excitation energy range, gated on the ^{8}Be ground state breakup channel. This data was then corrected

bin no., i	^{12}C ex. energy (MeV)	Best fit b_i*A	1σ error
1	9.0 - 9.5	0.100	0.065
2	9.5 - 10.0	0.165	0.050
3	10.0 - 10.5	0.190	0.045
4	10.5 - 11.0	0.265	0.055
5	11.0 - 11.5	0.425	0.100
6	11.5 - 12.0	0.100	0.165

Table 6.1 The table lists the b_i*A values corresponding to the minimum χ^2 value for each of the six 500 keV wide energy regions between 9 - 12 MeV excitation energy.

for the detection efficiency that varied as a function of energy as shown in previous chapter in figure 5.14. The efficiency corrected data has been shown in the same figure for comparison as a red line. In the middle panel in figure 6.4, the b_i*A values (table 6.1) have been plotted as a function of the excitation energy. The bottom panel shows the 2^+ resonance strength profile, which is obtained by multiplying the values in the middle panel and the efficiency corrected values in the top panel (the red line curve).

6.2 Angular correlation of the 12.7 MeV 1^+ state

As a last test to ensure that the observed anisotropy was not an artefact of some unknown energy-dependent effect in the analysis, the β-α angular correlation of the 12.7 MeV 1^+ state was analysed. For this analysis, data was gated on the breakup channel via the excited state of ^{8}Be. The angular correlation for the 12.7 MeV 1^1 state is expected to be isotropic. Therefore, the anisotropy parameter, A_2, in the fitting function $W(\theta) = 1 + A_2 \times P_2(cos\theta)$, was expected to be zero.

A similar χ^2-minimisation routine as before was implemented to evaluate the best-fit value for the A_2 parameter. The χ^2 value as a function of the A_2 parameter has been shown in figure 6.5, in the top panel. In the bottom panel, the experimental data angular correlation plot (solid blue line) has been compared with the best-fit simulated angular correlation plot (dashed green line). It is clear from this fitting

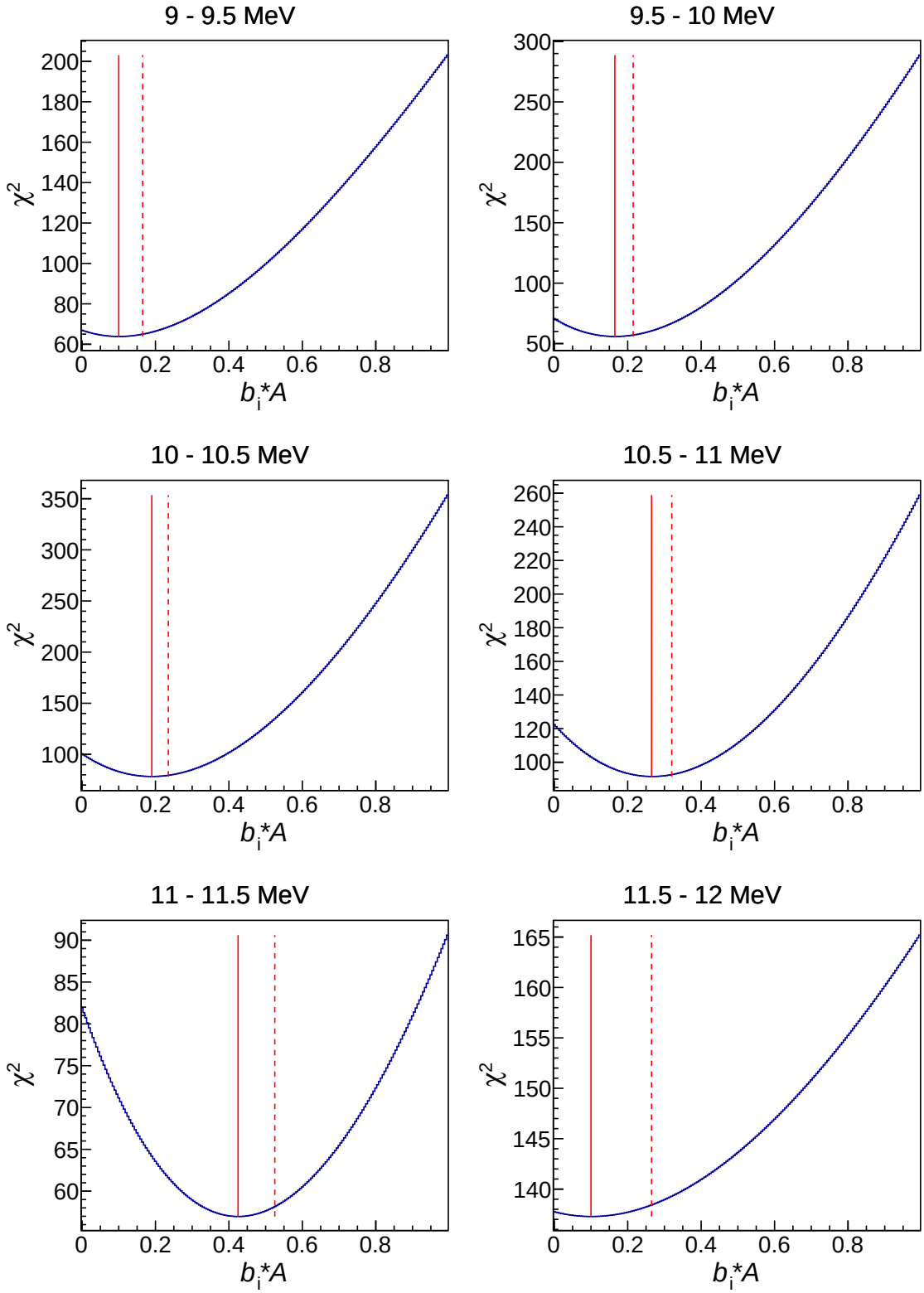

Fig. 6.1 The figure shows the χ^2 values as a function of the product $b_i{*}A$, where b_i and A are the parameters used in the fitting function. The solid red line corresponds to the best fit $b_i{*}A$ value. The difference between the solid red line and the dotted red line is equal to the 1σ error on the best fit $b_i{*}A$ value respectively.

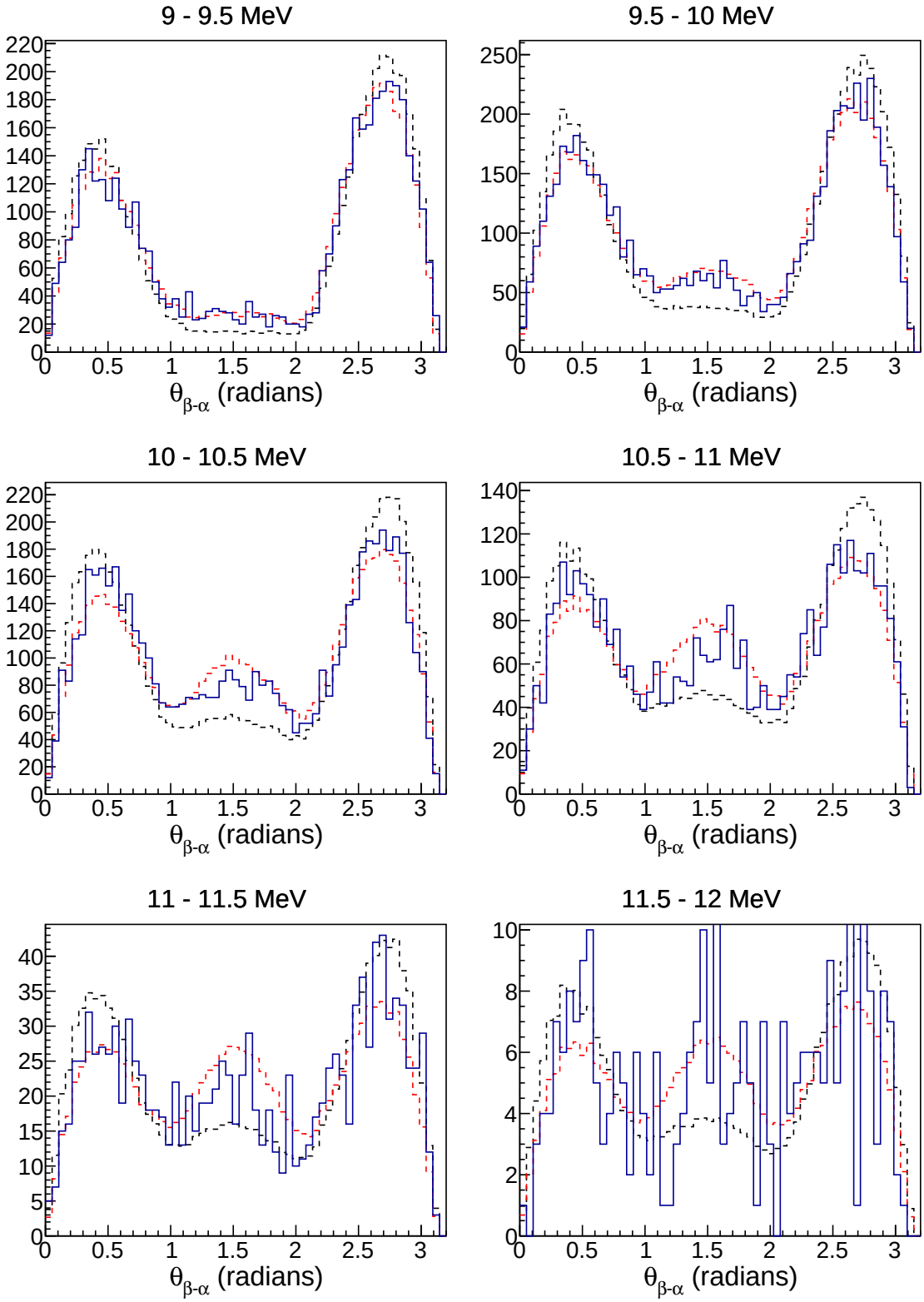

Fig. 6.2 The figure shows β-α angular correlation plots of experimental data displayed as the solid blue line and the simulated histograms for pure 0^+ and 2^+ states displayed as the dotted red and black lines respectively.

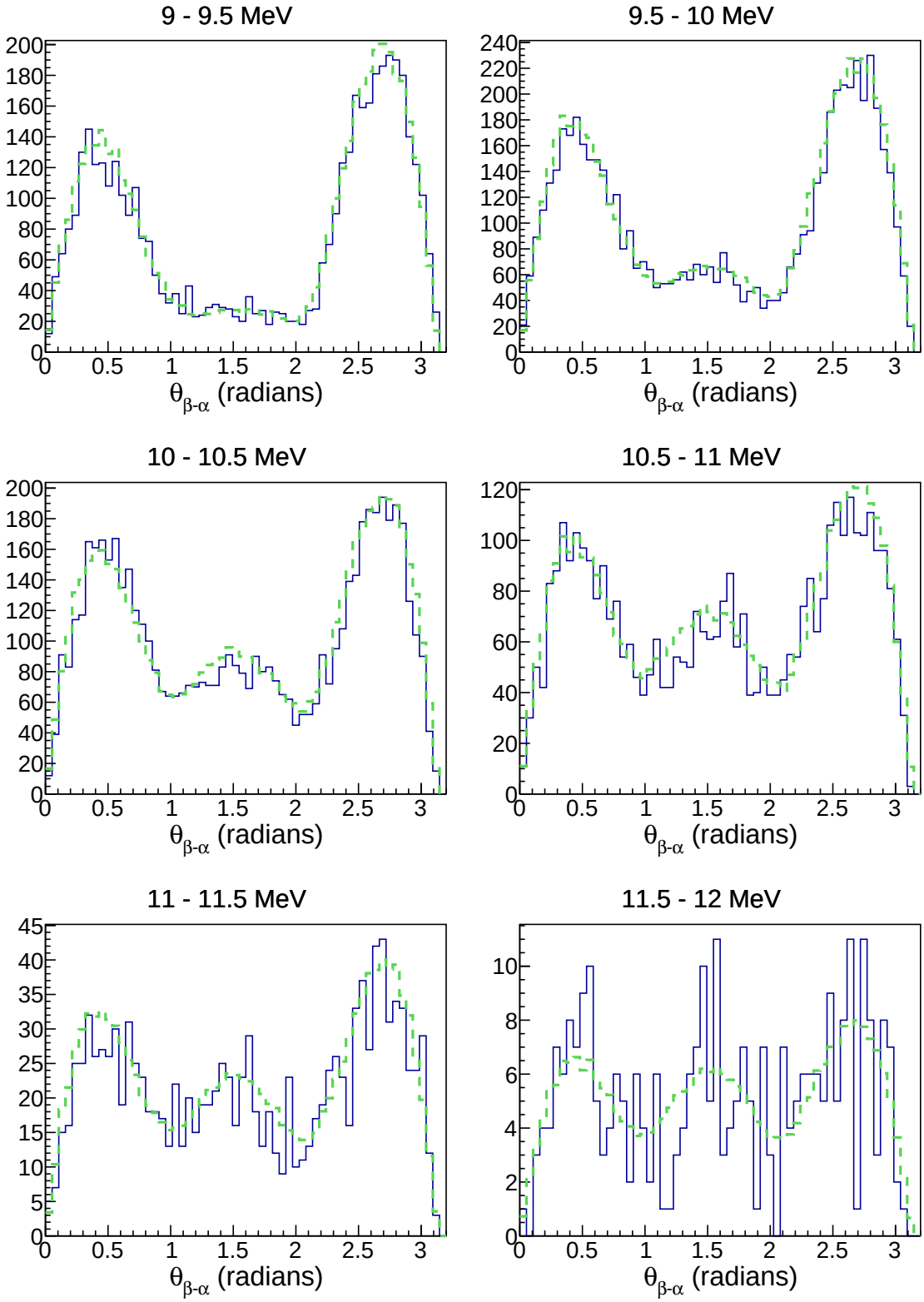

Fig. 6.3 The figure shows the experimental data β-α angular correlation histogram displayed as the solid blue line, along with the fit obtained by combining the simulated 0^+ and 2^+ histograms displayed as the dotted green line.

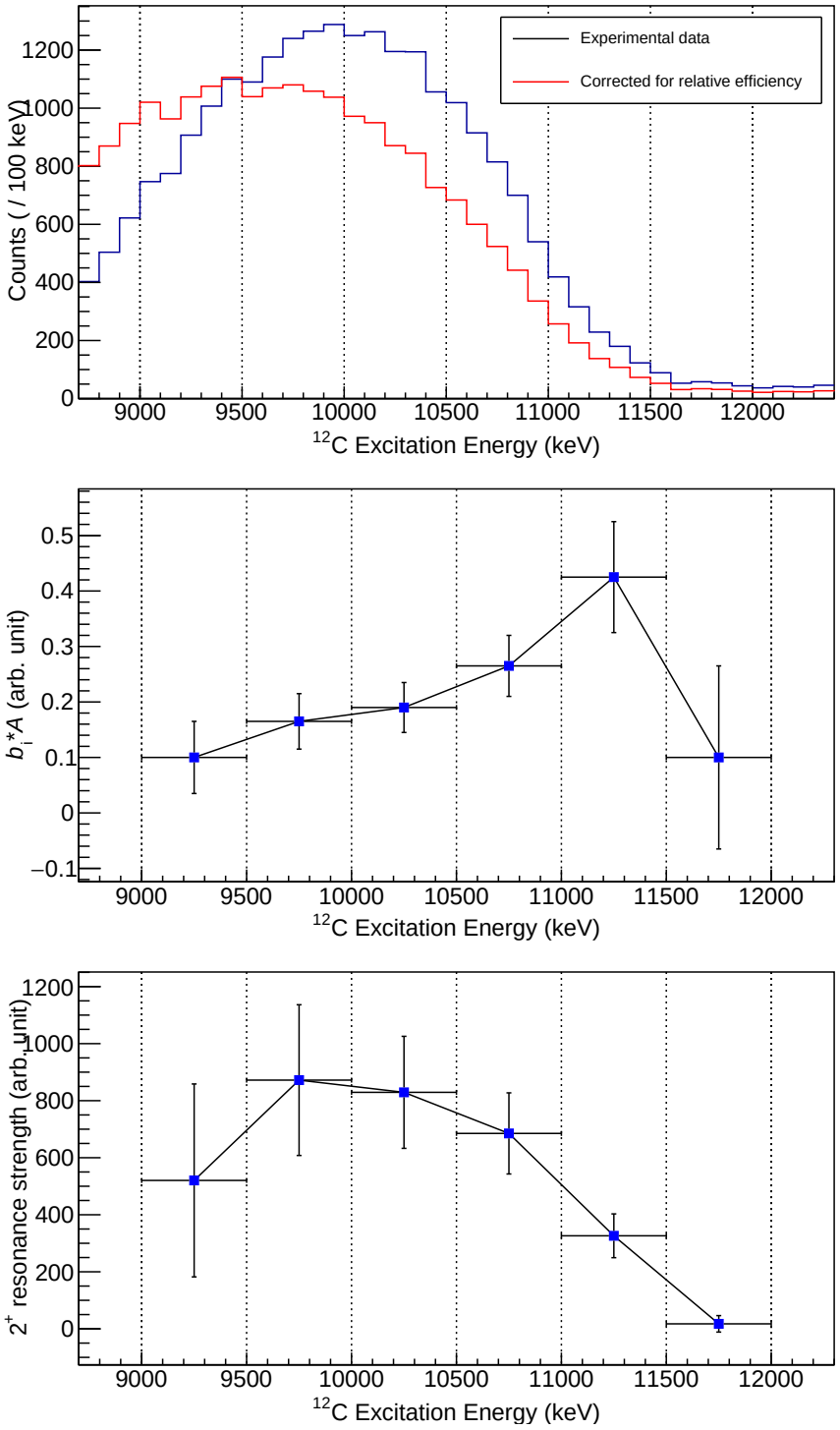

Fig. 6.4 The top panel shows the detected β-triple-α coincidence data for the 9 - 12 MeV excitation energy region as the blue line. The red line shows the detection efficiency corrected data. The middle panel shows the b_i*A values, that were obtained via the χ^2-minimisation, plotted against energy. The bottom panel shows the final result for the 2^+ resonance strength that is extracted by combining the values of b_i*A with the efficiency corrected data.

that the A_2 value is consistent with the expected value of zero to within a 1σ error. This result along with the observed small value of $b_i{*}A$ for the 9 - 9.5 MeV region where the 0^+ component is expected to dominate, rules out the possibility that some systematic error in the analysis could be the cause of observed anisotropy near the 10 MeV excitation energy.

One other thing to note in the angular correlation plot of the 1^+ state is that the relative size of the dips to the bumps is smaller compared to those in the angular correlation plots for the 9 - 12 MeV excitation energy region. The reason for that is, the breakup dynamics of the 1^+ state is very different from that of the 0^+ or the 2^+ state. The three α-particles from the breakup of the 1^+ state are emitted in all different directions, unlike in the breakup of 0^+ or 2^+ state, where the direction of emission of α_2 and α_3 is almost directly opposite the direction of emission of α_1. Therefore, the geometrical acceptance for the triple-α coincidence detection is different for the two different breakup channels. If the α_1-particle from the breakup is emitted toward the edge of one detector, the chances of the coincident detection of α_2 and α_3 would be higher in the breakup of the 1^+ state than the breakup of a 0^+ or 2^+ state.

6.3 R-matrix fitting

In the previous section, the final experimental result on the observation of the 2^+ resonance strength was presented in figure 6.4. In order to extract the resonance energy and width from those data, *R*-matrix calculations were performed using the code AZURE2. In this section, the *R*-matrix calculation results are presented and discussed. The details of both, the *R*-matrix formalism, and the AZURE2 code have already been discussed in chapter 3, section 3.3.

The incoming channel is defined in AZURE2 by the particle pair (^{12}N, β^+), with the particle spins (1^+, $1/2^+$). The separation energy is taken as the β-decay Q-value, 16.316 MeV, calculated using, $Q_\beta = (M_{^{12}N} - M_{^{12}C} - 2m_e)c^2$. The channel radius

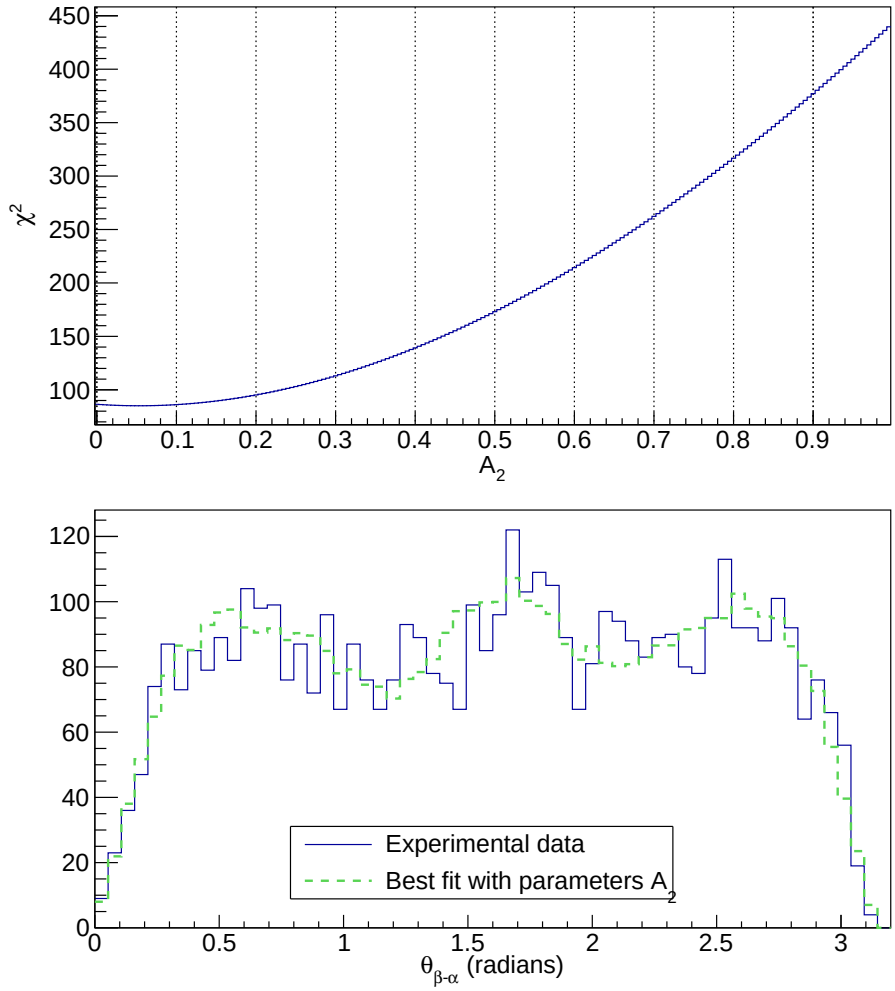

Fig. 6.5 The figure shows the β-α angular correlation fitting for the 12.7 MeV 1^+ state. The top panel shows the χ^2 versus the parameter A_2 of the fitting function. The bottom panel shows the experimental data compared to the best-fit with the A_2 value obtained from the plot above.

was calculated as,

$$a_c = r_0(A_1^{1/3} + A_2^{1/3}) \tag{6.4}$$

where, A_1 and A_2 are the mass numbers of the two particles in the pair, and r_0 is chosen arbitrarily large enough to exclude any nuclear interaction in the external region. Here, r_0 was taken as 1.4 fm. This value of r_0 is what is typically observed from the electron-scattering experiments [50]. This gave the value of channel radius, a_c, for the incoming channel as 3.205 fm.

The exit channel particle pair was (^{8}Be, α), with the particle spins (0^+, 0^+). The separation energy was taken as the α-threshold in the ^{12}C nucleus, 7.367 MeV [33].

In the case of the (^{8}Be, α) particle pair, the channel radius, a_c, was calculated to be 5.022 fm, with the r_0 = 1.4 fm. But since the Hoyle state has an extended spatial-distribution, the r_0 value had to be taken larger in order to get the calculations to work without crashing. The process of deciding the optimal value of a_c has been described in detail in subsection 6.2.3. The value of a_c was set to be 9.5 fm.

6.3.1 2^+ resonance strength fitting

There were only six data points that could be used for the *R*-matrix fitting to obtain the 2^+ resonance energy and width. Therefore, only single level calculations could be performed. In practise, more levels at higher energies could have been included, but the number of free parameters for two levels would have been 6. The number of free parameters per level is 3: resonance energy, reduced width, and β-decay strength. Using six free parameters, six data points can be fit perfectly with a reduced χ^2 of 1. But the uncertainty on the parameters obtained would be infinite.

The results of the single level fit have been given in table 6.2 and the fit and the data have been shown in figure 6.6. The errors on the energy and width were obtained by performing the MINOS error analysis option in AZURE. The MINOS error analysis provides the asymmetric errors, but the higher of the two values have been shown in the table 6.2. The shape of the resonance can be explained via the β-decay phase space factor. Compared to the reaction probes in the works [25, 36], the observed short tail in present work is due to the fact that the β-decay phase space cuts close to the Q-value.

E_R (MeV)	Γ_R (MeV)	χ^2/N
10.53 (0.165)	1.35 (0.25)	1.44

Table 6.2 *R*-matrix fit results for the 2^+ resonance.

It should be noted that the exit channel where the breakup proceeds via the excited 2^+ state of ^{8}Be has not been included in these calculations. Additionally, the interference from higher lying 2^+ resonances could not be studied here due to limited

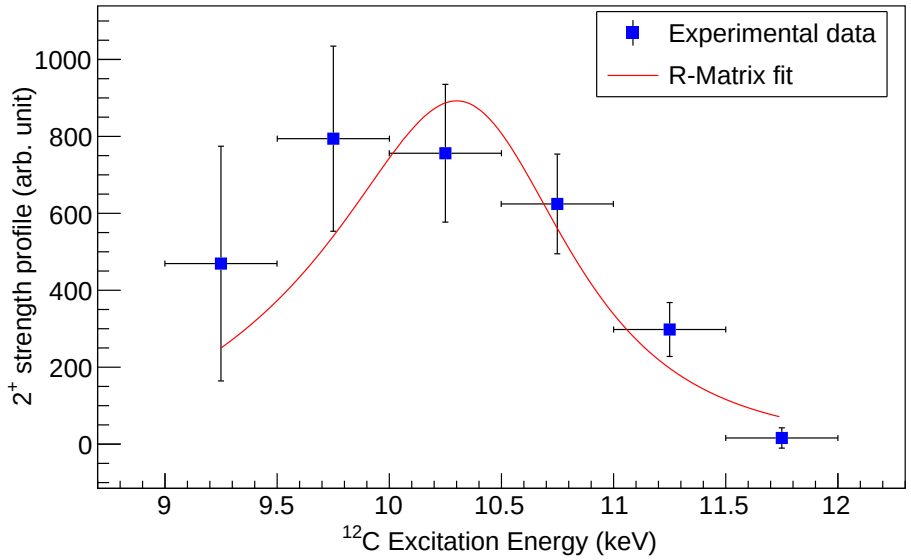

Fig. 6.6 The figure shows the experimentally extracted 2^+ resonance strength along with the R-matrix fit to the data.

statistics. These factors might have an effect on the resonance parameters. This has been discussed in the next chapter under considerations for future work.

6.3.2 Triple-α data fitting

The triple-α coincidence data, first corrected for the detection efficiency, was used for fitting the R-matrix parameters using several different combinations of levels for calculations. The different levels that were used in the calculations and the initial guess on their energies and widths have been listed in table 6.3.

Level	Description	Initial guess parameters	
		E_R (MeV)	Γ_R (keV)
$_{HS}0^+$	The Hoyle state	7.654	0.0085
$_1 0^+$	An identified state in [17]	10.3	3000
$_2 0^+$	An arbitrary, high energy, broad state	15.0	10000
$_1 2^+$	The state from the fit in fig 6.6	10.53	1348
$_2 2^+$	An arbitrary, high energy, broad state	15.0	10000

Table 6.3 The table lists the levels that were used in fitting the triple-α data.

In order to perform the analysis in a systematic way, first the calculations were performed with only the Hoyle state and other levels were added to the fits progressively. All the different level combinations along with the reduced χ^2 values of the fit have been listed in table 6.4.

Fit no.	Levels	χ^2/N
1	${}_{HS}0^+_f$	992.00
2	${}_{HS}0^+_f + {}_1 0^+$	20.23
3	${}_{HS}0^+_f + {}_1 0^+ + {}_2 0^+$	1.05
4	${}_{HS}0^+_f + {}_1 0^+ + {}_1 2^+_f$	16.22
5	${}_{HS}0^+_f + {}_1 0^+ + {}_2 0^+ + {}_1 2^+_f$	1.04
6	${}_{HS}0^+_f + {}_1 0^+ + {}_2 0^+ + {}_1 2^+$	0.85
7	${}_{HS}0^+_f + {}_1 0^+ + {}_1 2^+ + {}_2 2^+$	1.10

Table 6.4 The table lists the different fits that were performed on the triple-α data. The first row is the fit number, the second row is the combination of levels that were used in the fit, and the third row shows the reduced χ^2 values. The f subscript implies that the physical parameters for the state were fixed at the initial guess value.

Fit 1: As was mentioned above, the first fit was performed using just the Hoyle state, and the χ^2 value proved that it was a bad fit. But this was as expected as there is at least one other identified 0^+ state in the energy region. The fit results have been shown in table 6.5 and figure 6.7.

Level	E_R (MeV)	Γ_R (keV)
${}_{HS}0^+_f$	7.654	0.0085

Table 6.5 R-matrix fit-1 output parameters

Fit 2: This fit was performed with two 0^+ states: the Hoyle state and the known $\sim$10 MeV 0^+ resonance. The χ^2 value for *fit 2* was an improvement over *fit 1*, but it was still not a good fit with χ^2/N = 20.23, indicating the presence of more states in the region. The fit results have been shown in table 6.6 and figure 6.8.

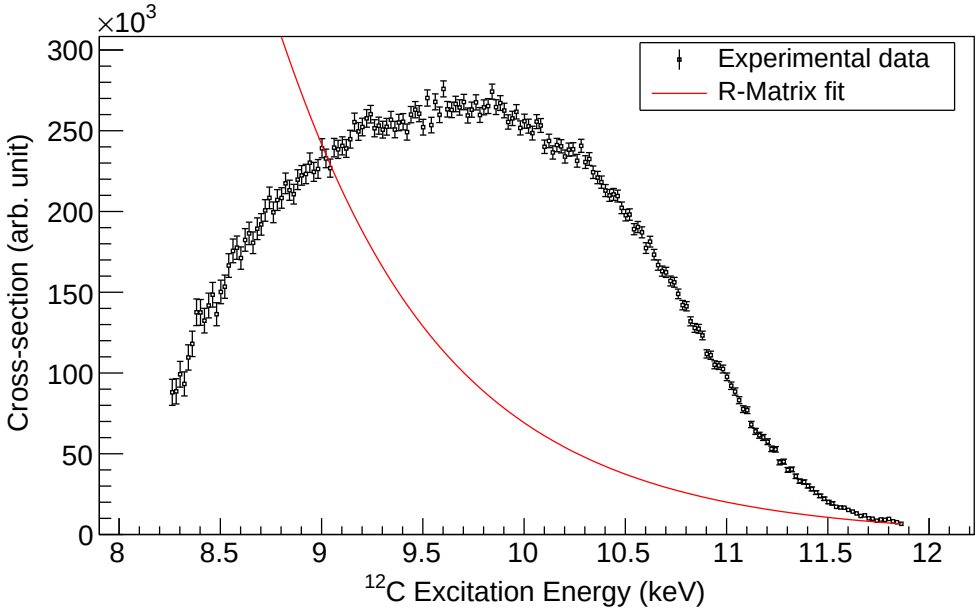

Fig. 6.7 R-matrix fit-1.

Level	E_R (MeV)	Γ_R (keV)
${}_{HS}0^+_f$	7.654	0.0085
${}_{1}0^+$	10.644	1721.9

Table 6.6 R-matrix fit-2 output parameters

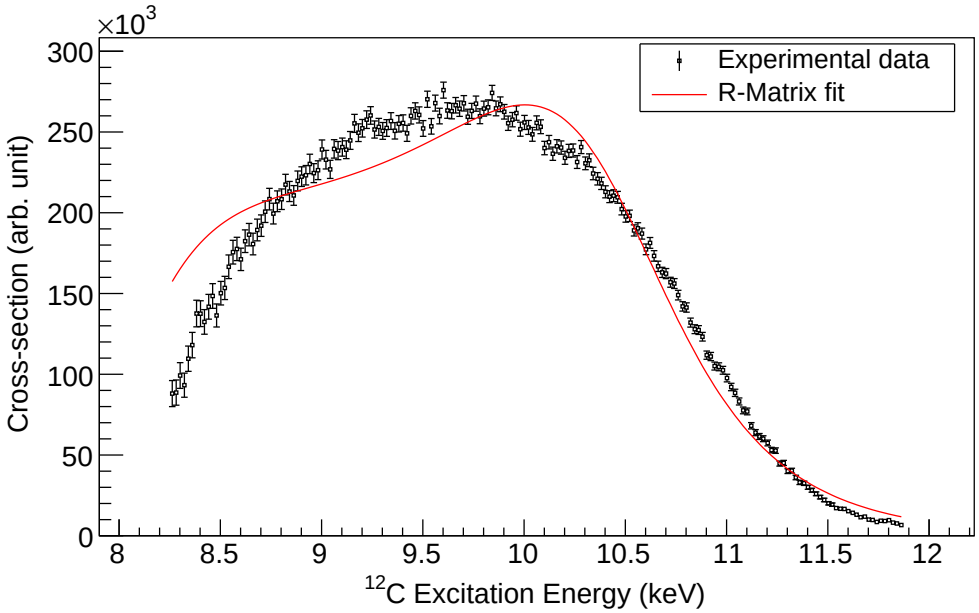

Fig. 6.8 R-matrix fit-2.

Fit 3: The calculations were performed with three 0^+ states this time, with the third 0^+ being a broad background state lying at high energy. The resulting χ^2/N value

of 1.05 indicated it to be a good fit. The fit results have been shown in table 6.7 and figure 6.9.

Level	E_R (MeV)	Γ_R (keV)
${}_{HS}0^+_f$	7.654	0.0085
${}_{1}0^+$	10.028	1747.3
${}_{2}0^+$	13.612	8125.1

Table 6.7 *R*-matrix fit-3 output parameters

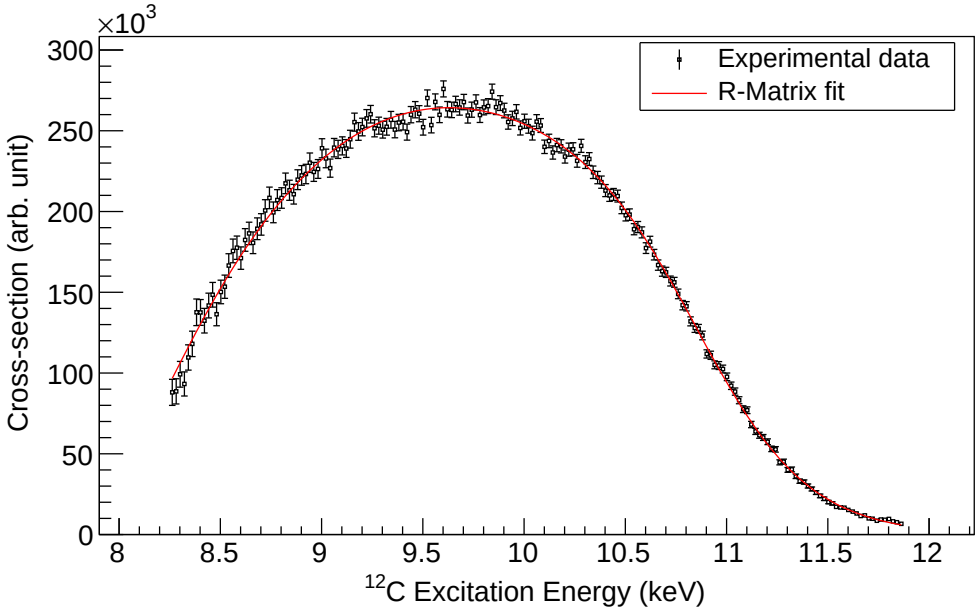

Fig. 6.9 *R*-matrix fit-3.

Fit 4: This fit also was performed with three levels: the Hoyle state, the ∼10 0- 0^+ state, and the observed 2^+ state instead of the broad background 0^+ state. This fit had a large χ^2/N value of 16.22 proving the requirement of the broad background state. The fit results have been shown in table 6.8 and figure 6.10.

Fit 5 (the best fit): This fit was performed with four states: three 0^+'s, same as the *fit 3* with the addition of the observed 2^+. The energy and the width of the 2^+ state were kept fixed in the calculations. This fit gave the best χ^2/N value of 1.04. The fit results have been shown in table 6.9 and figure 6.11.

The addition of the fixed energy and width 2^+ state added one extra degree of freedom (the β decay strength) to the *fit 5* as compared to *fit 3*. Therefore, an

Level	E_R (MeV)	Γ_R (keV)
${}_{HS}0^+_f$	7.654	0.0085
${}_{1}0^+$	9.933	1572.0
${}_{1}2^+_f$	10.530	1348.0

Table 6.8 R-matrix fit-4 output parameters

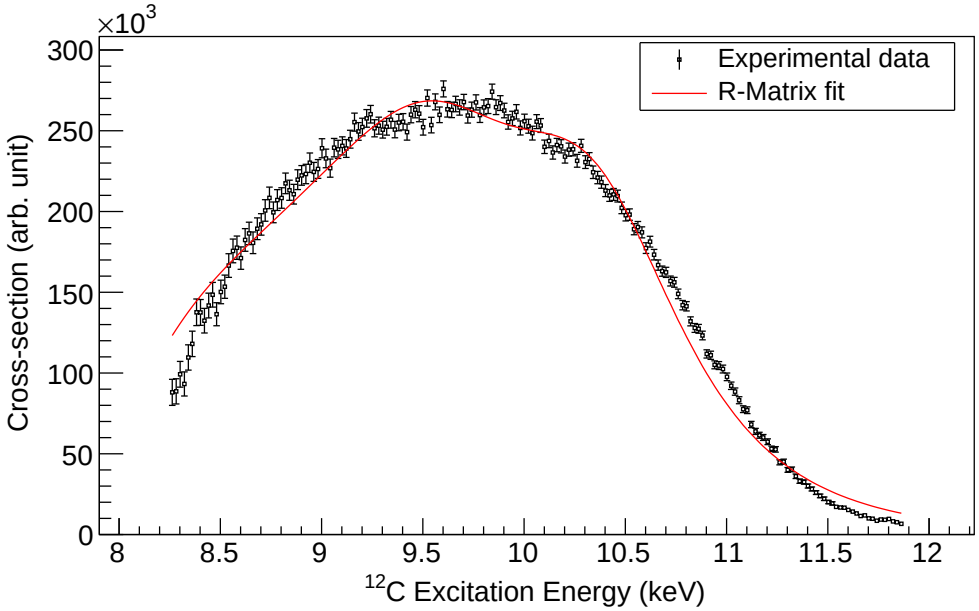

Fig. 6.10 R-matrix fit-4.

improvement of 0.006 in χ^2/N value was expected. But it should be noted that however the χ^2/N improvement between *fit 3* and *fit 5* was more than expected (0.008 as compared to ∼0.006), it is not a substantially large difference. That is to say that for the extraction of the 2^+ state's parameters, the result from the β-α angular correlation work are more reliable.

Level	E_R (MeV)	Γ_R (keV)
${}_{HS}0^+_f$	7.654	0.0085
${}_{1}0^+$	9.972	1751.2
${}_{2}0^+$	12.866	5600.2
${}_{1}2^+_f$	10.530	1348.0

Table 6.9 R-matrix fit-5 output parameters

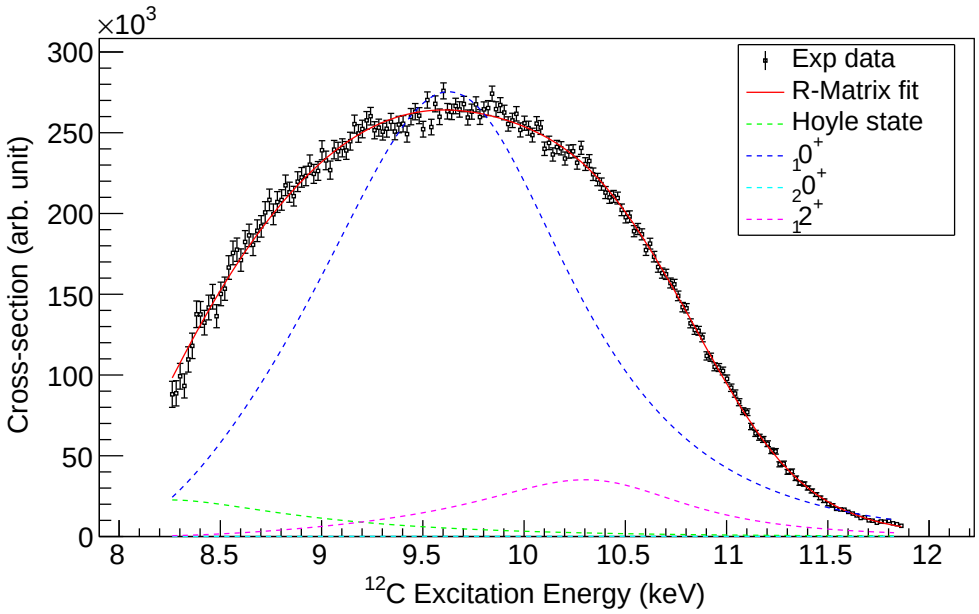

Fig. 6.11 *R*-matrix fit-5 (the best fit): The figure shows detection efficiency corrected triple-α data along with the *R*-matrix fit (solid red line) with four levels: the Hoyle state (dashed green line), the ∼10 MeV 0^+ state (dashed blue line), a broad background 0^+ state (dashed purple line, but hardly visible due to the scale), and the 2^+ state (dashed cyan line). The χ^2/N value for this fit was 1.04.

Fit 6: An attempt was made to perform the calculation with the same levels as *fit 5* but leaving the 2^+ state's parameters free. The χ^2/N value for this fitting was 0.85. But the output parameters were unrealistic with the broad background 0^+ state at 55 MeV and the B value (β-decay *R*-matrix fit parameter that relates to the branching ratio [64]) of 94. The fit has been shown in figure 6.12.

Level	E_R (MeV)	Γ_R (keV)
$_{HS}0^+_f$	7.654	0.0085
$_1 0^+$	11.133	2027.1
$_2 0^+$	55.699	16137.1
$_1 2^+$	11.821	187.6

Table 6.10 *R*-matrix fit-6 output parameters

Fit 7: The last fit was performed with two 0^+ states and two 2^+ states. The new addition in this fit was the second 2^+ state that was the broad background state lying at high energy. The χ^2/N value of this fit was 1.06. The fit results have been shown in table 6.11 and figure 6.13.

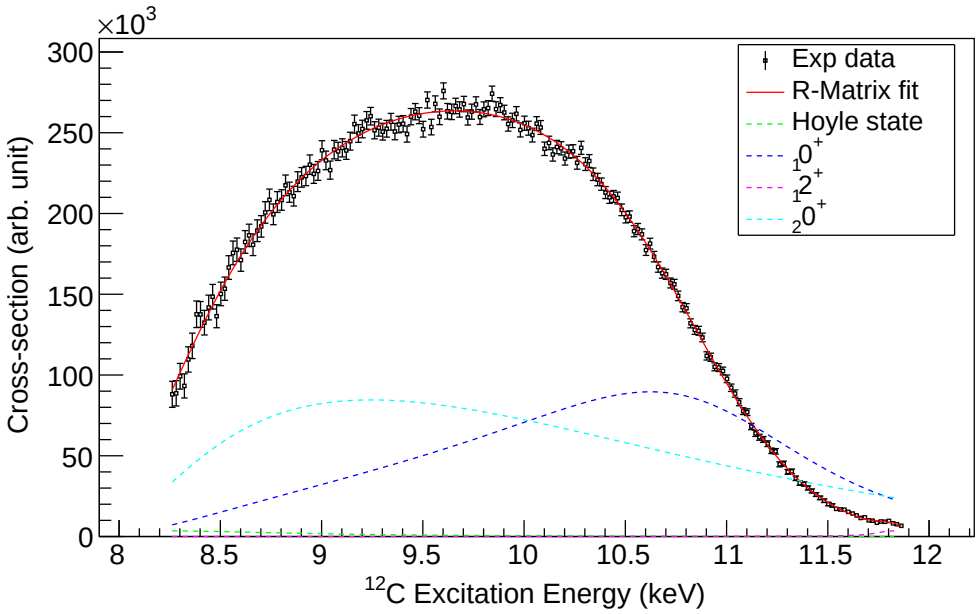

Fig. 6.12 *R*-matrix fit-6.

The comparison between *fit 5*, *fit 6*, and *fit 7* has been made in the conclusions chapter in section 7.2.

Level	E_R (MeV)	Γ_R (keV)
$_{HS}0^+_f$	7.654	0.0085
$_1 0^+$	10.431	3175.7
$_1 2^+_f$	10.530	1348.0
$_2 2^+$	12.604	2351.8

Table 6.11 *R*-matrix fit-7 output parameters

6.3.3 The exit channel radius

The channel radius is not a physical parameter, but an auxiliary parameter of the *R*-matrix theory. The value for the channel radius can be chosen arbitrarily so long as it is chosen large enough that there is no strong interaction in the external region. As was mentioned in the beginning of section 6.2, the physical estimate of the channel radius can be usually calculated using the values of r_o that are obtained from the electron scattering experiments, in equation 6.4. But in the presented work, the outgoing channels involve the resonances that have cluster structure. The spatial

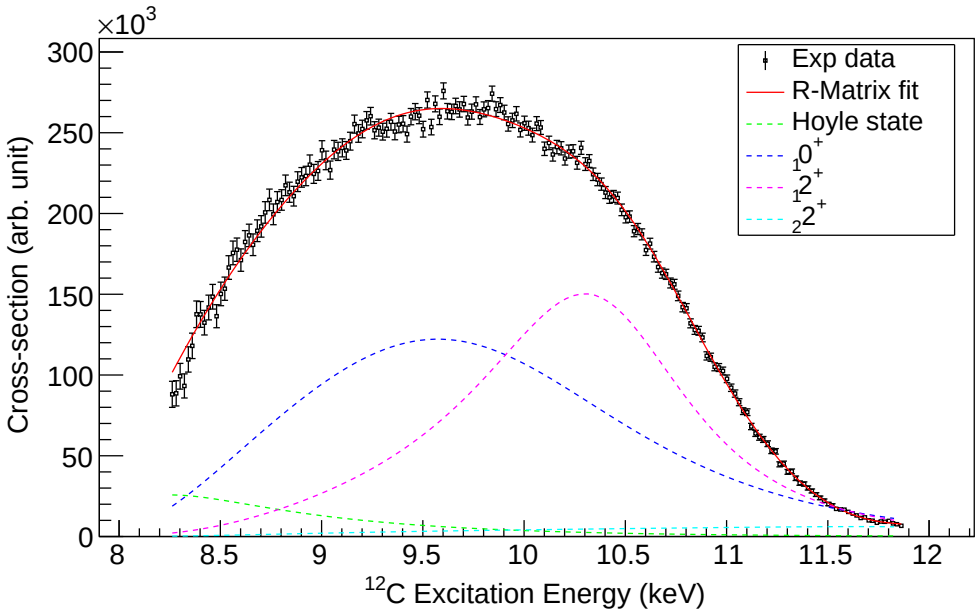

Fig. 6.13 *R*-matrix fit-7: the total fit (solid red line) consisted of four levels: the Hoyle state (dashed green line), the ∼10 MeV 0^+ state (dashed blue line), the 2^+ state (dashed pink line), and a broad background 2^+ state (dashed cyan line).

distribution of a cluster state is usually large and therefore, the value of r_o as 1.4 fm does not give a good physical estimate of the channel radius value. Therefore, it was necessary to investigate the effect of the channel radius on the fit results.

To study the effect of the varying channel radius on the fit outputs, the *fit 5* fits were performed with the various a_c values between 5.5 - 10.0 fm (r_o = 1.53 - 2.78 fm). The output results (resonance energies and widths) from the fits with channel radii smaller than 9.0 fm were physically unrealistic for the broad background states. For example, the energy for 0_1^+ converged to the values -2146 MeV and 3067 GeV for a_c of 6 fm and 8.5 fm respectively. The resonance width for 0_1^+ was not returned for the a_c = 6 fm calculations. For the fit with a_c = 8.5 fm, the resonance width for 0_1^+ state converged to value 3.4 × 10^{14} keV. Therefore those fits have not been discussed any further. The resonance energy and width outputs from fits with a_c = 9.1, 9.5, 10.0 fm have been shown as functions of channel radius in figure 6.14 and 6.15 respectively. It can be seen from these figures that the effect of varying the channel radius on the resonance parameters is of the order of a few percent. Between a_c=9.1 fm and a_c=10.0 fm, the resonance energy varies by less than 1% and the resonance width varies by approximately 5%. In order to select an optimum value,

the trend from the figures was used as a guide and the middle value of 9.5 fm (r_o = 2.64 fm) was chosen. In the work by Hyldegaard *et* al. [30], the r_o values was taken as 2.47 fm for the fit shown in figure 2.2 in section 2.1. This r_o value of 2.47 fm corresponds to the channel radius value (a_c) of 8.9 fm, which is very close to the region that has been region that has been assessed to be optimum in the present work.

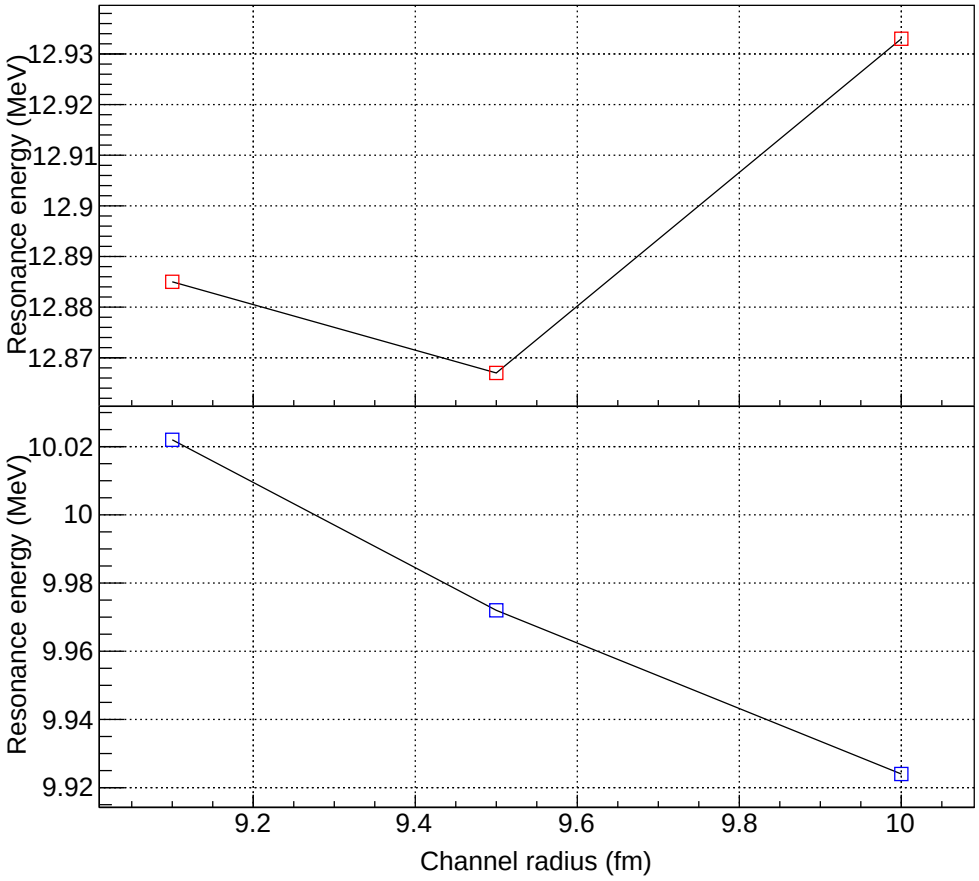

Fig. 6.14 The resonance energy versus channel radii for the broad background 0^+ state (top) and the ∼10 MeV 0^+ state (bottom).

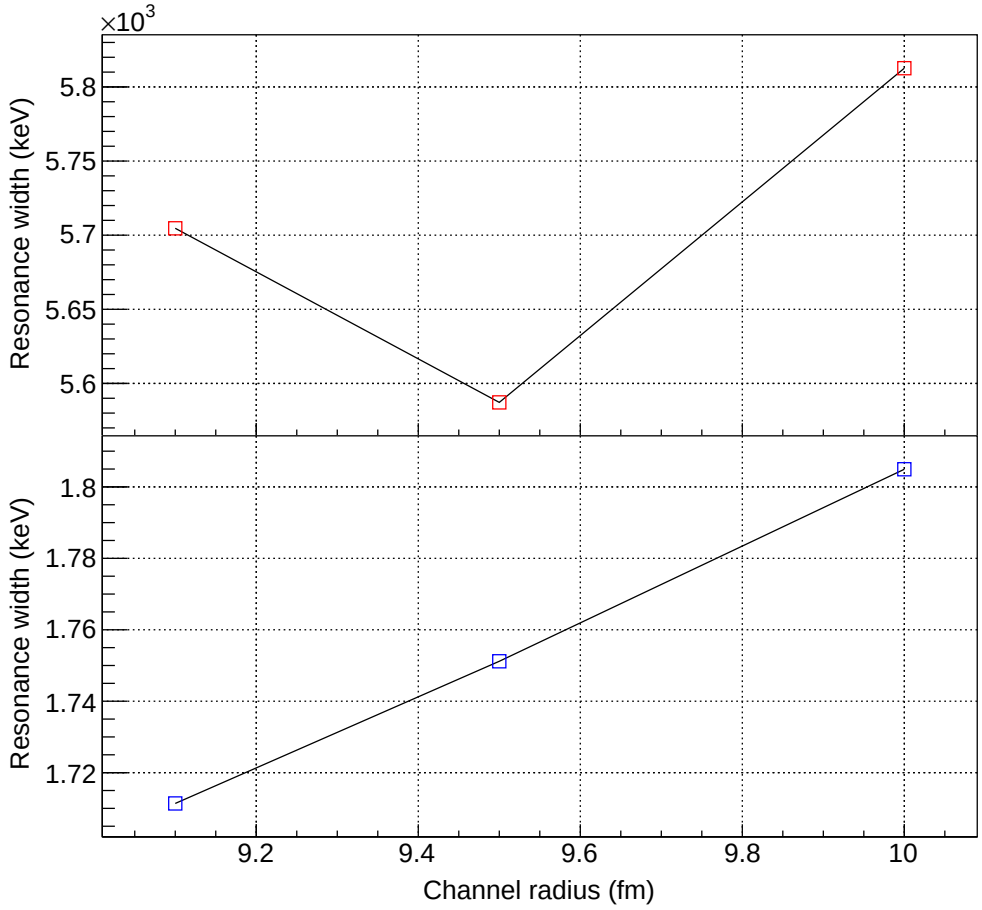

Fig. 6.15 The resonance width as the function of channel radii for the broad background 0^+ state (top) and the ∼10 MeV 0^+ state (bottom).

Chapter 7

Conclusion and Future Work

7.1 A novel identification of the ^{12}C 2_2^+ state

The objective of the present work was to search for the 2_2^+ state of the ^{12}C nucleus in the 9 – 11 MeV excitation energy region. Such a state is predicted by theoretical models as the first rotational excitation of the Hoyle state. While there have been claims of the observation of this state in different works, an agreement on the observed resonance parameters has not been reached between results from different probes. Previous studies with the β-decay of ^{12}N and ^{12}B recommended the ^{12}C 2_2^+ state's energy and width at 11.1 $\pm$ 0.3 MeV and 1.4 $\pm$ 0.4 MeV, while the inelastic scattering experiments suggest these parameters' values as 9.75 $\pm$ 0.15 MeV and 750 $\pm$ 150 keV respectively. In the γ-excitation experiment this state was measured at 10.03 $\pm$ 0.11 MeV[1] with the width of 800 $\pm$ 130 keV. In the present work we have studied the resonance using the novel technique of the β-triple-α angular correlation to extract the 2^+ strength in the ^{12}N β-decay experiment. We present, for the first time in a β-decay study, a clear identification of the ^{12}C 2_2^+ state in the experimental data in the present work.

7.2 Resonance parameters for the 2^+ state

The recommended values for the resonance energy and width that are obtained from R-matrix fitting to the 2^+ strength extracted from β-α angular correlation analysis are 10.53 $\pm$ 0.17 MeV and 1.35 $\pm$ 0.25 MeV respectively. It should be noted

[1]The data analysing is being revisited and the new value for resonance might be smaller [37]

that the R-matrix fitting to the 2^+ strength was somewhat limited by the statistics (figure 7.1a). There are potentially three free parameters per state in the R-matrix fitting. Therefore, with only six data points available, the interference effects from the other higher lying 2^+ states could not be studied. Also, due to the low statistics, the breakup channel via the ^{8}Be excited state has not been analysed for the 2^+ strength using β-α angular correlation.

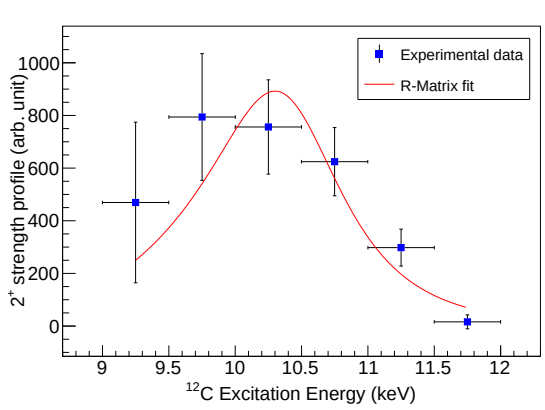

(a) 2^+ strength in β-3α angular correlations

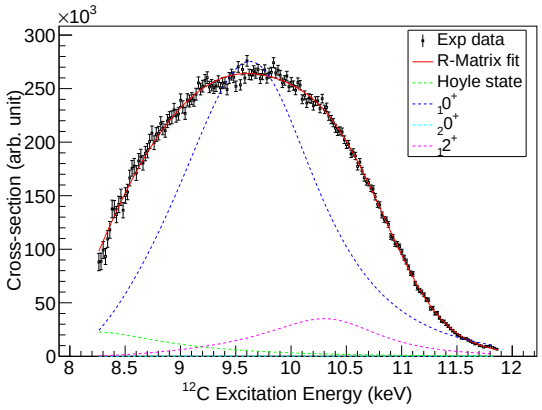

(b) 3α data, *fit* 5.

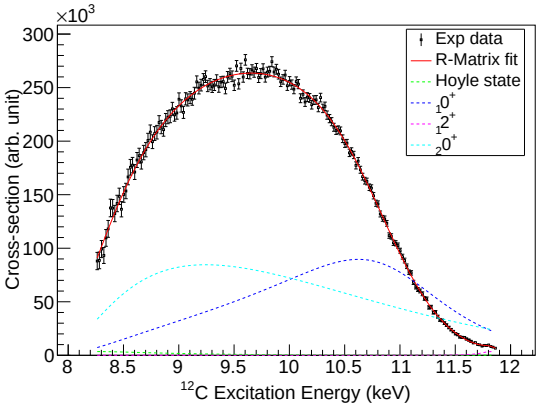

(c) 3α data, *fit* 6.

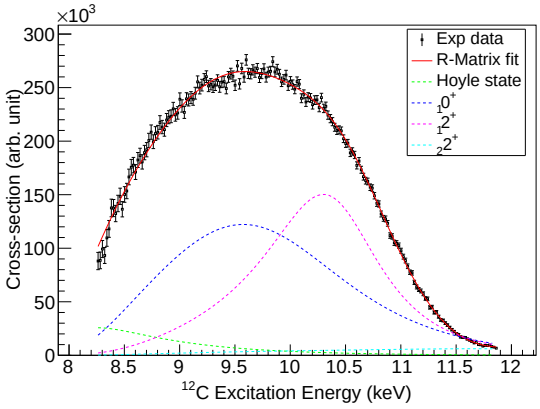

(d) 3α data, *fit* 7.

Fig. 7.1 Main R-matrix fits discussed in conclusion. Plots shown here are same as those shown in section 6.3.1 and section 6.3.2.

The triple-α data has similarly been analysed through R-matrix fitting. Fit 6 (figure 7.1c) in section 6.3.2 was performed with fixed parameters for the Hoyle state and free parameters for the 10 MeV 0^+ strength and the 2^+ state. Another broad higher lying 0^+ state was included in this fit for the 0^+ background. The resonance parameters for the 2^+ state obtained from this fit suggested the energy and width of 11.8 MeV and 187 keV respectively. This is very different from the

results obtained from the β-α angular correlation data. Hence, it can be inferred that a conclusion on the 2^+ state's parameters cannot be reached from just the R-matrix fitting to the triple-α data. The experiment should be repeated with improved detector arrangement in the future to gain more statistics.

The R-matrix fits 5 (figure 7.1b) and 7 (figure 7.1d) in section 6.3.2 had fixed parameters for the Hoyle state and the 2^+ state, and free parameters for the 10 MeV 0^+ state and the higher lying broad background 0^+ state (fit 5) or 2^+ state (fit 7). The comparison between these two presents some open questions. It can be seen in this comparison that depending on which background is included in the fit, the relative strength of the 0^+ state and the 2^+ state can change significantly. While for fit 5 the 2^+ state is rather weak, it contributes almost 50% of the total strength in the 10 MeV energy region in fit 7. The χ^2/N values for the two fits are too close to each other (1.04 for fit 5 and 1.06 for fit 7) to be able pick the best fit from the two. But the implications that the relative strength of the 0^+ and the 2^+ states may have on the measurement of the anisotropy in the β-α angular correlation make the fit 7 a stronger candidate because the smaller 2^+ component means the larger contribution from the β-decay to the observed anisotropies. Using the same argument, fit 6 can also be discarded as the 2^+ strength is too small to explain the observed large anisotropy in the 10 MeV energy region.s

7.3 Anisotropy in the β-α angular correlation

The theoretical assessment of the expected β-α angular correlation that was presented in the proposal [65] for the experiment was incorrect. In the present work, the theoretical description of the β-α angular correlation has been revised and the correct expression has been derived. As per this re-evaluated theoretical expression, the β-α angular correlation can mostly be expected to be isotropic (section 3.2.2). However, there has been an unambiguous observation of large anisotropy in the β-α angular correlations in the experimental data. The observed b_i*A values (table 6.1) range from 0.1 to 0.425, where b_i is the relative strength of the 2^+ component and A is

the anisotropy parameter associated with the β-decay. The b_i factor can only have values between 0 and 1, which means that observed values for A are of the order of magnitude 10^{-1}. This is two orders of magnitude larger than what has ever been observed before [66]. A possible explanation for this large anisotropy is that this is due to the combination of two factors that affect these angular correlations. First is the contribution of the second-forbidden transition to the allowed β-decay which can happen if the allowed transition is suppressed [67]. The ground state of the ^{12}N is a single-particle state and the ^{12}C resonance that are being studied in this work are expected to have the cluster structure. This structure difference between the parent and daughter nuclei could therefore suppress the allowed transition and enhance the anisotropy factor as has been explained in section 3.2.2. The second factor that can contribute to the large anisotropy is the effect of the relativistic momentum type element in the allowed GT transition [46]. Since the Q-value of the ^{12}N is $\sim$17 MeV, the β-particles in the decay can be considered ultra-relativistic. The two factors combined could give rise to such large anisotropies, but for the complete understanding of the physics behind this observation, in addition to more data, more input from the theorists is required. Particularly, theoretical values of the higher-order matrix elements for the transition between the shell-model like ^{12}N ground state and the expected cluster structure of the ^{12}C 2^+_2 state are needed to obtain the complete theoretical description of the angular correlation function.

In conclusion, we have identified the second 2^+ state in ^{12}C for the first time in a β-decay study. This is done through the novel technique of β-triple-α correlations. The observed correlation is exceptionally strong, and may originate from contributions of β-decay higher order matrix elements.

Appendix A

W1 detector specifications

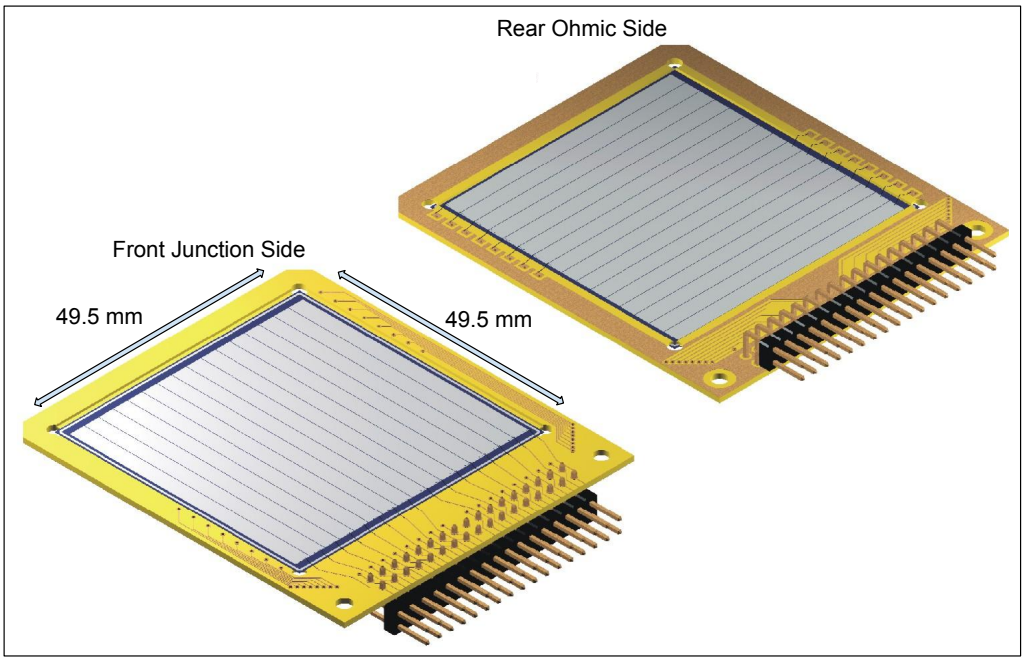

Fig. A.1 Drawing of W1 detector [68]

Number of strips (Junction side):16

Pitch in μm (Junction side): 3100

Number of strips (Ohmic side): 16

Pitch in μm (Ohmic side): 3100

Active area (mm^2): 49.50 x 49.50

Thickness range (μm): 40 – 1500

References

[1] URL www.nndc.bnl.gov/chart/.

[2] E. Margaret Burbidge, G. R. Burbidge, William A. Fowler, and F. Hoyle. Synthesis of the elements in stars. *Rev. Mod. Phys.*, 29:547–650, Oct 1957.

[3] H. Kragh. An anthropic myth: Fred Hoyle's carbon-12 resonance level. *Archive for History of Exact Sciences*, 64:721–751, 2010.

[4] C. Iliadis. *Nuclear Physics of Stars*. Wiley-VCH, Weinheim, 2007.

[5] H. A. Bethe. Energy production in stars. *Phys. Rev.*, 55:434–456, Mar 1939.

[6] E. J. Opik. Stellar Models with Variable Composition. II. Sequences of Models with Energy Generation Proportional to the Fifteenth Power of Temperature. *Proceedings of the Royal Irish Academy. Section A: Mathematical and Physical Sciences*, 54:49–77, 1951.

[7] E. E. Salpeter. Nuclear Reactions in Stars Without Hydrogen. *Astrophys. J.*, 115:326–328, March 1952.

[8] F. Hoyle, D. N. F. Dunbar, R. E. Pixley, W. A. Wenzel, and W. Whaling. The 7.68-Mev State in c^{12}. *Phys. Rev.*, 92:649–650, Nov 1953.

[9] F. Hoyle. On Nuclear Reactions Occuring in Very Hot STARS.I. the Synthesis of Elements from Carbon to Nickel. *Astrophys. J. Suppl. Ser.*, 1:121, September 1954.

[10] L. R. Hafstad and E. Teller. The alpha-particle model of the nucleus. *Phys. Rev.*, 54:681–692, Nov 1938.

[11] Kiyomi Ikeda, Noboru Takigawa, and Hisashi Horiuchi. The systematic structure-change into the molecule-like structures in the self-conjugate 4n nuclei. *Progress of Theoretical Physics Supplement*, E68:464–475, 1968.

[12] H. Morinaga. Interpretation of Some of the Excited States of 4n Self-Conjugate Nuclei. *Physical Review*, 101:254–258, January 1956.

[13] L. R. Buchmann and C. A. Barnes. Nuclear reactions in stellar helium burning and later hydrostatic burning stages. *Nuclear Physics A*, 777:254–290, October 2006.

[14] W. R. Zimmerman. *Direct Observation of the Second 2+ State in 12C*. PhD thesis, The University of Connecticut, 2013.

[15] C. Angulo, M. Arnould, M. Rayet, P. Descouvemont, D. Baye, C. Leclercq-Willain, A. Coc, S. Barhoumi, P. Aguer, C. Rolfs, R. Kunz, J.W. Hammer, A. Mayer, T. Paradellis, S. Kossionides, C. Chronidou, K. Spyrou, S. Degl'Innocenti, G. Fiorentini, B. Ricci, S. Zavatarelli, C. Providencia, H. Wolters, J. Soares, C. Grama, J. Rahighi, A. Shotter, and M. Lamehi Rachti. A compilation of charged-particle induced thermonuclear reaction rates. *Nuclear Physics A*, 656(1):3 – 183, 1999. ISSN 0375-9474.

[16] G. R. Caughlan and W. A. Fowler. Thermonuclear reaction rates V. *Atomic Data and Nuclear Data Tables*, 40(2):283 – 334, 1988. ISSN 0092-640X.

[17] H. O. U. Fynbo, C. Aa. Diget, U. C. Bergmann, M. J. G. Borge, J. Cederkall, P. Dendooven, L. M. Fraile, S. Franchoo, V. N. Fedosseev, B. R. Fulton, W. Huang, J. Huikari, H. B. Jeppesen, A. S. Jokinen, P Jones, B. Jonson, U. Koster, K. Langanke, M. Meister, T. Nilsson, G. Nyman, Y. Prezado, K. Riisager, S. Rinta-Antila, O. Tengblad, M. Turrion, Y. Wang, L. Weissman, K. Wilhelmsen, J. Aysto, and The ISOLDE Collaboration. Revised rates for the stellar triple-α process from measurement of ^{12}C nuclear resonances. *Nature*, 433:136–139, 22005.

[18] Shinya Wanajo, Hans-Thomas Janka, and Shigeru Kubono. Uncertainties in the νp-process: Supernova dynamics versus nuclear physics. *The Astrophysical Journal*, 729(1):46, 2011.

[19] Eduardo Bravo and Gabriel Martínez-Pinedo. Sensitivity study of explosive nucleosynthesis in type ia supernovae: Modification of individual thermonuclear reaction rates. *Phys. Rev. C*, 85:055805, May 2012.

[20] H Morinaga. On the spin of a broad state around 10 MeV in ^{1}2C. *Phys.~Lett.*, 21(1):78–79, 1966.

[21] A. Tohsaki, H. Horiuchi, P. Schuck, and G. Röpke. Alpha Cluster Condensation in ^{12}C and ^{16}O. *Physical Review Letters*, 87(19):192501, November 2001.

[22] Evgeny Epelbaum, Hermann Krebs, Timo Lähde, Dean Lee, and Ulf-G Meißner. Structure and Rotations of the Hoyle State. *Phys.~Rev.~Lett.*, 109(25):252501, December 2012.

[23] M. Itoh, H. Akimune, M. Fujiwara, U. Garg, H. Hashimoto, T. Kawabata, K. Kawase, S. Kishi, T. Murakami, K. Nakanishi, Y. Nakatsugawa, B.K. Nayak, S. Okumura, H. Sakaguchi, H. Takeda, S. Terashima, M. Uchida, Y. Yasuda, M. Yosoi, and J. Zenihiro. Study of the cluster state at e_x=10.3 mev in ^{12}C. *Nuclear Physics A*, 738(Supplement C):268 – 272, 2004. ISSN 0375-9474. Proceedings of the 8th International Conference on Clustering Aspects of Nuclear Structure and Dynamics.

[24] M. Freer, H. Fujita, Z. Buthelezi, J. Carter, R. W. Fearick, S. V. Förtsch, R. Neveling, S. M. Perez, P. Papka, F. D. Smit, J. A. Swartz, and I. Usman. 2^+. *Phys. Rev. C*, 80:041303, Oct 2009.

[25] M. Itoh, H. Akimune, M. Fujiwara, U. Garg, N. Hashimoto, T. Kawabata, K. Kawase, S. Kishi, T. Murakami, K. Nakanishi, Y. Nakatsugawa, B. K. Nayak, S. Okumura, H. Sakaguchi, H. Takeda, S. Terashima, M. Uchida, Y. Yasuda, M. Yosoi, and J. Zenihiro. Candidate for the 2^+ excited hoyle state at $E_x \sim 10$ mev in ^{12}C. *Phys. Rev. C*, 84:054308, Nov 2011.

[26] W. R. Zimmerman, N. E. Destefano, M. Freer, M. Gai, and F. D. Smit. Further evidence for the broad 2_2^+ state at 9.6 Mev in ^{12}C. *Phys. Rev. C*, 84:027304, Aug 2011.

[27] W. R. Zimmerman, M. W. Ahmed, B. Bromberger, S. C. Stave, A. Breskin, V. Dangendorf, Th. Delbar, M. Gai, S. S. Henshaw, J. M. Mueller, C. Sun, K. Tittelmeier, H. R. Weller, and Y. K. Wu. Unambiguous identification of the second 2^+ state in ^{12}**C** and the structure of the hoyle state. *Phys. Rev. Lett.*, 110:152502, Apr 2013.

[28] F. D. Smit, F. Nemulodi, Z. Buthelezi, J. Carter, R. W. Fearick, S. V. Förtsch, M. Freer, H. Fujita, M. Jingo, C. O. Kureba, J. Mabiala, J. Mira, R. Neveling, P. Papka, G. F. Steyn, J. A. Swartz, I. T. Usman, and J. J. van Zyl. No evidence of an 11.16 Mev 2^+ state in ^{12}C. *Phys. Rev. C*, 86:037301, Sep 2012.

[29] M Alcorta, M J G Borge, M Cubero, C A Diget, R Dominguez-Reyes, L Fraile, B R Fulton, H O U Fynbo, D Galaviz, S Hyldegaard, H B Jeppesen, B Jonson, O S Kirsebom, M Madurga, A Maira, A Muñoz, T Nilsson, G Nyman, D Obradors, A Perea, K Riisager, O Tengblad, and M Turrion. Properties of resonances in 12 C above the triple-alpha threshold. *Journal of Physics: Conference Series*, 312(9):092013, 2011.

[30] S. Hyldegaard, C. Forssén, C.Aa. Diget, M. Alcorta, F.C. Barker, B. Bastin, M.J.G. Borge, R. Boutami, S. Brandenburg, J. Büscher, P. Dendooven, P. Van Duppen, T. Eronen, S. Fox, B.R. Fulton, H.O.U. Fynbo, J. Huikari, M. Huyse, H.B. Jeppesen, A. Jokinen, B. Jonson, K. Jungmann, A. Kankainen, O. Kirsebom, M. Madurga, I. Moore, P. Navrátil, T. Nilsson, G. Nyman, G.J.G. Onderwater, H. Penttilä, K. Peräjärvi, R. Raabe, K. Riisager, S. Rinta-Antila, A. Rogachevskiy, A. Saastamoinen, M. Sohani, O. Tengblad, E. Traykov, J.P. Vary, Y. Wang, K. Wilhelmsen, H.W. Wilschut, and J. Äystö. Precise branching ratios to unbound ^{12}C states from ^{12}N and ^{12}B β-decays. *Physics Letters B*, 678 (5):459 – 464, 2009.

[31] Yamada, T. and Schuck, P. Single α-particle orbits and Bose-Einstein condensation in 12C. *Eur. Phys. J. A*, 26(2):185–199, 2005.

[32] M. Chernykh, H. Feldmeier, T. Neff, P. von Neumann-Cosel, and A. Richter. Structure of the hoyle state in ^{12}C. *Phys. Rev. Lett.*, 98:032501, Jan 2007.

[33] F. Ajzenberg-Selove and J. H. Kelley. Energy levels of light nuclei A = 11–12. *Nuclear Physics A*, 506, 1:1–158, 1990.

[34] H. O. U. Fynbo and C. Aa. Diget. Structure of 12C and the triple-α process. *Hyperfine Interactions*, 223(1):103–120, Jan 2014.

[35] D. Schwalm and B. Povh. Alpha particles following the β-decay of ^{12}B and ^{12}N. *Nuclear Physics*, 89(2):401 – 411, 1966. ISSN 0029-5582.

[36] M. Freer, M. Itoh, T. Kawabata, H. Fujita, H. Akimune, Z. Buthelezi, J. Carter, R. W. Fearick, S. V. Förtsch, M. Fujiwara, U. Garg, N. Hashimoto, K. Kawase, S. Kishi, T. Murakami, K. Nakanishi, Y. Nakatsugawa, B. K. Nayak, R. Neveling, S. Okumura, S. M. Perez, P. Papka, H. Sakaguchi, Y. Sasamoto, F. D. Smit, J. A. Swartz, H. Takeda, S. Terashima, M. Uchida, I. Usman, Y. Yasuda, M. Yosoi, and J. Zenihiro. Consistent analysis of the 2^+ excitation of the ^{12}C hoyle state populated in proton and α-particle inelastic scattering. *Phys. Rev. C*, 86:034320, Sep 2012.

[37] M. Gai. Private communication. 2017.

[38] S. Karataglidis, P. J. Dortmans, K. Amos, and R. de Swiniarski. Fully microscopic model of 200 Mev proton$-^{12}$C elastic and inelastic scattering. *Phys. Rev. C*, 52:861–877, Aug 1995.

[39] P. Navrátil, J. P. Vary, and B. R. Barrett. Large-basis ab initio no-core shell model and its application to ^{12}**C**. *Phys. Rev. C*, 62:054311, Oct 2000.

[40] D.M. Brink and E. Boeker. Effective interactions for hartree-fock calculations. *Nuclear Physics A*, 91(1):1 – 26, 1967. ISSN 0375-9474.

[41] M. Freer and H.O.U. Fynbo. The Hoyle state in 12C. *Progress in Particle and Nuclear Physics*, 78(Supplement C):1 – 23, 2014. ISSN 0146-6410.

[42] Y. Funaki, A. Tohsaki, H. Horiuchi, P. Schuck, and G. Röpke. Resonance states in 12C and α-particle condensation. *The European Physical Journal A - Hadrons and Nuclei*, 24(3):321–342, Jun 2005. ISSN 1434-601X.

[43] Y. Kanada-En'yo. The structure of ground and excited states of 12C. *Progress of Theoretical Physics*, 117(4):655–680, 2007.

[44] E. Epelbaum, H.-W. Hammer, and Ulf-G. Meißner. Modern theory of nuclear forces. *Rev. Mod. Phys.*, 81:1773–1825, Dec 2009.

[45] Krane K. S. *Introductory Nuclear Physics.* John Wiley and Sons, U.S.A., 1988.

[46] Siegbahn K. *Alpha-, Beta-, and Gamma-ray Spectroscopy.* North-Hollang Publishing Company, Amsterdam, 1965.

[47] M. Morita and R. Morita. Beta-gamma angular correlations and beta-ray angular distributions. *Progress of Theoretical Physics Supplement*, 37-38:458–472, 1966.

[48] M. Morita, M. Fuyuki, and S. Tsukada. Theory of Allowed Beta Decay with Higher Order Corrections. *Progress of Theoretical Physics*, 47:556–571, February 1972.

[49] G. Breit and E. Wigner. Capture of slow neutrons. *Phys. Rev.*, 49:519–531, Apr 1936.

[50] A. M. Lane and R. G. Thomas. R-matrix theory of nuclear reactions. *Reviews of Modern Physics*, 30:257–353, 1958.

[51] E. Vogt. Theory of low energy nuclear reactions. *Rev. Mod. Phys.*, 34:723–747, Oct 1962.

[52] P. Descouvemont and D.. Baye. The R-matrix theory. *Reports on Progress in Physics*, 73(3):036301, 2010.

[53] R. E. Azuma, E. Uberseder, E. C. Simpson, C. R. Brune, H. Costantini, R. J. de Boer, J. Görres, M. Heil, P. J. LeBlanc, C. Ugalde, and M. Wiescher. Azure. *Phys. Rev. C*, 81:045805, Apr 2010.

[54] F. James. Minuit: Function Minimization and Error Analysis. 94.1.ed, 1994.

[55] P. Karvonen, I.D. Moore, T. Sonoda, T. Kessler, H. Penttilä, K. Peräjärvi, P. Ronkanen, and J. Äystö. A sextupole ion beam guide to improve the efficiency and beam quality at IGISOL. *Nuclear Instruments and Methods in Physics Research Section B: Beam Interactions with Materials and Atoms*, 266 (21):4794 – 4807, 2008.

[56] G. F. Knoll. *Radiation Detection and Measurement Third Edition*. John Wiley and Sons, U.S.A., 2000.

[57] J. F. Ziegler, M. D. Ziegler, and J. P. Biersack. SRIM - the stopping range of ions in matter. *Nuclear Instruments and Methods in Physics Research B*, 268: 1818–1823, 2010.

[58] F.G. Kondev and S. Lalkovski. Nuclear data sheets for A = 207. *Nuclear Data Sheets*, 112:707–853, 2011.

[59] Appendix. Stopping power and range tables for charged particles. *Journal of the International Commission on Radiation Units and Measurements*, 14, 1:79–98, 2016.

[60] E. Browne and J. K. Tuli. Nuclear data sheets for A = 207. *Nuclear Data Sheets*, 114:1849–2022, 2013.

[61] D. R. Tilley, J. H. Kelley, J. L. Godwin, D. J. Millener, J. E. Purcell, C. G. Sheu, and H. R. Weller. Energy levels of light nuclei A = 8,9,10. *Nuclear Physics A*, 745, 3:155–362, 2004.

[62] J. Refsgaard. *Resonances, R-matrix – Rotations in 12C?* PhD thesis, Aarhus Universitet, 2016.

[63] Barlow R. J. *Statistics: A Guide to the Use of Statistical Methods in the Physical Sciences*. John Wiley and Sons, U.S.A., 1989.

[64] F.C. Barker and E.K. Warburton. The beta-decay of ^{8}He. *Nuclear Physics A*, 487:269–278, 1988.

[65] C. Aa. Diget, P Adsley, C. J. Barton, B. Blank, M. J. G. Borge, G. Canchel, T. Eronen, S. P. Fox, B. R. Fulton, H. O. U. Fynbo, M. Gerbaux, J. Giovinazzo, D. G. Jenkins, A. Jokinen, B. Jonson, A. M. Laird, I. Moore, T. Nilsson, G. Nyman, H. Penttila, K. Riisager, A. Saastamoinen, O. Tengblad, J. C. Thomas, and J. Aysto. Search for the second excited ^{12}C 2^{+} state using ^{12}N and ^{12}B decay beta-triple-alpha coincidence measurements at IGISOL. *Proposal to the JYFL PAC*, Mar 2010.

[66] R. M. Steffen. Search for higher-order effects in allowed beta decay. *Phys. Rev. Lett.*, 3:277–279, Sep 1959.

[67] Masato Morita. Higher order corrections to the allowed beta decay. *Phys. Rev.*, 113:1584–1589, Mar 1959.

[68] URL http://www.micronsemiconductor.co.uk/strip-detectors-double-sided/.